DISLOCATION INTERACTIONS WITH CHARACTERISTIC INTERFACES IN AG-CU EUTECTIC

BY

BENJAMIN P. EFTINK

DISSERTATION

Submitted in partial fulfillment of the requirements
for the degree of Doctor of Philosophy in Materials Science and Engineering
in the Graduate College of the
University of Illinois at Urbana-Champaign, 2016

Urbana, Illinois

Doctoral Committee:

Dean Ian M. Robertson, Chair
Dr. Nathan Mara, Los Alamos National Laboratory
Professor John Lambros
Professor Pascal Bellon
Associate Professor Shen Dillon

ABSTRACT

In the AgCu eutectic alloy, the observation of deformation twinning in Cu proposed to be induced by direct transmission of deformation twinning partial dislocations in Ag highlights the question of how interfaces in bi-phase materials respond to deformation. AgCu eutectic alloy was produced by both directional solidification and cast water-quenching. Control over processing variables enabled the synthesis of Ag/Cu eutectic with three predominant interface types: ones with a cube-on-cube orientation relationship with $\{111\}_{\mathrm{Ag}}||\{111\}_{\mathrm{Cu}}$ interface habit planes, twin orientation relationship with $\{111\}_{\mathrm{Ag}}||\{111\}_{\mathrm{Cu}}$ interface habit planes, and twin orientation relationship with near $\{\bar{3}13\}_{\mathrm{Ag}}||\{\bar{1}12\}_{\mathrm{Cu}}$ interface habit planes. How dislocations interacted with each of the interfaces was determined using *in situ* and *ex situ* TEM straining experiments. It was determined that how strain transfers across Ag/Cu interfaces is consistent with criteria of strain transfer across grain boundaries in single phase materials. Specifically, the magnitude of the Burgers vector of the residual dislocation, $|\mathrm{b}_{\mathrm{res}}|$, left in the interface should be small. This criterion was determining enough to drive Cu to twin under conditions where otherwise it would not. When transmission of a dislocation would result in a high $|\mathrm{b}_{\mathrm{res}}|$, which is common for most slip systems encountering an incoherent twin interface, the interfaces were observed to block the dislocations. It was found that the increased effectiveness of the incoherent twin interfaces to block dislocations compared to the cube-on-cube interfaces resulted in an increased in the yield strength of the material.

Interfaces with the cube-on-cube orientation relationship and mutual {111} interface plane between Ag and Cu results in transfer of twinning defects from Ag into Cu. This was found at length scales in the tens of nano-meters to the micron range. Twinning in both phases was observed after both split-Hopkinson pressure bar *ex situ* straining and tensile *in situ* straining. The

cube-on-cube interfaces were still found to be barriers as dislocation pile-ups formed against the interfaces. Dislocation content at the interfaces increased as well after deformation. Incoherent and coherent twin interfaces between Ag and Cu were greater barriers to strain transfer than the cube-on-cube orientation relationship interfaces. Incoherent twin interfaces were found to allow perfect but not partial dislocation communication on the shared {111} slip plane across the interfaces due to the larger $|b_{res}|$ to communicate the partial dislocations. On the non-shared plane perfect and partial dislocations were blocked by the interfaces.

ACKNOWLEDGEMENTS

I owe gratitude to many people, first of all to my advisor, Dean Ian Robertson, for the opportunity to pursue my PhD and his continual guidance throughout. He devoted an incredible amount of time to my betterment. Dr. Nate Mara contributed immensely as well in guiding me, and welcomed me during my time in Los Alamos. My parents also deserve recognition for their support through my life that allowed me to pursue this opportunity.

I have had the privilege to work closely with wonderful people and would like to give a special thank you to several of them. Dr. Owen Kingstedt who collaborated closely with me through the entirety of this project, and with whom I enjoyed my time working. Owen did the bulk mechanical testing of the materials for this study and contributed to my understanding of it. Professor John Lambros for his guidance from the start. Ao Li, Professor Izabela Szlufarska, and Dr. Shuai Wang who contributed their knowledge of computer simulations to greatly improve this work. Dr. Doug Safarik who guided me in processing the material for this study. I thank my committee members as well, Professors Pascal Bellon, and Shen Dillon for their time and input.

The Robertson group, past and present, also deserves my thanks for their help. I also enjoyed the events we had outside of the lab and the camaraderie. These including Aki Nagao, Kelly Nygren, Jaime Fenske, Kaila Bertsch, Josh Kacher, May Martin, Buyang Cao, Cindy Smith, Stephen House, Virginia McCreary, Megan Emigh, Grace Liu, Rigen Mo, Shi Shi, Shuai Wang and David Gross.

During my summers at Los Alamos National Laboratory I had the privilege to work with many people. I appreciated their technical expertise which was very helpful to me and would like to thank Dr. Irene Beyerlein, Dr. Rod McCabe, Dr. John Carpenter, Dr. Ben Morrow, Dr. Rob and

Pat Dickerson, Tom Wynn, Professor Amit Misra, the various post docs, numerous others, and my office mate Tom Nizolek.

TABLE OF CONTENTS

CHAPTER 1

INTRODUCTION

Materials with a high density of interfaces have been shown to have favorable properties including: high mechanical strength, corrosion and wear resistance, irradiation tolerance, and high electrical conductivity [1-6]. This raises the following questions: what is the role, if any, of the interface type, the atomic level structure of the interface, the dislocation structure of the interface and the spacing between each interface on material properties? In the case of mechanical strength, additional factors will need to be considered: the continuity of slip systems across the interface, the loading direction with respect to the interface normal, and the ability of the interface to accommodate shear stress. A fundamental understanding of the link between synthesis of materials with a high density of interfaces, the structure of those interfaces, and the resultant properties is an avenue to guide material design. In this research the emphasis is on the impact of interface type and density on the mechanical properties of a two component metallic system. The impact is determined by defect dynamics, as interfaces can act as either weak or strong barriers to strain transfer and act as both sinks and sources for dislocations [7]. Although there is considerable evidence, experimental, theoretical and simulation data, supporting the hypothesis that some mechanical properties can be improved as the density of tailored and controlled interfaces between dissimilar metallic systems increases, there remains a lack of direct support for the fundamental deformation mechanisms proposed to account for them [6, 8].

For this study, AgCu eutectic alloy serves as a model system for testing the bulk mechanical response of high interfacial density FCC-FCC metal composites. Through the use of different processing strategies, the bi-layer thickness can be controlled as can the type of interface [9, 10]. In the as-cast state, there are three possible interface types: $\{111\}_{\mathrm{Ag}}||\{111\}_{\mathrm{Cu}}$ with a cube-on-cube

orientation relationship, $\{111\}_{\mathrm{Ag}}||\{111\}_{\mathrm{Cu}}$ with twin orientation relationship, and twin orientation relationship with incoherent twin interface planes [10, 11]. The transfer mechanisms of dislocations across the interfaces are compared and contrasted with the slip transfer rules established for polycrystalline single-phase FCC metals and used to interpret the microstructures developed from the bulk mechanical tests, and to test the predictions of current models and computer simulations [6, 8, 12, 13].

CHAPTER 2

BACKGROUND

2.1 AgCu

Processing routes will be covered with the relative advantages and disadvantages of each for producing a material suited for studying dislocation interface interactions. Processing provides avenues to study AgCu with different interface types as well as constituent length-scales. Microstructure will be discussed based on specific interface types, morphology, length-scale of constituents, as well as chemical intermixing of the phases and tied to processing parameters.

2.1.1 Microstructures from different processing methods

Deposition

Physical vapor deposition has been used to produce thin films of AgCu composite multilayers [14-16]. For AgCu multilayers, individual layer thicknesses between 0.85 and 1500 nm thick have been produced. The mechanical properties have been assessed by nanoindentation [15, 16], and also tensile testing of free standing films [14]. Yield strength was found to follow the Hall-Petch relationship even down to 1 nm layer thicknesses [15]. AgCu deposited films exhibit a ⟨111⟩ growth direction, {111} interfaces between the layers independent of deposition substrate, and a cube-on-cube orientation relationship between Ag and Cu [16]. The drawback to these films for studying dislocation interactions with interfaces is only one interface type is present.

Casting

Water-quench casting has been used to produce eutectic AgCu composite rods, 3 to 10 mm diameter and 40 mm in length [17]. The microstructure consisted of colonies of Ag and Cu lamellae, with the colonies having diameters between 100 to 500 μm. The colonies were randomly oriented with respect to each other. Within the colonies the lamellae had a bi-layer thickness of approximately 100 nm. Undercooling is difficult to control and was measured to be approximately

260 °C during the water-quenching. An issue with using this material system to assess the mechanical properties is that the colonies are randomly oriented and therefore there is no knowledge of the direction of the applied load with respect to the interface normal. Additionally, lamellar thickness cannot be easily controlled.

Directional solidification, using the Bridgman furnace method, can be used to produce alloys in which the dominant bi-layer thickness can be controlled through changing the removal rate of the sample from the furnace, which impacts the undercooling [18, 19]. Faster removal rates result in a decrease in the bi-layer thickness. The correlation between orientation relationship between Ag and Cu with respect to removal rate, however, is not clear with cube-on-cube and twin orientation relationships between Ag and Cu having been observed [11, 18]. When grown directionally, the crystal direction along the growth direction for both Ag and Cu is ⟨101⟩ independent of orientation relationship [11, 18]. Directional solidification offers the advantage that the interfaces are aligned with the growth direction, which permits the determination of the dependence of the deformation response mode on the loading direction with respect to the interfaces.

Accumulative roll bonding

Accumulative roll bonding is also a viable option for producing bulk AgCu composites [20]. Structural refinement down to tens of nanometers was observed with a structure of elongated grains. This is different from the lamellar and fiber morphologies and well defined interfaces produced by casting. Although not practical to study defect interactions with characteristic interfaces, it is a way to produce bulk sheets of high strength and high conductivity material.

Wire drawing

Wire drawing can produce bulk AgCu composites with elongated fibers of both Ag and Cu-phases. The fibers can have diameters as small as 25 to 12.5 nm after reduction in cross section of 99.99% [21-23]. The Taylor wire method, where wire drawing occurs from molten metal in a glass tube, can be used to achieve a grain size as small as 10 nm within a wire of 10 μm diameter [24]. It was also shown that in the eutectic regions, coherent twin interfaces between Ag and Cu form and this has been attributed to the high cooling rate of the process [25].

Ball milling

AgCu composites have also been produced by ball milling, however, in the form of powders [26, 27]. Solid solutions with chemically diffuse interfaces between Ag and Cu rich regions are characteristic when milling powders for 5 hours at 473 K, while milling for 5 hours at 85 K produces a larger degree of intermixing producing a single solid solution. By this processing the interfaces are diffuse and again not practical for a study of defect interactions with specific and sharp interfaces.

2.1.2 Microstructure

Interfaces

Interface types generated in the AgCu system are limed to a cube-on-cube orientation relationship with $\{111\}_{\mathrm{Ag}}||\{111\}_{\mathrm{Cu}}$ or $\{100\}_{\mathrm{Ag}}||\{100\}_{\mathrm{Cu}}$ interface planes and either coherent or incoherent twin [10, 11, 28]. Coherent twin interfaces have been found only in multi-layered AgCu systems produced by casting [10], arc melting [10] and the Taylor wire method [24]. The dependence of the proportion of coherent twin Ag/Cu interfaces with cooling rate has not been established. For both cast and arc-melted material, coherent twin interfaces comprise half of the interfaces with the others exhibiting a cube-on-cube orientation relationship [10]. Incoherent twin interfaces have also been reported with deviations of the interface planes up to 20° from

$\{111\}_{Ag}||\{111\}_{Cu}$ when processing by directional solidification [11]. Processing by deformation with rolling provides an additional interface type, $\{001\}_{Ag}||\{001\}_{Cu}$ habit planes with a cube-on-cube orientation relationship between Ag and Cu. The $\{001\}$ habit planes were attributed to interface rotation due to the complete twinning of both phases across the interface [28]. Table 2.1 summarizes the interface types and processing methods to achieve them.

Table 2.1: Ag/Cu interface types experimentally observed.

Orientation relationship	Cube-on-cube	Cube-on-cube	Twin	Twin
Habit plane	$\{111\}_{Ag}||\{111\}_{Cu}$	$\{001\}_{Ag}||\{001\}_{Cu}$	$\{111\}_{Ag}||\{111\}_{Cu}$ (coherent twin)	Up to 20° from $\{111\}_{Ag}||\{111\}_{Cu}$ (incoherent twin)
Processing	Water-quench casting and directional solidification [10, 29]	Water-quench casting followed by rolling [30]	As-cast [10]	Directional solidification [11]

Limited literature is available on the chemical abruptness of the interfaces in AgCu produced by techniques other than ball milling. X-ray diffraction has been used for water-quenched AgCu to approximate concentrations of Ag in Cu and vice versa by measuring the lattice parameters of each phase [17]. Prior to the analysis, the materials were annealed at temperatures between 200 °C and 600 °C as well as at room temperature; the results are presented in Fig. 2.1. In the initial state, around 3.5 atomic percent Ag is in the Cu-phase and 5.0 atomic percent Cu is in the Ag-phase. An anneal at 400 °C for 1 hour resulted in the smallest intermixing with the concentrations around 1.5 atomic percent Ag in Cu and 1.0 atomic percent Cu in Ag. The concentration of Ag in the Cu-phase is important for studying twinning deformation in the Cu-phase as solute concentrations commonly decrease the stacking-fault energy and increase the twinnability in FCC metals [31, 32].

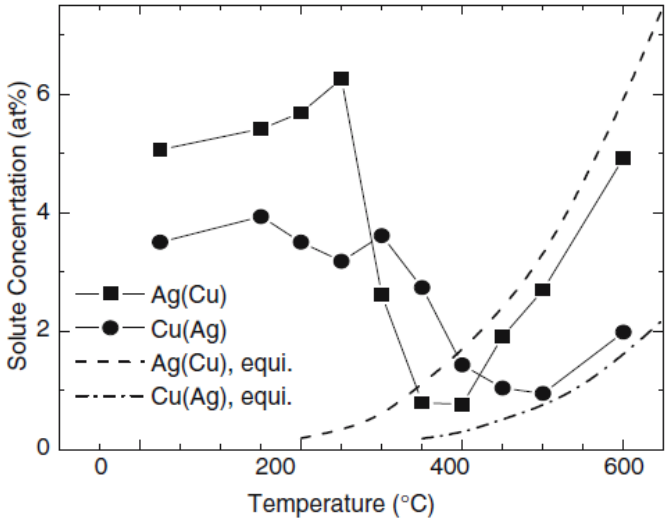

Figure 2.1: Concentrations of Ag in Cu and vice versa for as-cast AgCu eutectic after annealing at the given temperatures for 1 hour. Equilibrium values shown as the dotted lines [17].

Morphology

Directionally solidified AgCu eutectic has been shown to have morphologies of near circular fibers and lamellar structures [18, 19]. Water-quenched material, however, has shown exclusively a lamellar structure organized in colonies [10, 28, 33]. Observing both fiber and lamellar morphologies relates to volume fraction of the phases in the AgCu system, which straddles the boundary between lamellar and fiber morphology for eutectics [19, 34]. Accumulative roll bonding produces a structure with layers of Ag and Cu with elongated grains [20]. Wire drawing produces a microstructure with Ag and Cu fibers [35]. Ball milling results in highly intermixed solid solution with a grain and sub-grain structure [26].

Length-scale

The bi-layer thickness of the Ag and Cu constituents can be controlled through the growth rate or by annealing treatments. Shen *et al*. examined the thermal stability of the water-quenched AgCu eutectic with annealing treatments for 1-hour at temperatures between 200 °C and 600 °C [17].

The microstructural length-scale called "crystallite size" was measured by using the Scherrer formula using a (111) x-ray diffraction peak for both Ag and Cu. The comparison of crystallite size and annealing temperature is plotted in Fig. 2.2. The value of "crystallite size" was found to be roughly half of the bi-layer thickness. From the graph it is determined that the structural length-scale is retained on annealing at temperatures up to 400 °C for 1 hour, above 400 °C the microstructure coarsens.

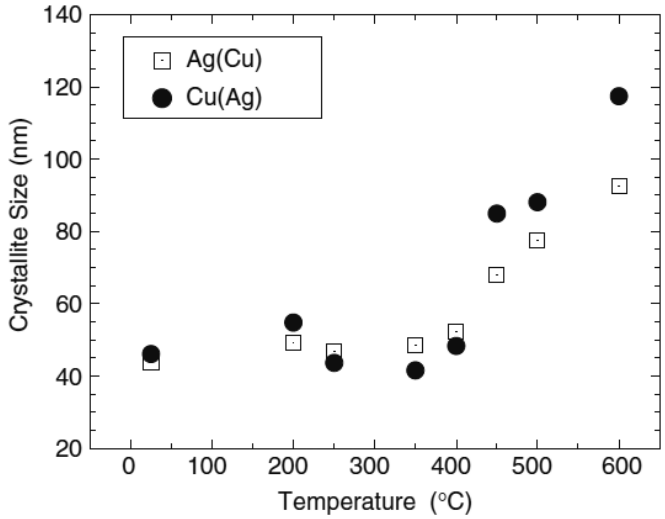

Figure 2.2: Crystallite size versus 1 hour annealing temperature of water quenched AgCu eutectic [17].

Using the Bridgman furnace method of directional solidification provides greater control of bi-layer thickness [18, 19, 36]. Bi-layer thicknesses from three different studies are plotted as a function of melt removal rate in Fig. 2.3. The data are plotted on a log scale because bi-layer thickness changes are more sensitive to changes in removal rate at lower removal rates. For the three cases plotted, the data from each falls on a straight line, albeit with different gradients. Generally, for eutectics $\lambda^2 v$ is equal to a constant value where λ is the bi-layer thickness and v is the growth rate. According to Fig. 2.3, for AgCu eutectic $\lambda^2 v$ is between $0.9 * 10^{-8}$ and $7.1 *$

$10^{-8}\ \frac{\text{mm}^3}{\text{s}}$. The differences in the studies are not clear but could be from differences in temperature gradients or purity of starting material.

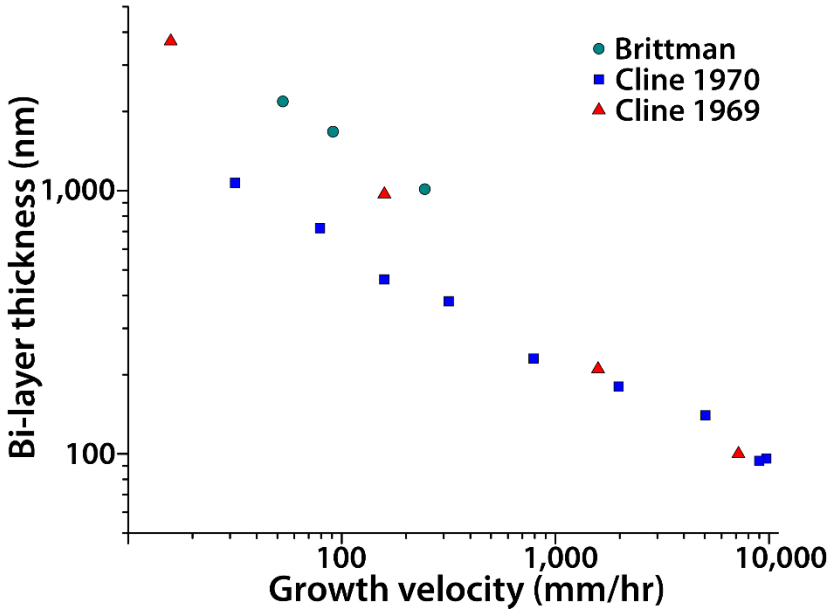

Figure 2.3: Bi-layer thickness as a function of growth velocity for AgCu eutectic in three studies [18, 19, 36].

2.2 Metallic multilayers: mechanical properties and deformation mechanisms

Before looking at how bi-phase components deform it is instructive to review, briefly, single phase material deformation. Initial deformation can occur by dislocation slip, deformation twinning, or a mixture of both. The interaction of dislocations mobile on different slip systems can result in the formation of dislocation tangles that at high levels of strain organize into low energy dislocation cells [37]. The cell walls contain a high dislocation density and the cell interiors are largely free of dislocations. At increasing levels of strain, the dislocation cells transition to geometrically necessary grain boundaries and sub grain boundaries [38, 39]. Deformation twinning occurs in certain coarse grained materials after the activation of dislocation slip [40-42]. Determination of activation of deformation twinning includes both intrinsic and extrinsic factors favoring materials with low stacking-fault and unstable-twinning energies, large grain size (coarse

grain materials), low temperature, high strain-rate, and certain crystal orientations including ⟨100⟩ and ⟨111⟩ in compression and ⟨101⟩ and ⟨111⟩ in tension [42-49]. Nano-grained materials can deform by deformation twinning as well, however, from interface driven mechanisms compared to dislocation driven mechanisms in coarse grained materials [50]. The deformation response for several materials is given in Table 2.2.

Table 2.2: Deformation mode for several FCC metals.

Material	Ag	Al	Cu	Cu-20 at% Zn	Ni
Deformation mode	Dislocation slip and deformation twinning [42].	Dislocation slip. Deformation twinning in nanocrystalline material [50].	Dislocation slip. Deformation twinning when at high strain-rate (shock loading) [45, 48, 51, 52], cryogenic temperature [53], less than tens of nanometer grain size [54].	Dislocation slip and deformation twinning [44].	Dislocation slip. Deformation twinning at cryogenic temperature [55].

The idea behind using composite materials with a layered structure for improving mechanical strength is rooted in using interfaces to hinder dislocation mobility. Metallic multilayers have long been found to have beneficial mechanical properties. For example, Palatnik *et al*. determined that vapor deposited Cu/Cr laminants retained their strength to 400 °C as opposed to 180 °C for Cu [56]. Strength as a function of layer thickness was studied using vapor deposited Cu/Fe laminants which showed consistency with the general Hall-Petch strengthening relationship with layer thicknesses decreasing to the tens of nanometers range [57]. Multilayer thin films produced by physical vapor deposition (PVD) have been used to investigate the strength as a function of layer thickness because of i) the wide range of possible layer compositions and ii) precise control of

layer thicknesses. The drawback of PVD for deformation based experiments is the materials can only be produced as thin films with a maximum total thickness on the order of microns.

Studies of defect dynamics in nano-structured bi-metal composites and nano-grained materials have resulted in several proposed mechanisms for plastic deformation that vary with length scale [6, 58, 59]. With layer thicknesses greater than tens of nanometers to 100 nm, the strengthening relationship follows a Hall-Petch like relationship, in which the strength is dependent on the inverse square root of the layer thickness, i.e. $\sigma \propto {}^{1}/_{h^{1/2}}$ where h is the layer thickness and σ is mechanical strength. Here it is assumed that the deformation behavior is similar to that in coarse grained material and that pile-ups of dislocations form against the interfaces.

Studies of multi-phase thin film laminates have reported deviations from the Hall-Petch relationship when the layer thickness decreased to below several tens of nanometers [60-62]. For example, Misra *et al*. has reported a deviation from the Hall-Petch relationship in Cu-Nb, Cu-Cr, and Cu-Ni multilayer thin films at layer thicknesses less than 50nm independent of whether the system was FCC/FCC or FCC/BCC [58]. Similar deviations had previously been reported for single phase materials with grain sizes in the nanometer range, for example nanocrystalline Cu and Pd with grain sizes between 16 and 6.25 nm, where strength decreased with decreasing grain size [63]. The deviation from the Hall-Petch relationship was observed regardless of interface type and material system. It was proposed that with decreasing layer thickness the formation of dislocation pile-ups is prohibited and deformation occurs by single dislocation slip mechanisms [58, 64, 65]. For example, confined layer slip dominates plastic deformation in systems with layer thicknesses between a few tens of nanometers to a few nanometers [59, 64, 66, 67]. Embury and Hirth suggested that at small length-scales, nanometer-scale, Frank-Read sources do not operate and dislocation nucleation occurs by bowing out from the interfaces [65]. Strengthening is then

attributed to Orowan bowing as the stress required to bow a dislocation in a layered structure is proportional to $\frac{\ln(h)}{h}$ where h is the layer thickness. Scattergood and Koch suggested the change in strengthening trend corresponds to a decrease in line energy of dislocations with decreasing layer thickness, which can be used to modify a dislocation network based Hall-Petch model [68]. Material hardness below a critical grain size is proportional to $\ln\left(\frac{D}{r_{eff}}\right) D^{-\frac{1}{2}}$ compared to the common Hall-Petch relationship $D^{-\frac{1}{2}}$ where D is grain size and r_{eff} is the effective dislocation core-cut off distance.

In the range of layer thicknesses of a few nanometers where the dislocation core diameter is close to the layer thickness, it was proposed that dislocations can easily cross the interfaces to account for the plastic deformation and there is an associated decrease in strength with decreasing layer thickness. Misra *et al*. found good agreement of the three strengthening regimes corresponding to those above from hardness data in various metallic composite thin films [64]. Fig. 2.4 shows the strength with respect to layer thickness for several Cu-based metallic composite systems. However, there is a lack of direct experimental data on the specific deformation processes that operate in multi-layered systems as function of bi-layer-thickness. Additionally, these deformation mechanisms were proposed based solely on layer thickness and are considered general and to be independent of the type of interface that exists.

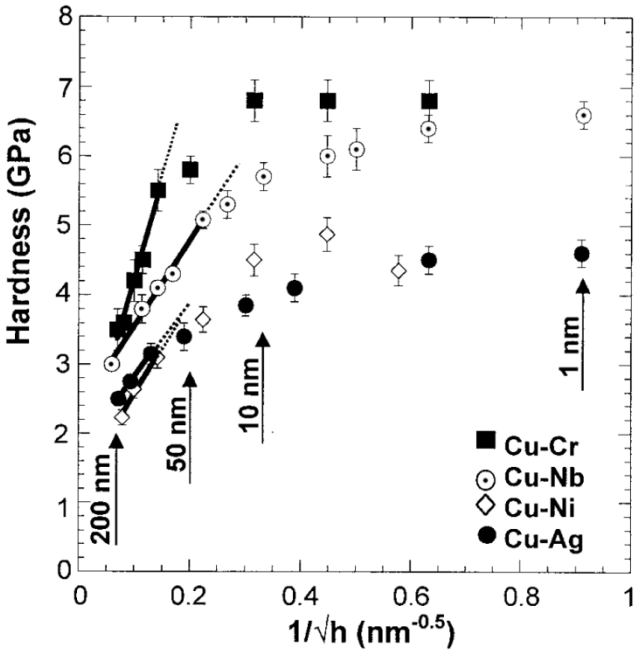

Figure 2.4: Hardness as a function of inverse square root of layer thickness. Hall-Petch trend given by the solid black lines [64].

If the structure of the interface is taken into account a more accurate assessment of possible deformation mechanisms can be formed. One of the simpler treatments splits the interface types into two categories: transparent and opaque [12]. The key difference between the two types is related to alignment of slip systems and is therefore a general interpretation of the criteria found applicable for single phase grain boundaries, the details of which are presented later [12]. Transparent interfaces have the same crystal structure on both sides of the interface, for example FCC/FCC, and the two phases must have a cube-on-cube orientation relationship as this relationship results in alignment of all the slip systems on both sides of the interface. Opaque interfaces generally will have misaligned slip systems such that dislocation communication between layers occurs by absorption and nucleation of dislocations from the interfaces. Opaque

interfaces exist in FCC/BCC or FCC/HCP systems in general or FCC/FCC systems with a twin orientation relationship.

For transparent interfaces, resistance to communicate strain across the interfaces arises due to coherency strains, image (Koehler) stresses, energy to create a step at the interface, and interactions with the interface misfit dislocations [12, 18, 69]. Coherency strains are the tensile and compressive strains near the interfaces caused by the two crystals trying to achieve continuity across the interface despite having different lattice parameters. Image stresses result from the difference in the shear modulus across the interface. Several studies probed the relative importance of the resistances to dislocation communication in terms of material strength with conflicting conclusions. Mitchell *et al*. were able to separate the impact of coherency strains compared to differences in moduli in nitride thin films by changing both stoichiometry and chemistry of the layered composites [60]. The difference in modulus was found to have a stronger influence on strength. However, the highest lattice mismatch used was only 1.7%, which is small and does not make for a good comparison. Misra *et al.* later proposed that at larger differences in lattice parameters, the introduction of periodic misfit dislocations will serve as significant strengtheners as they provide a resistive stress to Orowan bowing of dislocations [70]. Hoagland *et al.* based on atomistic simulations, proposed coherency strain as the most dominant factor for strengthening when the slip systems were well-aligned such as in FCC/FCC systems with a cube-on-cube orientation relationship [12]. It was found that the coherency stress was near the stress required to propagate a lead partial dislocation across a (010) Cu/Ni interface. However, because Cu and Ni interfaces have large separations between misfit dislocations, 9.6 nm, it was noted that this stress for communication is for "windows" between misfit dislocations [71]. The analysis was repeated for a Ag/Cu interface with a (010) interface plane with misfit dislocations more closely spaced at

2.27 nm. However, the core structure of misfit dislocations in the Ag/Cu interface overlap with neighboring misfit dislocation cores such that the coherency stresses are low. The Ag/Cu interface was also found to be very weak in shear which resulted in the interfaces acting as sinks for the dislocations such that transmission into the next layer was not found, which is different from the Cu/Ni result. Though coherency strains, images stresses, and misfit dislocations contribute to strengthening of the FCC/FCC interfaces, the relative contributions are not known and are dependent on details such as incoming dislocation core spreading. Direct experimental observations of the dislocation/interface interactions for "transparent" interfaces are still needed to verify these models. Opaque interfaces do not have aligned slip systems across the interfaces for dislocations and the barrier strength to dislocations is directly related to ability of the interface to trap dislocations. The key factor for dislocation trapping in opaque interfaces is promoting dislocation core spreading in the interface, a characteristic of interfaces weak in shear [72].

Interface type impacts the deformation response and part of the motivation of this thesis is deformation twinning in Cu. Twinning in Cu has been reported for both AgCu and Cu-Nb composite systems [30, 73-76]. Twinning in Cu has been reported to occur in AgCu alloys in regions with a cube-on-cube orientation relationship between the phases with $(111)_{\mathrm{Ag}}||(111)_{\mathrm{Cu}}$ interfaces at high strains, greater than 52.9% rolling reductions, for initial layer thicknesses less than 350 nm [30, 73, 74]. This response has been attributed to direct transmission of twinning partial dislocations from Ag through the interface into Cu [30, 73]. This particular mechanism does not derive from interface-mediated nucleation processes, and depends instead on a prolific supply of twinning partial dislocations from the Ag-phase transmitting into the Cu-phase. As such, in the AgCu system, twinning should occur in Cu under conditions twinning in Cu would otherwise not occur including at moderate temperatures and strain rates. Twinning partial

dislocation communication across the interface from Ag to Cu, however, has barriers arising from the presence of misfit dislocations and coherency strains to account for the lattice mismatch between phases; image forces due to differences in elastic modulus; and the necessity to leave a residual dislocation at the interface with a Burgers vector of $b_r = \frac{a_{Ag}-a_{Cu}}{6} < 112 > = 0.196$ Å for each twinning partial dislocation involved in the strain transfer, where a_{Ag} and a_{Cu} are the lattice parameters of Ag and Cu, respectively [12, 18, 28]. Deformation twinning in Cu is also found in accumulative roll bonded Cu and Nb with the Kurdjumov-Sachs (KS) relationship with $\{112\}_{Cu}||\{112\}_{Nb}$ and $\langle 110\rangle_{Cu}||\langle 111\rangle_{Nb}$. Deformation twinning occurs in the Cu-phase by dissociation of misfit dislocations at the Cu/Nb interface or by geometrically well-aligned perfect dislocations in Nb transferring strain across the interface by twinning partial dislocation emission from the Cu/Nb interface into Cu or by a combination of the two [75]. The layer thickness influences the twinning response in multi-layered Cu-Nb with deformation twinning being prolific in Cu at layer thicknesses less than 30 nm and occurring less frequently in layers with a thickness up to 80 nm [77]. For the AgCu system twinning in Cu has only been confirmed for cube-on-cube type interfaces, testing other characteristic interfaces will help elucidate the mechanism driving twinning in Cu for a variety of interface types.

2.3 Slip transfer across interfaces

Understanding how dislocations interact with interfaces is a natural first step in understanding how to design materials with specific interfaces that strengthen materials. Traditionally, the Hall-Petch relationship is used to correlate strength of materials as a function of grain size, this, however, treats grain boundaries and interfaces in a non-specific way that does not consider interface characteristics. In particular, the proportionality constant is meant to reflect the average strength of the grain boundaries rather than specific boundary types. Characteristics of specific

grain boundaries are instead considered in the following mechanisms for interactions of dislocations with single phase grain boundaries.

2.3.1 Single phase

Criteria used to predict the slip system activated by a grain boundary to transfer slip has been reviewed recently [78]. Here the proposed mechanisms considered are discussed briefly. These mechanisms include: the Livingston and Chalmers criterion, two different Geometric criteria, and the Lee, Robertson, and Birnbaum criteria. Followed by considerations based on grain boundary structure.

Livingston and Chalmers proposed that the activation of a slip system across a boundary could be predicted based on the local shear stress produced by dislocation pile-ups against the grain boundary [79]. The local shear stress was considered to be on the slip plane and in the slip direction of the dislocations in the pile-up. The resultant shear stress on the various slip systems in the neighboring grain was calculated to be proportional to N_{1i} from the following equation.

$$\mathrm{N_{1i}} = (\mathrm{e_1} \cdot \mathrm{e}_i)(\mathrm{g_1} \cdot \mathrm{g}_i) + (\mathrm{e_1} \cdot \mathrm{g}_i)(\mathrm{e}_i \cdot \mathrm{g_1}) \quad (1)$$

where $\mathrm{e_1}$is the slip plane normal and $\mathrm{g_1}$ is the slip direction for the pile-up dislocations. e_i is the slip plane normal and g_i is the slip direction of the system *i* in the next grain. Maximizing $\mathrm{N_{1i}}$ is used to predict the activated slip system in the neighboring grain due to the dislocation pile-up. This criteria was used for Al bi-crystals and found to be able to predict the slip plane in the majority of cases. Because it was verified on slip trace analysis it did not probe the actual Burgers vectors of the dislocations involved in the process of slip transfer. It has since been shown there is a more accurate predictor of slip systems than using local resolved shear stress.

There are two variations of the geometric criterion, the first couples the lines of intersection of the incoming and outgoing slip planes and the slip direction, in the following equation, with the local resolved shear stress.

$$M = (L_1 \cdot L_i) * (g_1 \cdot g_i) \quad (2)$$

where L_1 and L_i are the lines of intersection of the incoming and the i^{th} outgoing slip planes in the interface. g_1 and g_i are the slip directions of the incoming and the i^{th} outgoing dislocations. Maximizing M can be used to select the outgoing slip system. The criterion M alone, however, only correctly predicted three of five cases involving slip transfer across grain boundaries in 304 SS [80]. Shen *et al.* found using this criterion to predict the slip plane of the outgoing system and then determining the Burgers vector by the local resolved shear stress was a better predictor, predicting all five cases [80, 81]. It was noted by Lee *et al.* that the slip direction used to determine the slip plane using the geometric criterion does not always match the Burgers vector predicted by the resolved shear stress [82]. Even though the criterion proposed by Shen *et al.* is generally predictive, there is a gap in the understanding of the dislocation/interface interactions. This combination of criteria is also difficult to apply in situations in which more than one slip system is incident on the same location of the grain boundary or multiple slip systems are activated by the grain boundary and ejected into the adjoining grain.

A similar geometric compatibility factor is defined in the following equation [83, 84].

$$m' = \cos(\phi) \cdot \cos(\kappa) \quad (3)$$

where ϕ is the angle between the slip plane normals, and κ the angle between the slip directions of the two neighboring crystals. The higher the m' value, up to 1, the more compatible the slip systems are and the easier for strain to transfer from one grain to the other. The difference between

m′ and M is in how the incoming and outgoing slip planes are treated. For m′ using the angle between the slip plane normals places a preference on local resolved shear stress whereas M uses lines of intersection in the interface which places the preference in minimizing climb of the dislocations in the interface which suggests the incoming and outgoing dislocation is the same. Luster *et al.* applied the m′ criterion to predict slip transfer across grain boundaries in a Ti-47.5Al-2.5Cr alloy deformed *ex situ* and the interactions characterized by using TEM [84]. The predicted slip systems were found to be in good agreement with the observations. The m′ criterion, in a modified form, was also applied to explain deformation twinning in Cu in CuNb multilayers [85].

The Lee, Robertson, Birnbaum, LRB, criterion proposes a modification to the geometric criterion, M, by decoupling the Burgers vector and alignment of slip plane traces in the interface and adding consideration of local resolved shear stress. They proposed that the outgoing slip system can be determined by (1) minimizing the magnitude of the Burgers vector of the residual dislocation left in the grain boundary as a result of the incoming and outgoing dislocations, (2) maximizing the local resolved shear stress experienced by the active slip plane, and (3) minimizing the angle between the traces of the slip planes on the grain boundary plane. Condition 1 and 2 are in competition for the outgoing slip system with condition 1 believed to be more important in unirradiated materials [13]. The LRB criterion is not limited to perfect dislocations but also applies to partial dislocations with both resolved shear stress and magnitude of the residual Burgers vector at the interface being different for the leading and the trailing partial dislocation [86]. The LRB criterion has been found to be predictive by experimental studies on several FCC and HCP systems [82, 86-90]. It is unclear, however, if the criterion applies to BCC systems [91, 92].

Critiques of the above criteria which are experimentally based, have been offered from molecular dynamics simulations which enable dislocation/interface interactions to be probed in

greater temporal and spatial detail than *in situ* TEM straining experiments. Dewald *et al*., for example, developed a modified LRB criterion (MLRB) based on simulations which is listed below [93].

1. The angle of intersection of incoming and outgoing slip planes with the interface should be minimized
2. The magnitude of the residual Burgers vector or step created by residual dislocations left at the grain boundary after emission from the boundary should be small.
3. For transmission, the resolved shear stress on the emitted dislocations should be high, the resolved shear stress on the grain boundary should be low.
4. For grain boundary dislocation formation, the primitive vectors of the grain boundary and associated step should be small.
5. The normal compressive stress on the boundary should be small.
6. If a lagging lattice Shockley partial dislocation remains near the intersection but has not absorbed, the resolved shear stress acting on the leading pile-up dislocation need not be high.
7. An intrinsic stacking fault must be formed upon transmission of a leading Shockley partial dislocation.

The MLRB criterion is not easily used as a predictive set of criteria, nor was it proposed as such. Rather, it adds additional considerations to the LRB slip transfer criteria. The relative importance of the components of the MLRB were found to be dependent on the interface structure, which questions whether a large set of criteria can be broadly applied. However, it was noted that the magnitude of the residual Burgers vector left at the interface and the resolved shear stress on the outgoing system were the two most important factors in determining the reaction [93].

The criteria mentioned are for predicting activated slip when dislocations encounter an interface, however, they lack dependence on interface structure and do not offer the barrier strength of interfaces both of which are important for material design. Molecular dynamics simulations allow simplified dislocation/interface interactions where the interface structure and dislocation Burgers vector can be specifically chosen and observed in atomistic detail. Several studies have shown dislocation/interface interactions are dependent on the structure of the interface [94-96]. For example, molecular dynamics simulations of Ni bicrystals showed a large angle grain boundary Σ7 (38.2° tilt boundary about [111]) was more resistive to dislocation transmission than a small angle grain boundary Σ57 (13.2° tilt boundary about [111]). It was determined that the increased resistance was from both a smaller distance between dislocation pinning points and an increase in the residual dislocation Burgers vector left at the interface for transmission. Additionally, the sign of the dislocation was found to be important because during transmission one would increase the interface energy while the other would decrease it. In a separate study, Sangid *et al.* used molecular dynamics simulations to calculate the energy barrier to dislocation transmission for several coincident site lattice (CSL) grain boundaries and found increasing barrier strength to dislocations with decreasing interface energy. The reactions that occurred were verified by comparison with previous experimental results. The measurements were not repeated for multiple incoming slip systems which could change the results. The Σ3 coherent twin interface, for example, is known to be a strong or weak barrier depending on the incoming slip system, however, is only considered a strong barrier by Sangid *et al*. Molecular dynamics simulations additionally revealed that increasing free volume at the interface resulted in a decrease in stress necessary to nucleate dislocations [96]. This was attributed to the interfaces ability to more easily rearrange. The impact of this free volume observation is not entirely clear as it has been proposed

that interfaces weak in shear, which have an increased free volume, are better able to trap dislocations in the interfaces due to dislocation core spreading [12].

2.3.2 Twin boundaries

Twin interfaces are prevalent in the AgCu system so it is necessary to understand how dislocations interact with twin boundaries in single phase materials [49]. Extensive studies have been done on defect interactions with coherent twin interfaces [86, 97, 98], however, not on incoherent twin interfaces, the type primarily investigated in this thesis. While coherent and incoherent twin interfaces share the same orientation relationships of the matrix and twin grains, the habit planes are different. Coherent twins have the $\{111\}$ twin plane as the habit plane and incoherent twin interfaces do not.

The case of a perfect screw dislocation interacting with a coherent twin interface when the Burgers vector is in the interface plane has several reactions that have been either observed experimentally or predicted by simulations. Experimental observations during *in situ* straining experiments on 310 stainless steel in the TEM have shown perfect screw dislocations are able to transfer across the coherent twin interface while retaining the same Burgers vector [87]. This results in no residual Burgers vector left at the interface and satisfies both the geometric, M and m', and LRB criterion. Another reaction observed experimentally in Cu and from molecular dynamics simulations in Al is the dislocation absorbing and dissociating in the coherent twin plane [99]. This reaction is written below for a (111) twin plane.

$$\frac{a}{2}[1\bar{1}0]_M \rightarrow \frac{a}{6}[2\bar{1}1]_M + \frac{a}{6}[1\bar{2}\bar{1}]_M \quad (4)$$

Subscript M denotes matrix or original grain. This reaction fits well into the geometric criteria M but not m', as the angle between the incoming and outgoing slip planes is 70.5°. Criteria 2 ,which

is the most determining of the LRB criteria is satisfied as the combined Burgers vectors of the twin boundary dislocations is equal to the incoming dislocation and the slip planes intersect as a line in the interface satisfying criteria 3. Simulations found the dissociation of the dislocation on the coherent twin plane is material dependent. This material dependence was suggested to be from energetics of nucleating partial dislocations. Dewald *et al.* proposed the screw dislocation should be treated as an extended dislocation and when the leading partial dislocation is absorbed into the coherent twin boundary two reactions can be predicted based on elastic energy [100]:

$$\frac{a}{6}[1\bar{2}1]_M \rightarrow \frac{a}{6}[2\bar{1}1]_T + \frac{a}{18}[112]_{M\ residual} + \text{stacking fault} \quad (5)$$

and

$$\frac{a}{6}[1\bar{2}1]_M \rightarrow \frac{a}{6}[2\bar{1}1]_{M\ grain\ boundary} + \frac{a}{6}[\bar{1}\bar{1}0]_{M\ residual} \quad (6)$$

Subscripts *M* and *T* denote matrix and twin grains respectively. The first is an intermediate step for transmission and the second is an intermediate step for dissociation at the twin interface. The first has a lower elastic energy however a stacking fault must be created whereas the second has a higher elastic energy but does not require a stacking fault. It was predicted that materials such as Cu, with a medium stacking fault energy, would favor the first reaction and the screw dislocation would transmit across the interface. Al, because of its high stacking fault energy, would favor the second reaction and dissociate on the coherent twin boundary. These intermediate reactions also describe the interaction of 30° from screw (mixed character) partial dislocations with the interface.

Jin *et al.* made similar findings however found the extended dislocation must constrict when it reaches the interface so the intermediate reactions would not apply. The authors did propose the outgoing dislocation across the twin was an extended dislocation which results in a stacking fault.

Jin *et al.* went further in the analysis, however, in quantifying resistance to nucleate a partial dislocation on both the twin plane (R′) as well as a non-twin plane (R).

$$R = \frac{\gamma_{US} - \gamma_S}{\mu b_S} \tag{7}$$

and

$$R' = \frac{\gamma_{UT} - \gamma_S}{\mu b_S} \tag{8}$$

where γ_{US} is the unstable stacking fault energy, γ_{UT} is the unstable twinning energy, γ_S is the stacking fault energy, μ is the shear modulus, and b_S is the size of a Shockley partial dislocation. For Cu and Ni, R is lower than R′. For Al, R′ is lower and the value is negative suggesting the dissociation into partial dislocations on the twin plane is favorable.

Interactions of 60° dislocations with coherent twin boundaries are less straightforward. Both the geometric and LRB criteria predict interactions involving these dislocations to be less favorable than the one described above. Molecular dynamics, MD, computer simulations have been used to investigate the interactions of the 60° dislocations with a coherent twin boundary. Multiple reactions were simulated and all left residual dislocation content at the interface [101, 102]. Jin *et al.* found the reaction to be dependent on the resistance to nucleate a partial dislocation on the twin plane [102]. For Cu the resistance was high and the reaction resulted in the emission of a dislocation into the twin grain while leaving a partial dislocation at the interface. In Al, the resistance to nucleate a dislocation in the boundary is negative and the boundary acts like a sink and does not result in nucleation of defects into the twin grain. In each case the magnitude of the Burgers vector of the residual dislocation left at the interface is substantial. These MD simulations

differ from slip transfer criteria presented previously in that the interactions were found to be material dependent.

In general, coherent twin interfaces are strong barriers to dislocations through both the lack of slip continuity and production of sessile dislocations, except for screw dislocations that can cross-slip across the interface. What remains to be investigated for dislocation interactions with twin interfaces includes bi-phase and incoherent twin interfaces. Bi-phase systems are much more complicated in that the two materials will have differences in lattice parameter, shear modulus, and in their gamma surfaces. This will impact the characteristics of the interface locally and also changes the energetics of dislocation incorporation into and nucleation away from the interface. It is unknown if the differences between the single phase and bi-phase twin interfaces substantially change the way dislocations interact with them. In Cu for example, direct communication of dislocations across an incoherent twin interface on the twin plane has been implied from the continuity of the slip bands in the two grains [103]. Incoherent twin interfaces will change the deformation response compared to coherent twin interfaces because of the change in geometry of the slip systems and the interface.

2.3.3 Multiphase

The criteria used to predict dislocation reactions across grain boundaries have been applied to bi-phase interfaces with mixed success, although the number of systems in which they have been applied is limited. The LRB criterion has been successfully applied to bi-phase interfaces in Ni-30Fe-20Al to predict the slip systems activated by the interface in response to a dislocation pile-up on the other side of it [88]. Even though the two phases have different crystal structures, FCC and BCC, TEM results confirmed the applicability of the LRB criterion to that system. However, in the Ti-48 at.% Al alloy system, stress-induced activation of interface sources was found to be

more determining than minimization of the Burgers vector of the residual dislocation at the hetero-phase interfaces for predicting the transfer of strain from the γ-TiAl to the α_2-Ti_3Al phase lamellae [104]. In that system, the lack of strain transmission is explained by the need for a high density of dislocations for twins to transfer across the boundary [105], the stress-induced activation of interface dislocation sources [105] and by an elastically-mediated transfer in the thinnest sections of the hard α_2-phase [106]. It is not clear how the unique features of bi-phase materials such as coherency stresses, misfit dislocations, or image stresses impact the applicability of strain transfer criteria. The models to predict strain transfer were developed for coarse grained materials and their applicability to grain boundaries or interfaces as the grain size or layer thickness decreases into the sub-micrometer and nanometer regimes has yet to be evaluated.

2.4 Inelastic strain recovery

Recovery of plastic strain is not generally something that occurs in appreciable amounts after deformation. However, several theoretical and experimental studies have reported plastic strain recovery in materials [107-110]. A molecular dynamics study of AgCu multilayers with cube-on-cube interfaces with $(111)_{\mathrm{Ag}}||(111)_{\mathrm{Cu}}$ interface habit planes, 2 nm layer thicknesses, strained to 4% along $[111]$ in tension, and deforming primarily by deformation twinning shows complete recovery of plastic strain [107, 111]. However, volume relaxation in two axis was not allowed to account for the Poisson effect and it is unclear if such a constraint on volume will lead to an unphysical plastic strain recovery mechanism. Plastic strain recovery has additionally been reported in an experimental study on Al and Au thin films with 65 and 50 nanometer grain sizes, respectively, strained up to 2%. However, the recovery was dependent on heating the specimens to 240 °C for Al and 210 °C for Au and the recovery was 0.33% and 0.35% strain respectively [108]. Computer simulations to explain the results for the Al and Au results tied the recovery to

dislocation retraction and grain boundary sliding [109]. Strain recovery has also been observed in a penta-twinned Ag nanowire strained *in situ* in a TEM. The authors attributed this behavior to leading partial dislocations, that had nucleated at the free surfaces, being blocked by the twin boundaries and upon unloading the partial dislocations were driven back to the free surface [110]. Though not clear from the *in situ* straining images published, the results of the molecular dynamics computer simulations that were reported with the experimental study showed this was the likely mechanism. It is not clear from the literature if inelastic recovery can be attained in bulk materials for materials strained higher than a few percent.

CHAPTER 3

EXPERIMENTAL PROCEDURES

3.1 Material processing

3.1.1 Flux melting and water quenching

Casting of AgCu eutectic was performed at Los Alamos National Laboratory under the guidance of Dr. Douglas Safarik. Rods with 8 mm diameters and masses between 12 and 32 g were cast. Pellets of Ag and Cu of 99.99% and 99.9% metals base purity respectively was measured to a composition of $Ag_{60}Cu_{40}$. A silica tube with an inner diameter of 8 mm and outer diameter of 10 mm was cleaned with ethanol. Cu was poured into the tube first, then Ag in the thought that Ag being more dense would cause gravitational mixing of the two phases. B_2O_3 flux that is 99.999% pure was crushed into chunks that fit in the silica tube and added to the tube until 2 inches above the Ag as shown in Fig. 3.1. The flux appears clear in the initial state and turns milky white opaque after absorbing moisture. The flux is added as it is thought to remove oxide particles from the melt and reduce heterogeneous nucleation sites [33]. The tube with its contents was then attached to a vacuum system consisting of a roughing pump and Ar gas tank. The tube was evacuated to 27 kPa before filling with Ar gas to a pressure of 108 kPa, which was repeated at least three times. If the flux was not clear, the tube under vacuum was then placed in the furnace which was set to 623 K for 30 minutes to remove any moisture from the flux. The tube was then backfilled with Ar to 108 kPa before ramping up the furnace to 1523 K. An observation window of the furnace allowed the melt to be visually monitored during the processing.

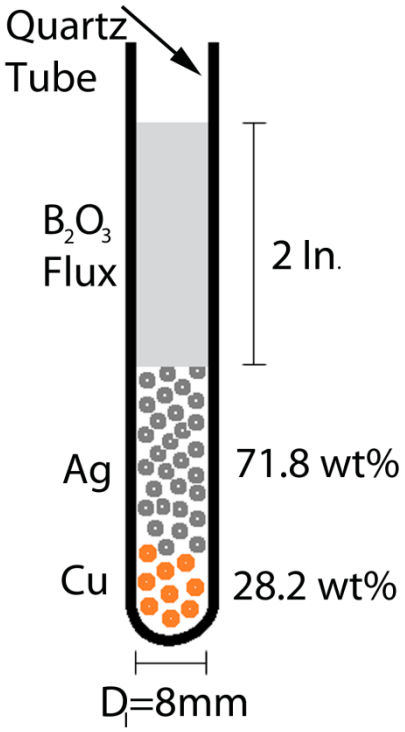

Figure 3.1: Diagram of tube with starting material and flux before melting.

Degassing of the melt was performed by slowly increasing the vacuum in increments of 4 to 8 kPa. Bubbles appearing in the melt were used as an indicator as to when to increase the vacuum. At each vacuum increment after the bubbles stopped forming, the tube was tapped and this generally resulted in further degassing. At a vacuum around 40 kPa, the vacuum increments were decreased as vigorous degassing occurred at this pressure.

When a vacuum of 27 kPa was reached and the valve to the roughing pump was fully opened, and the silica tube was again tapped to induce further degassing. This process was repeated until no more bubbles were observed in the melt. The melt was then left for at least 30 minutes. It was found that the degassing time for the heavier rods was only slightly longer than for the lighter rods, three to four hours for rods around 12 g compared to four to five hours for rods around 32 g. The tube was then removed from the furnace and air cooled to just before solidification. On cooling

the melt becomes darker but the melt has cooled too long in air when recalescence occurs and increases in brightness temporarily. Before the onset of recalescence, the tube is plunged into water and slowly swirled in the water to quench the melt to solid. The rod of material is then removed from the tube and placed in a Cu basket immersed in a bath of boiling water to dissolve the flux at the top of the rod.

3.1.2 Directional solidification

Directionally solidified $Ag_{60}Cu_{40}$ eutectic was cast as 10 mm diameter 50 mm length rods using a Bridgman furnace, Fig. 3.2, at a temperature of 1223 K and at removal rates of 0.46, 7.3, and 73 mm/hr. The material used to cast the directionally solidified material was the flux cleaned cast rods. These rods were placed in quartz tubes that were vacuum sealed to minimize exposure of the melt to gases such as oxygen that would become impurities. In the setup used, the Bridgman furnace moved upwards while the sample remained stationary in order to minimize vibrating of the sample as it was solidified. This produced a microstructure with the Ag and Cu-phases growing concurrently with a common [101] direction parallel to the rod axis. The samples were then annealed at 673 K for 4 hours at 1.3 kPa to reduce the solid solution of Ag in the Cu-phase to approach a value on the order of 0.5 at.% according to the phase diagram [112]. Near the end of the casting process some of the quartz tubes broke rendering a top portion of those rods as waste.

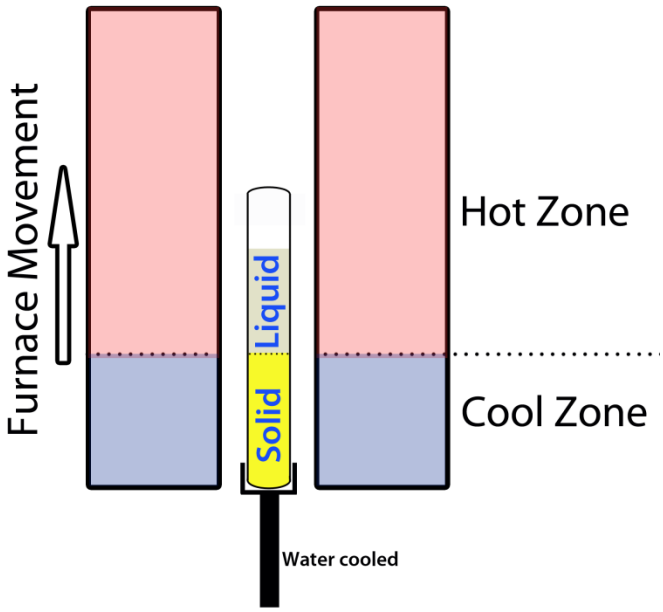

Figure 3.2: Diagram of Bridgman furnace and sample. Furnace is raised at a specified rate which solidifies the sample from the bottom to the top.

3.2 Mechanical testing

3.2.1 Split-Hopkinson pressure bar

Compressive loading was conducted using a split-Hopkinson pressure bar (SHPB) at room temperature. The specimens were placed between two elastic bars, the incident bar and transmitted bar, with strain gauges mounted to their surfaces to monitor propagating stress waves. A striker bar was launched at the incident bar initiating a stress wave that travels down the length of the incident bar. When the stress wave reaches the specimen a portion of the stress wave passes through it into the transmitted bar and the remaining portion is reflected back into the incident bar. Assuming one-dimensional wave propagation, the stress, strain and strain-rate were calculated from the measured strain gauge signals. These samples were compressed at a strain-rate of ~ 10^3 s^{-1}. A diagram of the SHPB setup can be seen in Fig. 3.3. More details about the SHPB

experiments can be found in [113, 114]. The SHPB tests were conducted by Dr. Owen Kingstedt as his doctoral work [115].

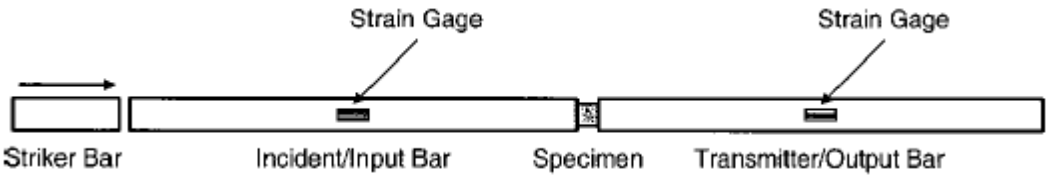

Figure 3.3: Split-Hopkinson pressure bar setup used for compression tests at a strain rate of 10^3 s^{-1}. Specimens are not tested to failure [116].

3.2.2 *In situ* transmission electron microscope straining

Tensile straining experiments were performed in the TEM using a Gatan single tilt heat/strain holder, Fig. 3.4. The sample is attached by two screws, one is stationary and the other can be displaced by a motorized mechanism. The displacement strains the sample in tension. Video of the deformation process is recorded by the CCD camera using VirtualDub video capture software.

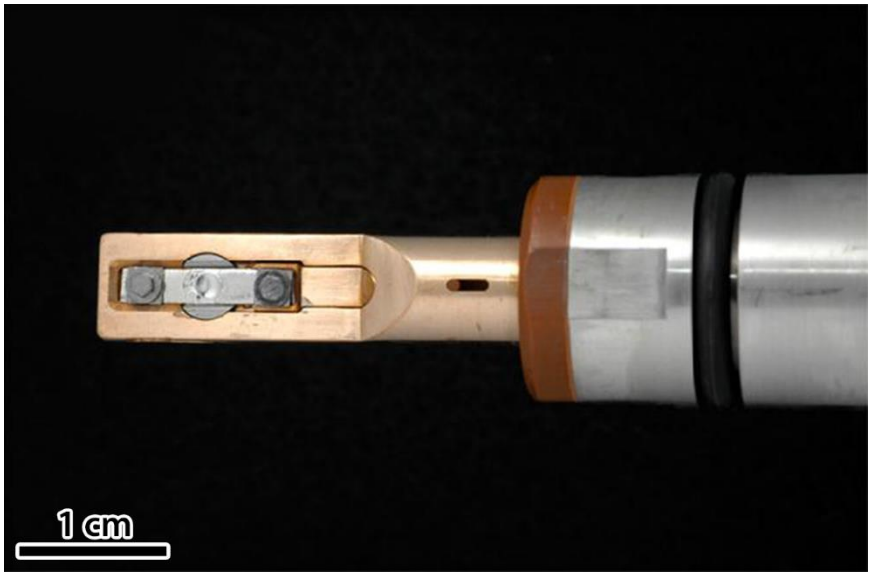

Figure 3.4: Gatan *in situ* TEM sample strain holder. Provides a tensile strain and allows one axis of tilt. Image courtesy of Jamey Fenske.

3.3 Transmission electron microscope sample preparation

3.3.1 Conventional preparation

Some of the samples fabricated for TEM observation were produced by using a conventional ion milling method. To begin, slices were cut using electrical discharge machining, EDM, to a thickness of approximately 800 µm. The slices were then mechanically polished on both sides to a target thickness of 100 µm. Care was taken to minimize induced damage by stepping down the coarseness of the grinding paper, it was assumed that damage induced was three times the coarseness. Mechanical polishing was done down to 1 µm diamond solution. 3 mm diameter samples where then punched out of the thinned slice. The discs were dimpled with a dimpling wheel starting with 6 µm diamond solution to a thickness of 52 µm, then 3 µm to a thickness of 34 µm, and, finally, 1 µm diamond solution until a thickness of approximately 25 µm at the thinnest region of the sample was reached. Ion milling was then performed using a Gatan PIPS with a cryo attachment with a typical starting voltage of 3 keV and incident angle of 4° while the sample was cooled. Once a hole developed, the voltage was dropped to 1 keV and the incident angle to 2° and milling continued for at least another hour.

3.3.2 Focused ion beam preparation

Focused ion beam machining (FIB) preparation was found to be more reliable and time effective for producing samples for TEM observation. Slices 800 µm thick were made using EDM and polished evenly on both sides to a thickness of 200 µm as described before, finishing with 1 µm diamond solution. A 3 mm-diameter disc sample was then punched out of the slice and ion milled at cryogenic temperature at 1.5 keV and incident angle of 2° for a few hours.

Samples were extracted from the polished disc by first depositing a protective layer of Pt on the surface with 3x3x30 μm dimensions. Trenches were then ion milled on both sides of the Pt at 30 kV and 20 nA. Next the foil was thinned to between 1 and 1.5 μm at 30 kV and 0.92 nA and 2° under tilt on both sides. The under tilt off-set the deflection of ions that occurs and results in a less wedge shaped specimen. A u-cut was then made on the sample leaving the sample connected at the top on both sides. A tungsten needle was attached to the sample foil with Pt before the foil was cut loose from the rest of the sample. The foil was then moved to a Cu mount and attached to it with Pt. Thinning of the foil to electron transparency was performed by ion milling first at an ion energy of 30 keV which was stepped down to 8 keV, and 5 keV and in some cases 2 keV in order to minimize milling damage.

3.3.3 Conventional *in situ* TEM straining sample preparation

A few samples for *in situ* straining in the TEM were fabricated by gluing Cu tabs to 3 mm-diameter discs with super glue. For this method, the 3 mm-diameter discs were first cut on two sides with a razor blade in order for them to be accommodated in the 2.5 mm wide TEM straining stage. The disc was then placed in the stage and Cu tabs placed on the top of the sample such that the electron transparent region is not covered. Superglue was then applied to regions where the disc and tabs met, capillary forces were relied upon to wick the glue between the two pieces.

After straining, the sample can be removed from the tabs with either acetone or a razor blade, and placed in a double tilt holder, however, great care must be observed. Acetone has the problem of depositing organics from the glue onto the electron transparent region. Using a razor blade was found to be a more effective means for removing the samples.

3.3.4 Focused ion beam preparation of samples for *in situ* TEM straining

FIB machining was used for fabricating location specific TEM samples for *in situ* TEM straining experiments [117, 118]. This concept can be applied to fabricating samples for in-situ straining in the TEM where the location of deformation can be controlled in addition to the load orientation to that specified area [117]. The challenge in this application is how to apply the load. To achieve this, the straining specimen geometry shown in Fig. 3.5 was employed [117].

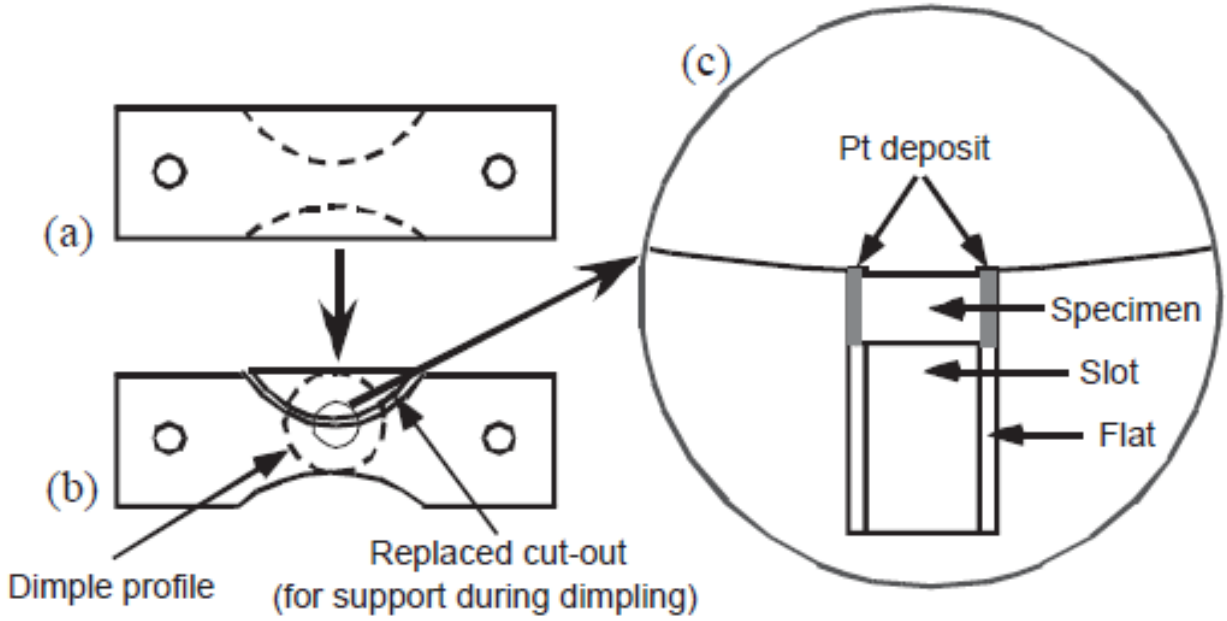

Figure 3.5: Sample geometry for in-situ straining TEM experiments that use FIB to choose location specific areas of material to strain. An A-symmetrical dog-bone is milled with FIB to which a specimen will be welded on with Pt [117].

The dogbones used were 304 stainless-steel or Cu and were the same geometry used by Field and Papin, Fig. 3.5 [117]. The dogbones are 250 µm thick and with a knife edge at the side where the sample is to be mounted. The dogbones are made asymmetrical to localize the load on the sample when it is mounted in place. At the knife edge, the FIB is used to create a clean flat edge 100 µm wide to minimize curtaining in the subsequent cuts, Fig. 3.6(a). Next the dogbone is cut edge-on 30 µm wide on both sides leaving a 10 µm thick rectangle at the knife edge, Fig. 3.6(b).

Then the dogbone is cut edge-on 22 µm wide leaving 2 µm to 5 µm of thickness, Fig. 3.6(c). Finally, an 18 µm wide and 30 µm deep cut into the dogbone is made, Fig. 3.6(d). This provides two ledges onto which a sample 20 µm wide can be placed.

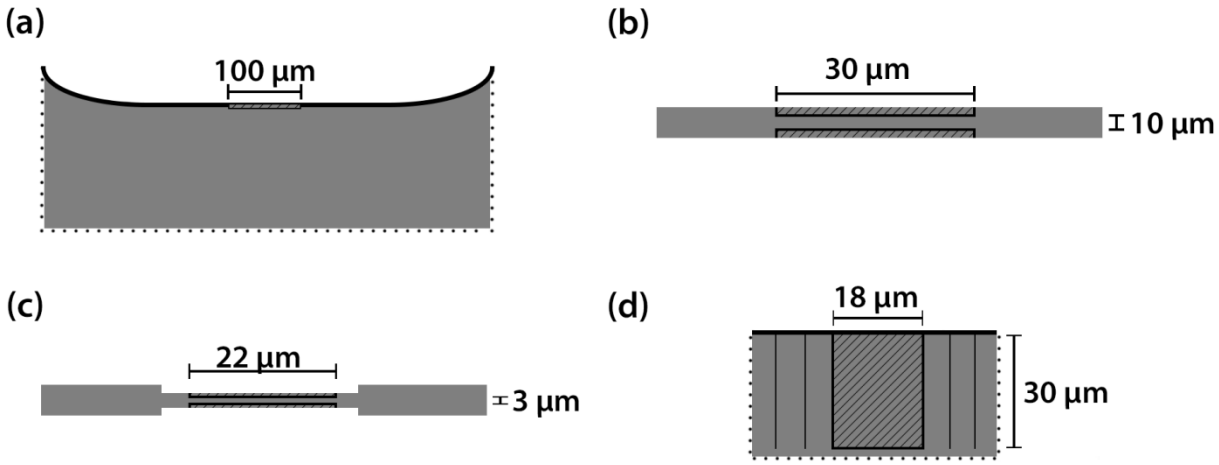

Figure 3.6: Pictorial describing the FIB cuts used to prepare the dogbones for mounting a sample in them. (a) and (d) are viewing the dogbone from the surface and (b) and (c) are viewing from edge on. Regions with diagonal lines denote where the cuts should be made.

The process to extract a foil for straining starts with selecting the area of material desired to be strained. Samples for straining were fabricated from both quenched and directionally solidified samples by using this method. The area selected for extraction was protected by a 3 µm thick 3 by 30 µm strip of Pt. Selecting how to extract the foil from the directionally solidified samples is aided by the growth direction of the material being [101], which was chosen to be the eventual beam direction for TEM due to the desire to image deformation twins. To do this the Pt was deposited on the sample in the geometry shown in Fig. 3.7. The directionally solidified cylinder was cut in half as shown and Pt strip deposited, in the same dimensions as before, such that the long direction of the Pt rectangle was perpendicular to the growth direction.

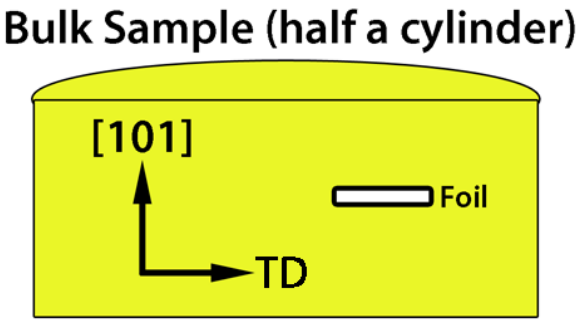

Figure 3.7: Half cylinder where the foil to be strained is extracted shown. The foil normal corresponds to the [101] growth direction. TD is the transverse direction.

The selected area was extracted by the method detailed for standard FIB sample extraction. After extraction the foil was mounted to the dogbone on the ledges and attached on both sides with Pt, Fig. 3.8. In the figure the locations of Pt, the loading direction, and sample are marked. In Fig. 3.8(b) the Cu appears darker than the Ag allowing them to be distinguished in the sample. Thinning of the foil was performed as previously described.

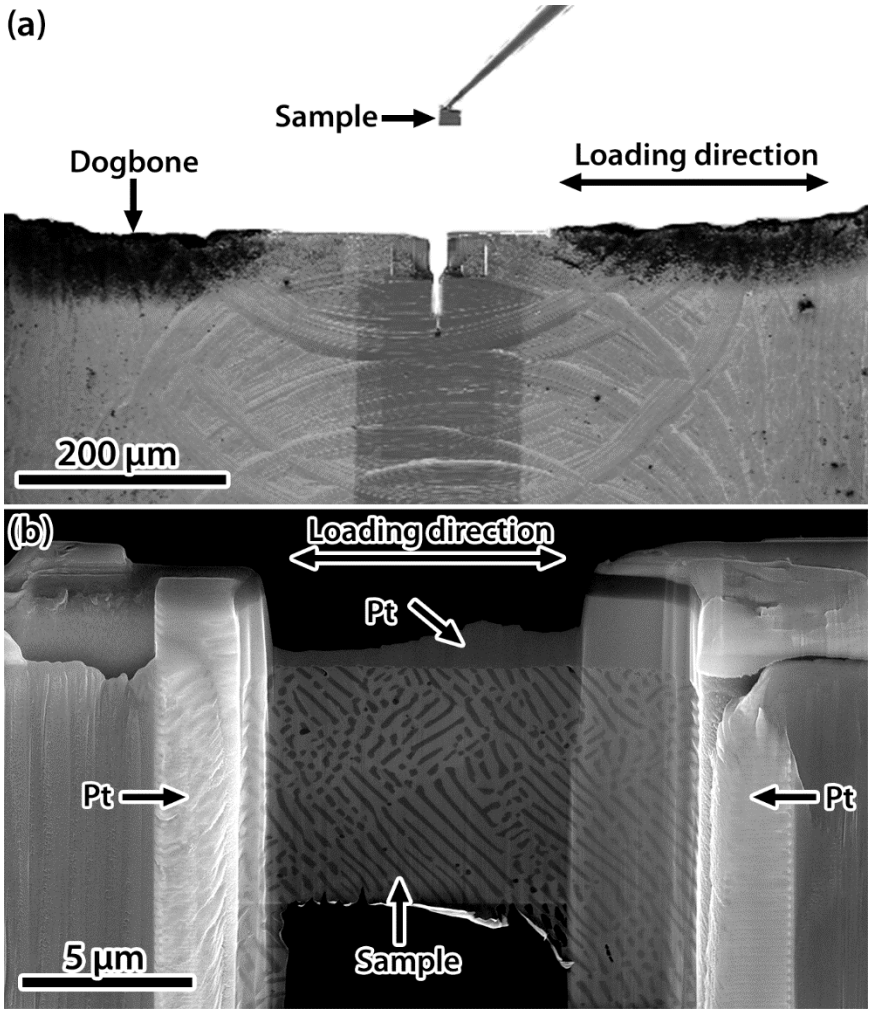

Figure 3.8: Placement of foil extracted by FIB onto strain bar diagramed in Fig. 3.5. (a) Foil attached to Omni probe needle being positioned to be glued with Pt to the dogbone strain bar. (b) Attached and thinned foil to be strained in tension.

3.4 Microstructural characterization

Diffraction contrast TEM analysis was conducted using a JEOL 2010 LaB_6 operating at 200 kV, or a FEI Tecnai TF30 operating at 300 kV, and high resolution TEM images were acquired using a FEI Tecnai F30 operating at 300 kV.

SEM and EBSD analysis was performed using a Zeiss LEO 1530 or FEI Inspect F, both with an electron backscatter detector and TSL/EDAX orientation imaging CCD. Samples for both were

prepared by mechanically polishing down to a 1 μm finish before ion milling at cryogenic temperatures with a Fischione 1050 argon ion mill. Final ion milling was at 1.0 keV accelerating voltage.

3.5 Indexing diffraction patterns

Diffraction patterns correspond to reciprocal space and contain spots, reflections, that correspond to types of planes. The diffraction spots are in the direction of the plane normal in real space, and the distance from the transmitted spot is the inverse of the interplanar spacing. The distance therefore is dependent on the plane and on the lattice spacing of the material. Ag and Cu have lattice parameters of 0.409 and 0.361 nm respectively which means the diffraction spots are distinct and well separated. For example, the selected area diffraction pattern presented in Fig. 3.9, shows the [101] zone axis of Cu and Ag with the diffraction spots corresponding to Ag being closer to the transmitted beam than the Cu diffraction spots.

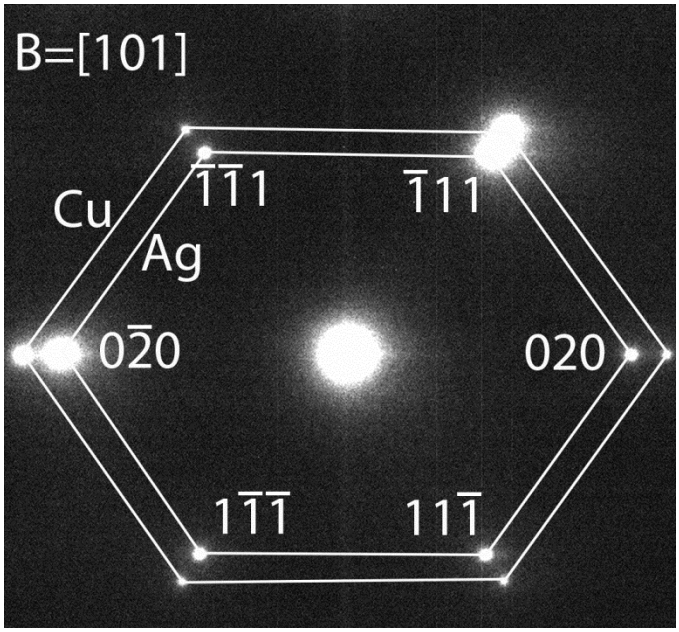

Figure 3.9: Diffraction pattern of Ag and Cu, in a cube-on-cube orientation relationship. The Ag spots are closer to the transmitted spot because Ag has a larger lattice parameter than Cu.

To characterize twins in FCC materials from the diffraction pattern, it is easiest to choose a ⟨101⟩ zone axis. Twinning in FCC materials corresponds to a 60° rotation about a ⟨111⟩. At this zone axis, this rotation results in a mirror of the crystal across the {111} twin plane. The diffraction spots associated with a matrix and twin at a zone axis of $[101]_m$ and $[110]_t$ is shown in Fig. 3.10; the diffraction spots associated with the matrix and the twin are distinguished by the subscripts m and t, respectively. Here the twin diffraction spots reside a distance of $\frac{1}{3}\langle 111\rangle$ along the systematic row of diffraction spots, refer to the arrow in Fig. 3.10(b).

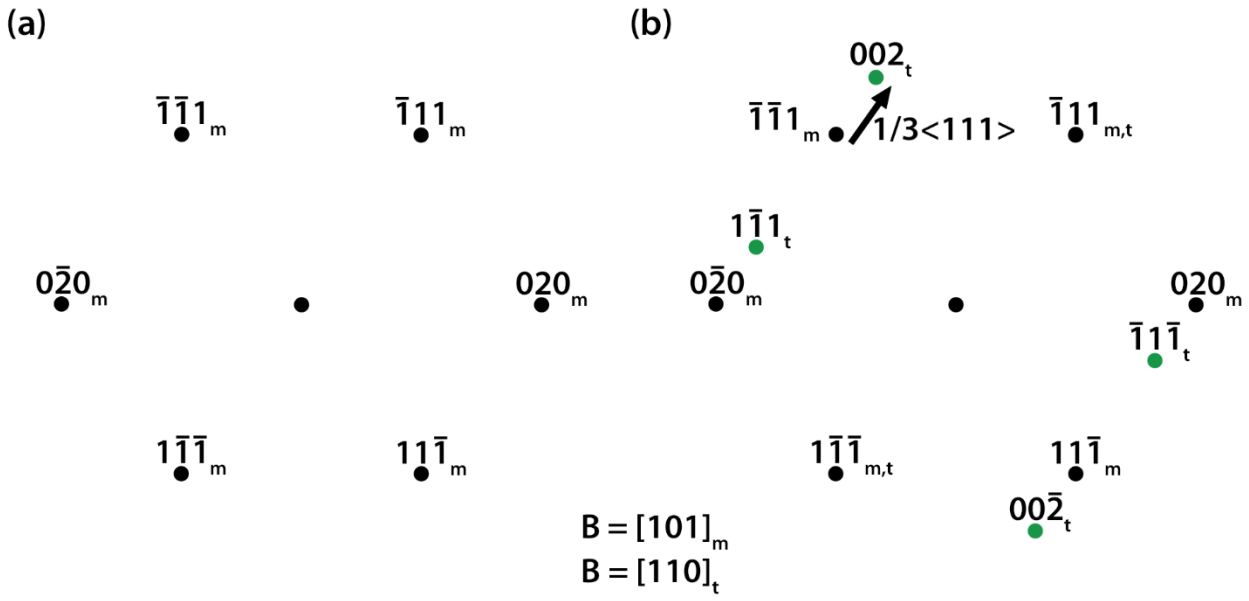

Figure 3.10: Indexed diffraction pattern for (a) matrix and (b) matrix and twin. Subscripts t and m represent matrix and twin, respectively.

Correctly indexing a twin diffraction pattern can be easily achieved using a cube with crystallographic directions marked on the surface with the origin defined as the center of the cube. The cube can be constructed using the template given in Fig. 3.11 (a). The beam direction is by convention out of the page, and diffraction vectors are perpendicular to the beam direction. The diffraction spots for the matrix can be indexed by viewing the cube in the orientation as shown in

Fig. 3.11 (b). Also, it should be remembered that for FCC crystal structures, the structure factor condition requires that all diffraction spots must contain h, k, and l that are all odd or all even. The indexed matrix is in Fig. 3.10 (a). To index the twin diffraction spots, the cube is rotated 60° about the twin plane normal, Fig. 3.11 (c). The twin plane is $(1\bar{1}\bar{1})$ in this case. The indexed diffraction pattern with both matrix and twin is shown in Fig. 3.10 (b). The twin indexes are indicated with a subscript t, and the twin diffraction spots are colored green. If the rotation of 60° had been in the opposite direction, the same crystal orientation for the twin would result, just different indexing. The twin rotations used throughout this document can be defined by the rotation matrixes given in Fig. 3.12. For a $(11\bar{1})$ twin plane the rotation matrix in Fig. 3.12(a), and for a $(\bar{1}11)$ twin plane the rotation matrix in Fig. 3.12(b).

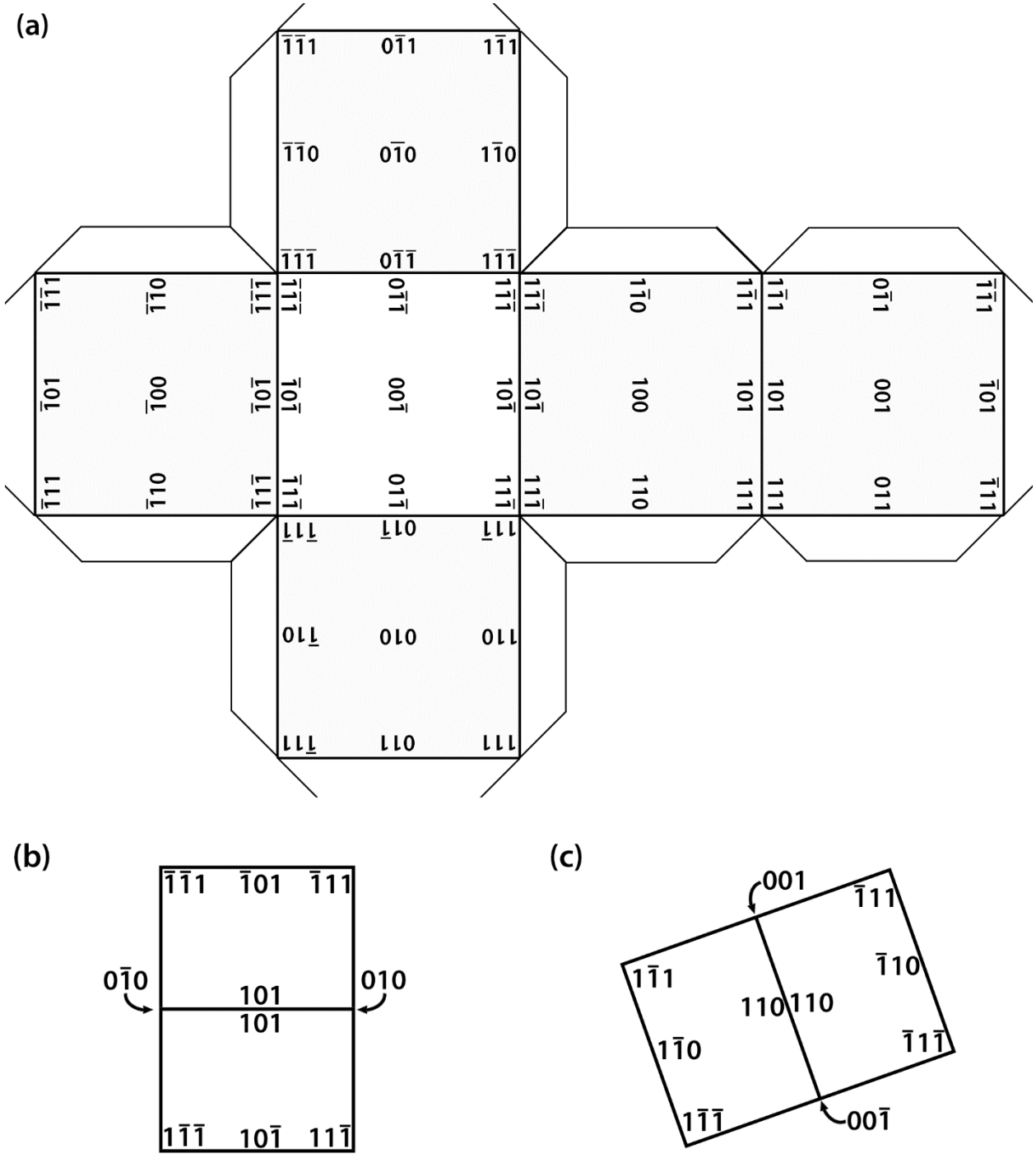

Figure 3.11: (a) Pattern for a cube with crystallographic directions marked when the origin is in the center of the cube. (b) and (c) Viewing cube at orientations relevant to indexing the diffraction patterns in 3.10.

(a)

$$\begin{bmatrix} 2/3 & 2/3 & 1/3 \\ -1/3 & 2/3 & -2/3 \\ -2/3 & 1/3 & 2/3 \end{bmatrix}$$

(b)

$$\begin{bmatrix} 2/3 & 1/3 & -2/3 \\ -2/3 & 2/3 & -1/3 \\ 1/3 & 2/3 & 2/3 \end{bmatrix}$$

Figure 3.12: Rotation matrixes to get to twin orientation for (a) $(11\bar{1})$ and (b) $(\bar{1}11)$ twin planes.

CHAPTER 4

RESULTS[1]

The results presented in this chapter are intended to show how different Ag/Cu interface types impact dislocation-interface interactions. Two different processing methods, (i) directional solidification and (ii) water quenching, were employed to produce material with different microstructures. The first two sections are broken down into initial microstructures, bulk mechanical response, and deformation microstructures for each of the two processing methods. The last section contains direct observations of dislocation/interface interactions using *in situ* TEM straining experiments for the different interface types.

4.1 Directionally solidified AgCu eutectic

4.1.1 Initial microstructures

Initial microstructures are presented for three growth rates in the order of slowest to fastest. The microstructure of the directionally solidified alloy with a growth rate of 0.46 mm/hr consists of Cu globular platelets elongated in, and discontinuous along, the growth direction in a Ag matrix with a bi-layer thickness of 2200 nm, Fig. 4.1. The cross-sectional view shows the dispersion of the Cu-phase in the Ag matrix, Fig. 4.1(a). The discontinuous nature of the elongated Cu-phase along the growth direction is seen in Fig. 4.1(b). The crystal orientation along the growth direction was determined by EBSD to be $[101]$ in both phases, Fig. 4.2(a). An EBSD map of the same area with the frame of reference perpendicular to the growth direction shows there are annealing twins, marked by arrowheads at a colony boundary, Fig. 4.2(b). The orientation relationship between Ag and Cu, determined by EBSD, is cube-on-cube. When observing a larger area with EBSD, Fig.

[1] Some of the results presented in this chapter have been previously published in the following publication: B.P. Eftink, N.A. Mara, O.T. Kingstedt, D.J. Safarik, J. Lambros, I.M. Robertson. Anomalous deformation twinning in coarse-grained Cu in Ag60Cu40 composites under high strain-rate compressive loading, Materials Science and Engineering: A 618 (2014) 254-261. Reprinted with permision from the publisher.

4.3, it was found that most of the colonies have similar orientations with respect to neighboring colonies and these form groups of colonies with similar orientations. For example, at the top of Fig. 4.3(b) there are groups of colonies near the [101] and [111] orientations. The EBSD results illustrate that the growth direction is constant with crystallographic rotations occurring about the growth direction.

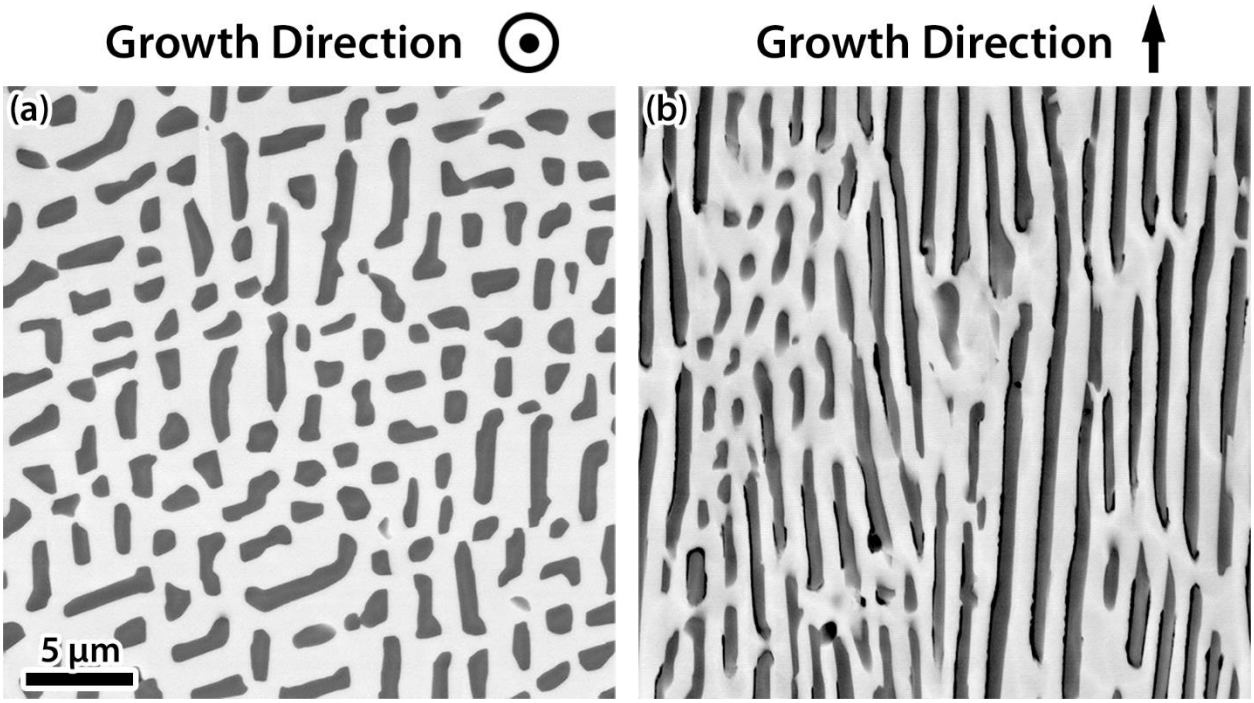

Figure 4.1: SEM backscattered electron images of the undeformed directionally solidified AgCu eutectic with 2200 nm bi-layer thickness and growth rate of 0.46 mm/hr. Ag appears lighter than Cu. (a) Growth direction into the page. (b) Growth direction in the vertical direction.

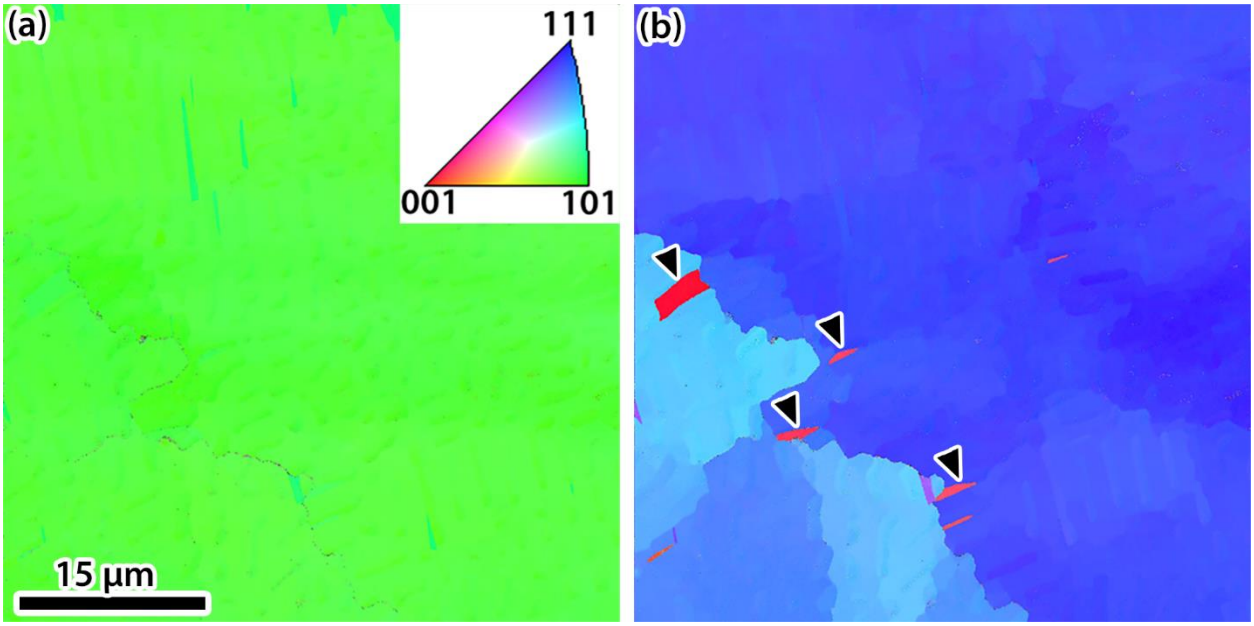

Figure 4.2: EBSD orientation map of directionally solidified AgCu eutectic with 2200 nm bi-layer thickness and 0.46 mm/hr growth rate. (a) Map showing orientation of sample surface normal which corresponds to the growth direction. (b) Map showing orientation perpendicular to the sample surface normal, the same area as (a). Arrowheads mark twinned regions. Step size for EBSD was 50 nm.

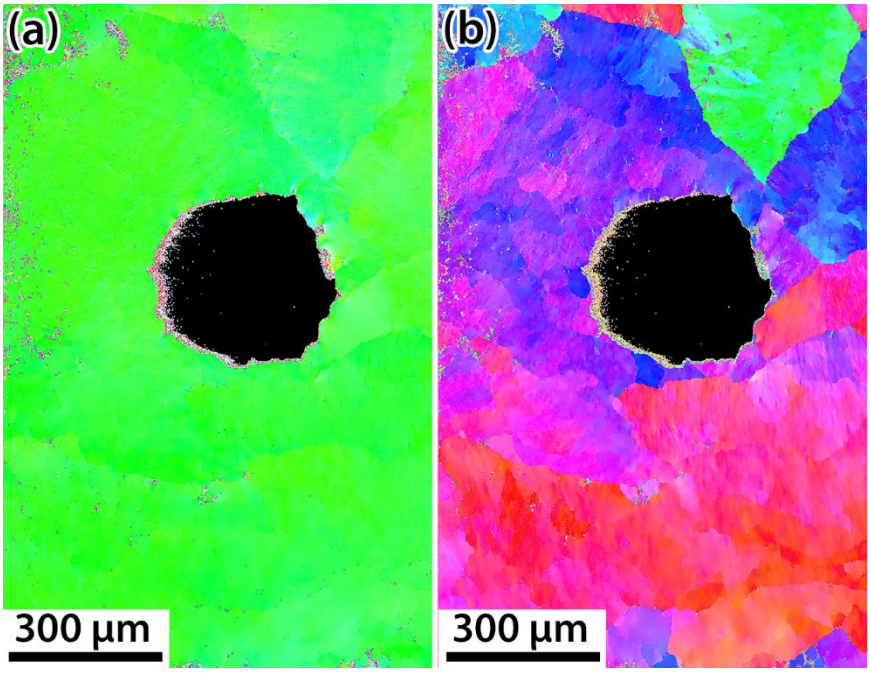

Figure 4.3: EBSD orientation map of directionally solidified AgCu eutectic with 2200 nm bi-layer thickness and 0.46 mm/hr growth rate. (a) Map showing crystal orientation of sample surface normal which corresponds to the growth direction. (b) Map showing crystal orientation perpendicular to the sample surface normal. Black region is a hole in the sample made for TEM.

The as-cast material has a low dislocation density in both Ag and Cu with the dislocation density being highest in Ag. Dislocation half-loops are seen to be emitted from the Ag/Cu interfaces into the Ag and examples are indicated by arrowheads in Fig. 4.4(a). Elastic stress concentration centers can be seen in the form of distortions extending from the interface into the Ag; examples are indicated by arrows. The preferred interfaces are $(\bar{1}11)_{\mathrm{Ag}}||(\bar{1}11)_{\mathrm{Cu}}$ and $(11\bar{1})_{\mathrm{Ag}}||(11\bar{1})_{\mathrm{Cu}}$, which are marked by the white dotted lines. On examining the interface structure at higher spatial resolution, it is found that the interface between Ag and Cu is {111} with irregularly spaced {111} steps. An example of this structure is shown in the high-resolution image presented in Fig. 4.4(b); the estimated location of the interface is indicated by the white line. The steps on the interface vary in height with some being just one atomic plane high and others being

several; these steps account for the interface curvature. Misfit dislocations, present as extra planes in Cu, occur approximately every 8-11 {111} planes and are marked by black circles. These misfit dislocations account for the lattice mismatch between the two phases; the lattice parameters for Cu and Ag are 3.610 $\dot{A}$ and 4.090 $\dot{A}$, respectively. The spacing of the misfit dislocations matches that of previous findings of a quenched $Ag_{60}Cu_{40}$ material [119]. Periodic elastic strain is observed between the misfit dislocations and is marked by the arrows in the Ag-phase.

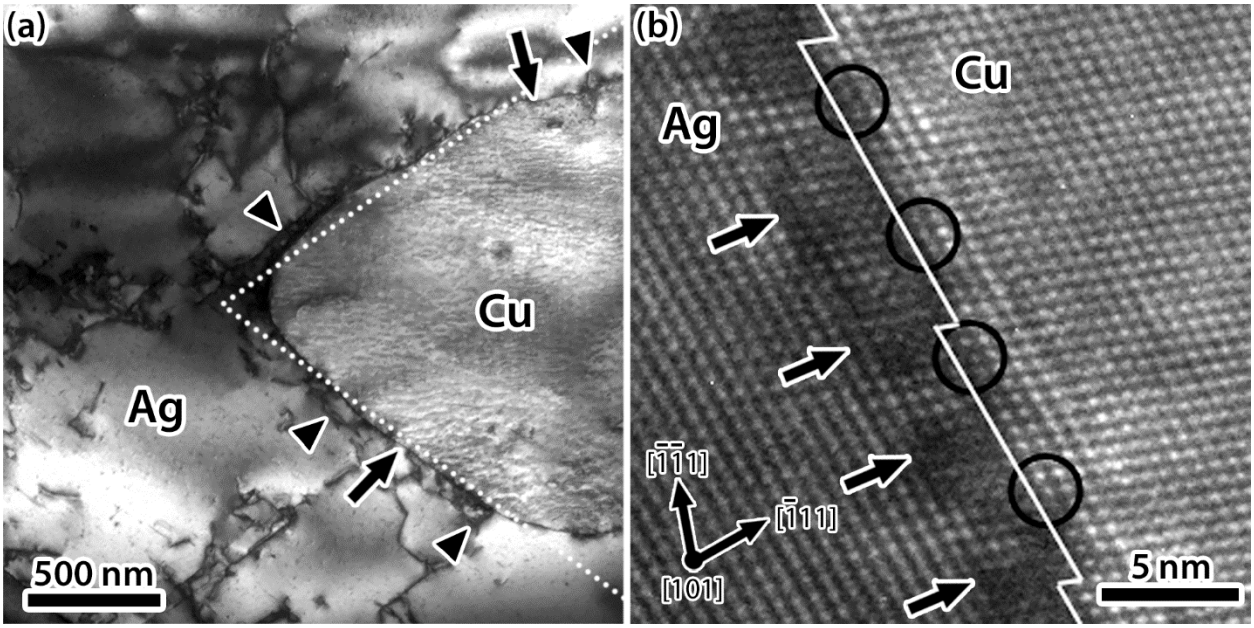

Figure 4.4: (a) Bright-field and (b) high-resolution electron micrographs of AgCu eutectic with 2200 nm bi-layer thickness and 0.46 mm/hr growth rate. Arrowheads mark dislocation half loops and arrows mark elastic distortions in (a). The dotted lines in (a) are the $(\bar{1}11)$ and $(11\bar{1})$ planes, the solid white line in (b) is the estimated location of the interface. Misfit dislocations and periodic elastic strain are marked in (b) with black circles and arrows, respectively.

The microstructure of the directionally solidified alloy with a growth rate of 7.3 mm/hr consists primarily of Cu globular platelets elongated in and discontinuous along the growth direction in a Ag matrix, as shown in the backscattered electron images presented in Fig. 4.5. A smaller fraction, around 15%, of the material has a lamellar structure, also elongated in the growth direction. In the cross-sectional view showing the dispersion of the Cu-phase in the Ag matrix, regions with the

lamellar structure are marked by arrowheads, Fig. 4.5(a). The discontinuous nature of the elongated Cu-phase along the growth direction is seen in Fig. 4.5(b). The bi-layer thickness of this material is 1100 nm. The difference between this growth rate and the slower rate is the introduction of a lamellar structure and a decrease in bi-layer thickness.

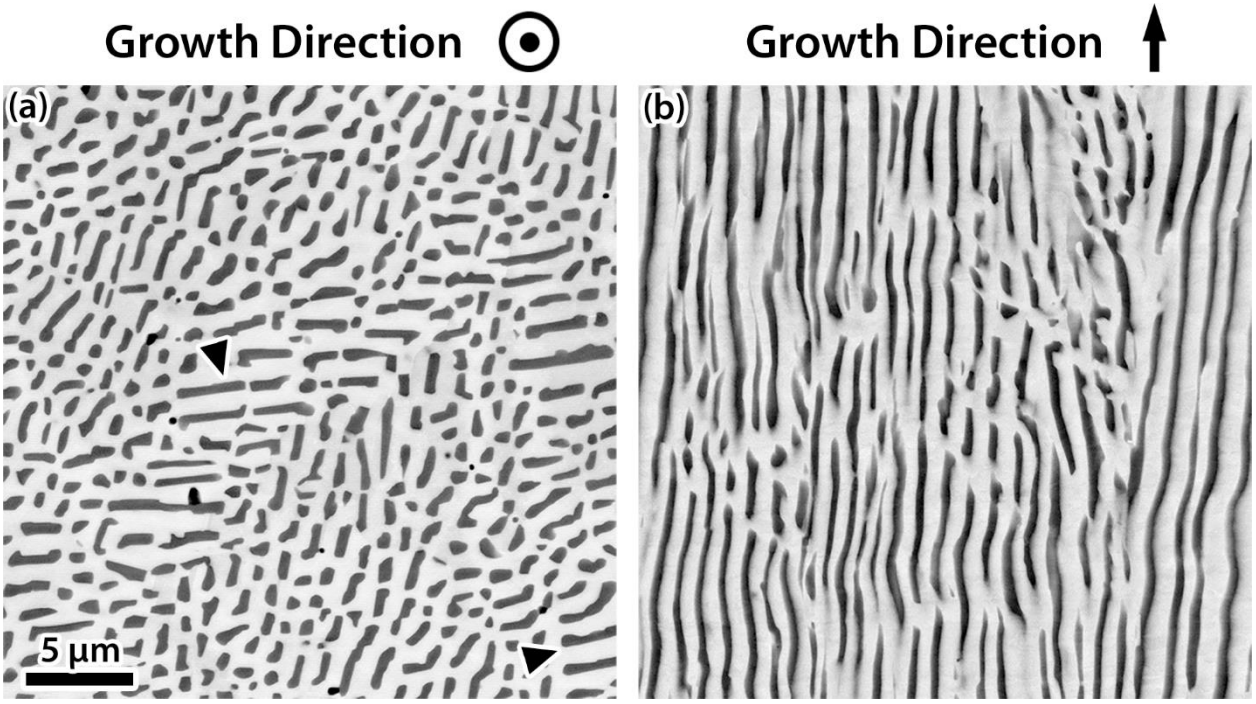

Figure 4.5: SEM backscattered electron images of the undeformed directionally solidified material with 1100 nm bi-layer thickness and growth rate of 7.3 mm/hr. Ag appears lighter than Cu. (a) Growth direction into the page. (b) Growth direction in the vertical direction. Arrowheads in (a) mark lamellar regions.

The crystal orientation along the growth direction was determined by EBSD to be ⟨101⟩ in both phases, Fig. 4.6(a). An EBSD map of the same area with the frame of reference perpendicular to the growth direction shows a twin orientation relationship between Ag and Cu in select regions, which comprises approximately 15% of the sample, Fig. 4.6(b). 85% of the sample has a cube-on-cube orientation relationship between Ag and Cu. Examples of twin regions are marked by arrowheads in Fig. 4.6(b). When the Ag and Cu have a twin orientation relationship, Ag and Cu will have growth directions of $[101]_{Ag}$ and $[110]_{Cu}$ or $[011]_{Cu}$. By comparing where the twin

regions are with the image quality map in Fig. 4.6(c), such regions are found to have a lamellar morphology whereas the cube-on-cube regions have a globular platelet morphology. On mapping a larger, 400 x 1100 μm, area with EBSD, Fig. 4.7, only similarly oriented colonies were found. Fig. 4.7 shows the crystal orientation referenced along the (a) growth direction and (b) perpendicular to the growth direction, both of the same area. The orientations referenced perpendicular to the growth direction indicate neighboring colonies are rotated small amounts about the growth direction with respect to each other. This is consistent with the larger bi-layer thickness material. Regions with the twin orientation relationship between Ag and Cu are seen to be distributed throughout the material and a few regions are marked with arrowheads.

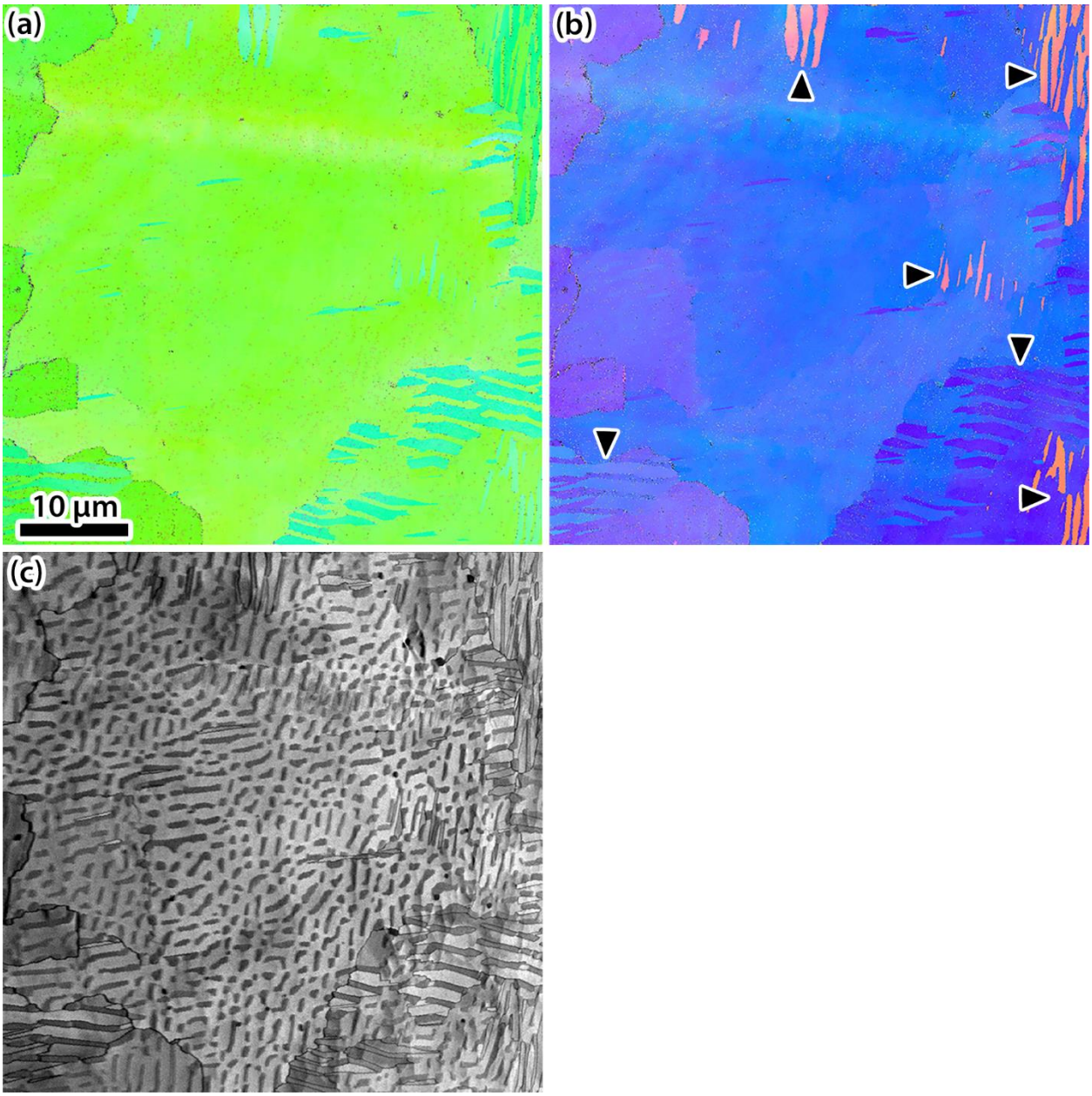

Figure 4.6: EBSD orientation map of $Ag_{60}Cu_{40}$ with 1100 nm bi-layer thickness and 7.3 mm/hr growth rate. (a) Map showing orientation of sample surface normal which corresponds to the growth direction. (b) Map showing orientation perpendicular to the sample surface normal, same area as (a). (c) Image quality map of the scan, Ag appears lighter than Cu. Arrowheads mark twinned regions.

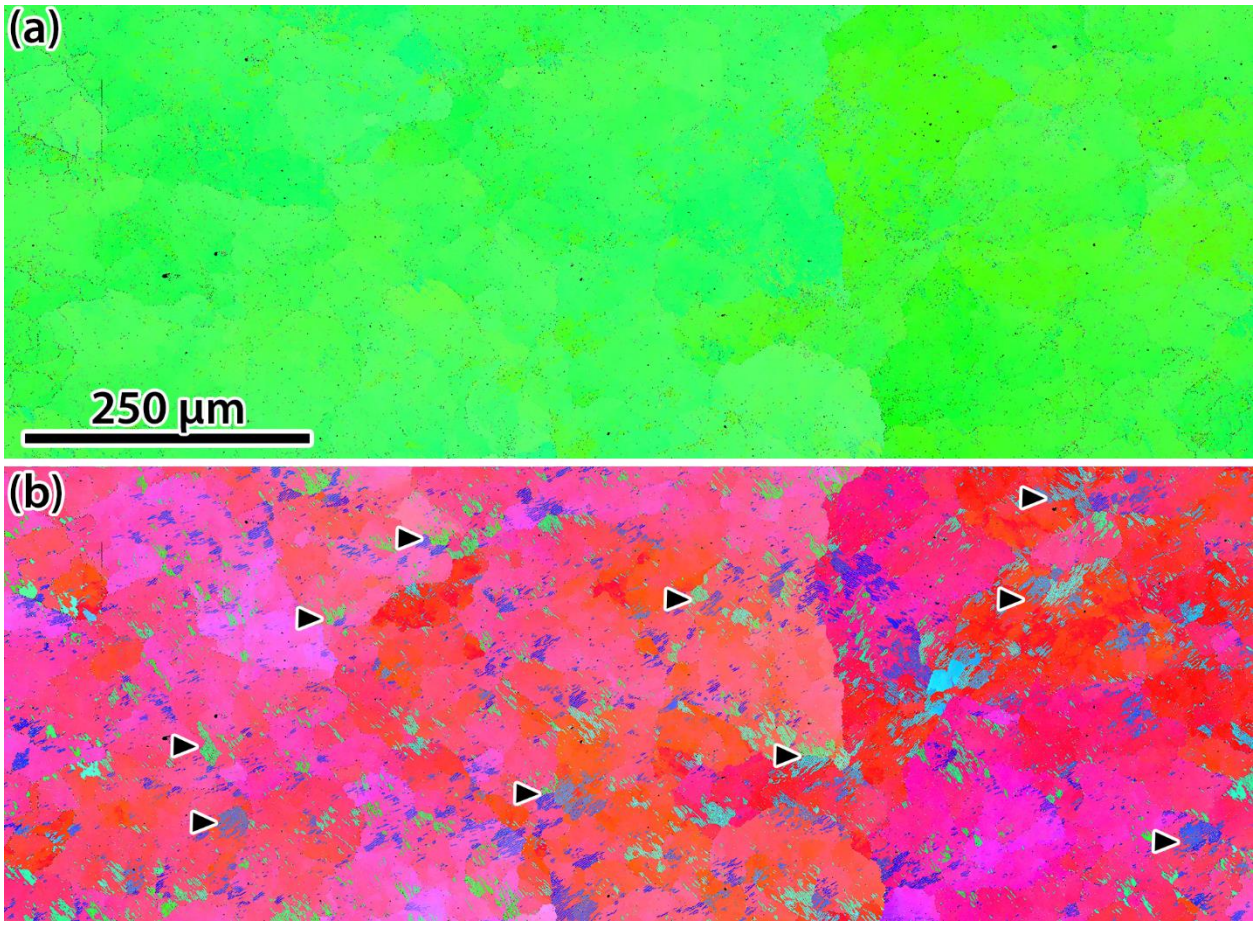

Figure 4.7: EBSD orientation map of $Ag_{60}Cu_{40}$ with 1100 nm bi-layer thickness and 7.3 mm/hr growth rate. (a) Map showing crystal orientation of sample surface normal which corresponds to the growth direction. (b) Map showing crystal orientation perpendicular to the sample surface normal, same area as (a).

Examining the lamellar regions in the TEM shows both Ag and Cu are of low dislocation density, Fig. 4.8(a). Also evident in this image, especially in the Cu-phase is the damage caused by ion milling, which is present as both black dots and the streaking that is tilted slightly off horizontal. The orientation relationship between Ag and Cu is a twin, however, there is a 2° rotation between the $(\bar{1}11)$ twin plane shared between Ag and Cu. This rotation is evident in the selected area diffraction pattern presented in Fig. 4.8(b). The interface habit plane, as determined from Fig. 4.8(b), is approximately $(\bar{3}13)_{Ag}||(\bar{1}12)_{Cu}$, which makes these incoherent twin

interfaces. Regions of the interfaces contain curvature and variations in the habit plane of up to 5° about the $\langle 101 \rangle$ growth direction generally toward the $(\bar{1}11)_{\mathrm{Ag}}||(\bar{1}11)_{\mathrm{Cu}}$ were common.

Regions of globular platelets of Cu in a Ag matrix in the 1100 nm bi-layer thickness material has a low density of dislocations in both Ag and Cu. Dislocations are predominantly in the Ag-phase emitting from the interfaces, a few examples are marked with arrowheads in Fig. 4.8(c). The orientation relationship between Ag and Cu is cube-on-cube, as shown in the selected area diffraction pattern presented in Fig. 4.8(d). The preferential interface planes are $(\bar{1}11)$ and $(11\bar{1})$, resulting in the globular platelet structure similar to the larger length-scale material.

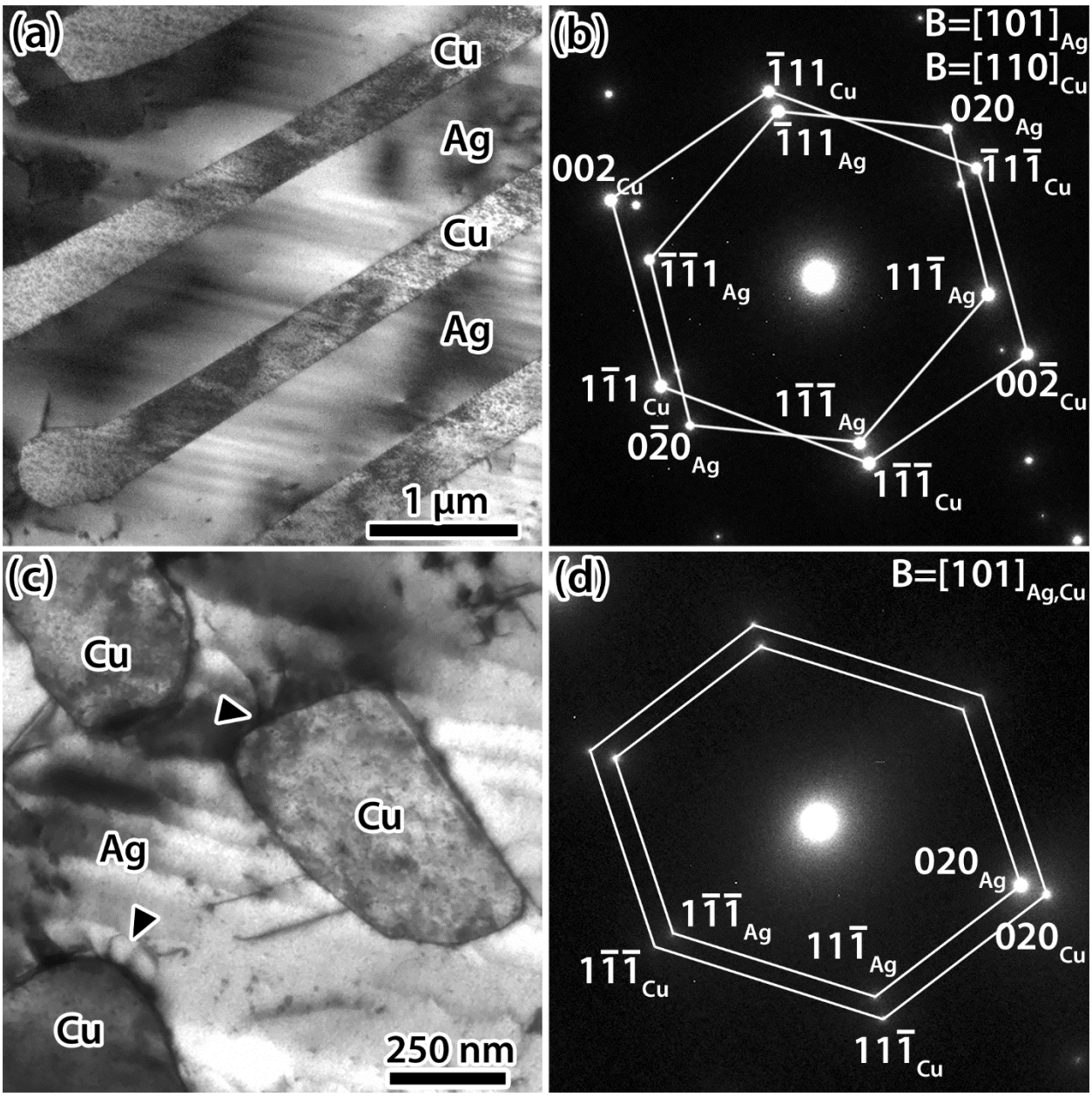

Figure 4.8: (a) Bright-field electron micrograph and (b) corresponding selected area diffraction pattern of a region with incoherent twin interfaces between Ag and Cu. (c) Bright-field electron micrograph and (d) corresponding selected area diffraction pattern of a region with cube-on-cube interfaces between Ag and Cu. Material was grown at 7.3 mm/hr and has a bi-layer thickness of 1100 nm. Arrowheads mark dislocations emitting from Ag/Cu interfaces.

At the fastest growth rate, 73 mm/hr, the microstructure is primarily Ag and Cu lamellae elongated in and discontinuous along the growth direction. An example of this microstructure is shown in the backscattered electron image presented in Fig. 4.9. The cross-sectional view, Fig.

4.9(a), shows the dispersion of the Cu-phase in the Ag matrix, and the discontinuous nature of the elongated Cu-phase along the growth direction is seen in Fig. 4.9(b). A smaller fraction, around 34%, of the material has the globular platelet structure. The bi-layer thickness of the material is 500 nm. Increasing the growth rate resulted in increasing the proportion of lamellar structure and decreasing the bi-layer thickness.

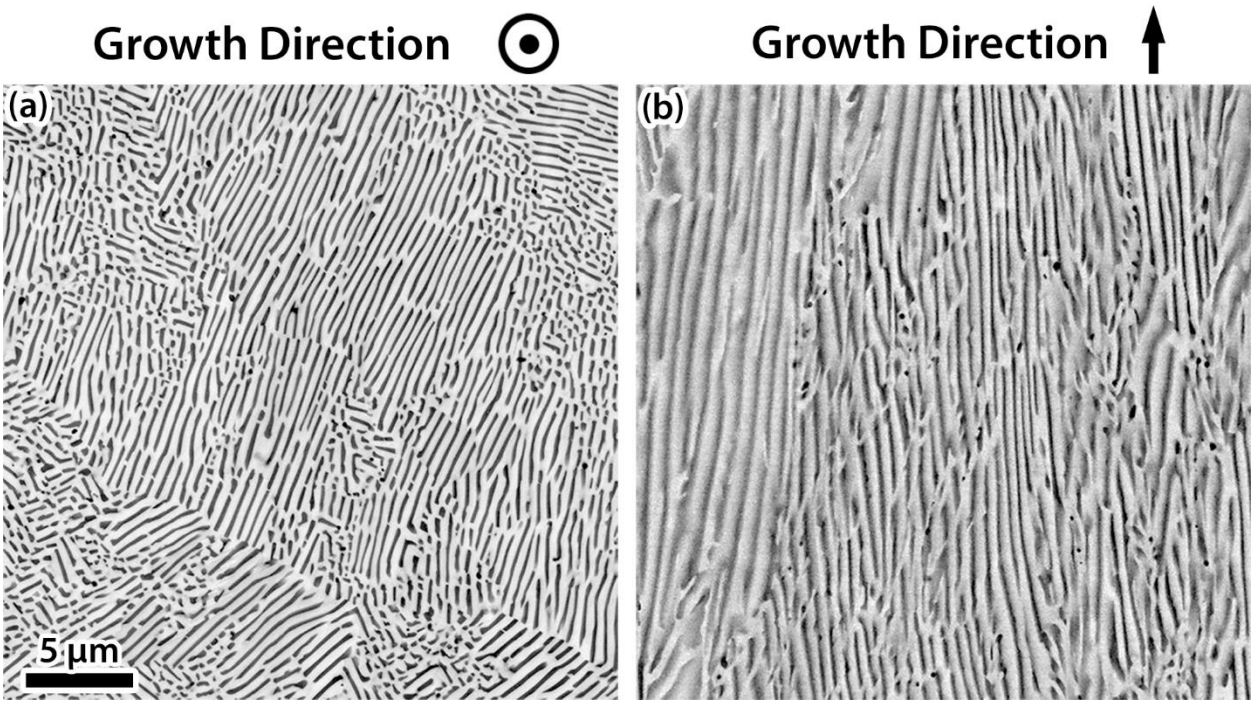

Figure 4.9: SEM backscattered electron images of the undeformed directionally solidified material with 500 nm bi-layer thickness and growth rate of 73 mm/hr. Ag appears lighter than Cu. (a) Growth direction into the page. (b) Growth direction in the vertical direction.

The crystal orientation along the growth direction was determined by EBSD to be ⟨101⟩ in both phases, Fig. 4.10(a). An EBSD map of the same area with the frame of reference perpendicular to the growth direction shows there is a twin orientation relationship between Ag and Cu comprising greater than 66% of the sample. The rest of the material had a cube-on-cube orientation relationship. Note at a 50 nm step size the Cu layers are three points wide, which is insufficient to distinguish all of the Cu layer orientations such that the proportions of orientation

relationships is skewed towards cube-on-cube. Therefore the value listed should be considered the minimum percentage with twin-oriented interfaces. The backscattered electron micrograph presented in Fig. 4.10(c) shows the area from which the EBSD map was acquired. Orientation maps for a surface perpendicular to the growth direction are shown in Fig. 4.11. In Fig. 4.11(a) the orientation map shows the crystal orientation in the vertical (growth) direction and Fig. 4.11(b) shows it perpendicular to the growth direction. This map, Fig. 4.11(b), confirms the colonies are columnar in nature. Because the surface is perpendicular to the growth direction, not all of the lamellae are observed edge-on and the lamellar bi-layer thickness appears to be greater than 500 nm. Even in this case, the percentage of twin interfaces was determined to be 66%.

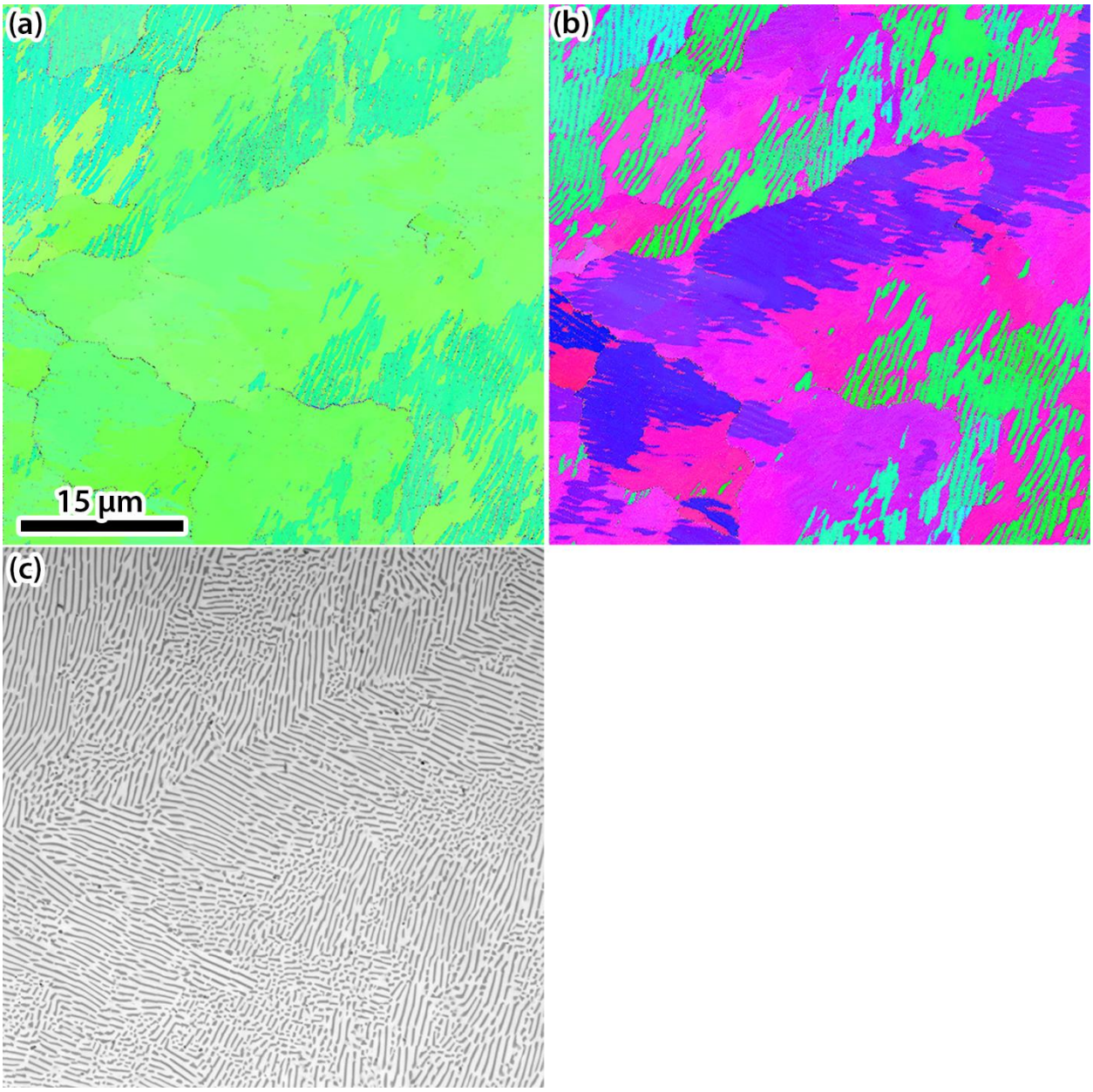

Figure 4.10: EBSD orientation map of $Ag_{60}Cu_{40}$ with 500 nm bi-layer thickness and 73 mm/hr growth rate. (a) Map showing orientation of sample surface normal which corresponds to the growth direction. (b) Map showing orientation perpendicular to the sample surface normal, same area as (a). (c) Backscattered electron micrograph of the same area, Ag-phase appears lighter than Cu.

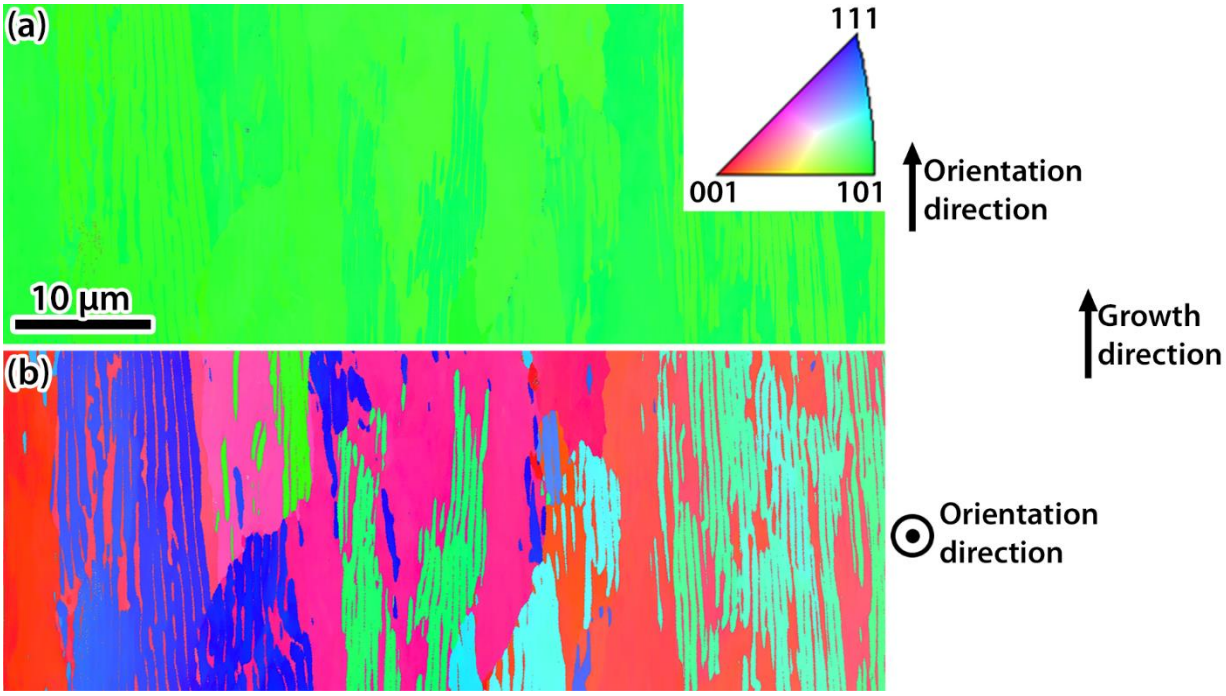

Figure 4.11: EBSD orientation map of $Ag_{60}Cu_{40}$ with 500 nm bi-layer thickness and 73 mm/hr growth rate with the sample surface perpendicular to the growth direction and the growth direction as the vertical direction in the maps. (a) Map showing orientation of sample in the vertical direction which corresponds to the growth direction. (b) Map showing orientation of the sample surface normal which is perpendicular to the growth direction.

A region with Ag and Cu lamellae and 500 nm bi-layer thickness is presented in the bright-field electron micrograph with a corresponding selected area diffraction pattern in Figs. 4.12(a) and (b). A low dislocation density is observed in both Ag and Cu with dislocations present at the interface and slightly preferentially in Ag. There is also evidence of elastic strain emanating from the interface into the Ag-phase; examples are marked by arrowheads in Fig. 4.12(a). Moreover, especially in the Cu-phase, there is evidence of the damage caused by ion milling. The orientation relationship between Ag and Cu is a twin, however, there is on average a 1.7° rotation between the $(\bar{1}11)$ twin plane shared between Ag and Cu, as shown in the diffraction pattern in Fig. 4.12(b). The interface habit plane varies and measurements from several colonies indicates the greatest number of interfaces are 20.2° and 18.5° away from the coherent twin habit plane in Ag and Cu,

respectively. This corresponds to the twin habit plane being approximately $(\bar{3}13)_{Ag}||(\bar{1}12)_{Cu}$. Therefore, these interfaces are incoherent twin interfaces. Variations in the habit plane of up to 10° about the $\langle 101 \rangle$ growth direction toward the $(\bar{1}11)_{Ag}||(\bar{1}11)_{Cu}$ twin plane were observed. This can be seen in the histogram in Fig. 4.13 which shows the distribution of angle away from the coherent twin plane of the habit plane in Ag, measured from 68 interfaces. The peak occurrence is a Ag habit plane 20.2° away from the $(\bar{1}11)_{Ag}||(\bar{1}11)_{Cu}$ coherent twin plane, and the occurrences decrease for habit planes closer to coherent twin. The histogram also shows interface habit planes greater than 21° from the coherent twin interface are not favorable. The incoherent twin type interfaces are stepped as illustrated in the high resolution electron micrograph shown in Fig. 4.12(c). On the Ag side, the interfaces are $(\bar{1}11)_{Ag}$ with $(\bar{1}\bar{1}1)_{Ag}$ steps whereas for Cu the interface is $(\bar{1}11)_{Cu}$ with $(002)_{Cu}$ steps. The incoherent twin interfaces do not contain periodic misfit dislocations, however, randomly spaced dislocations are present in these interfaces.

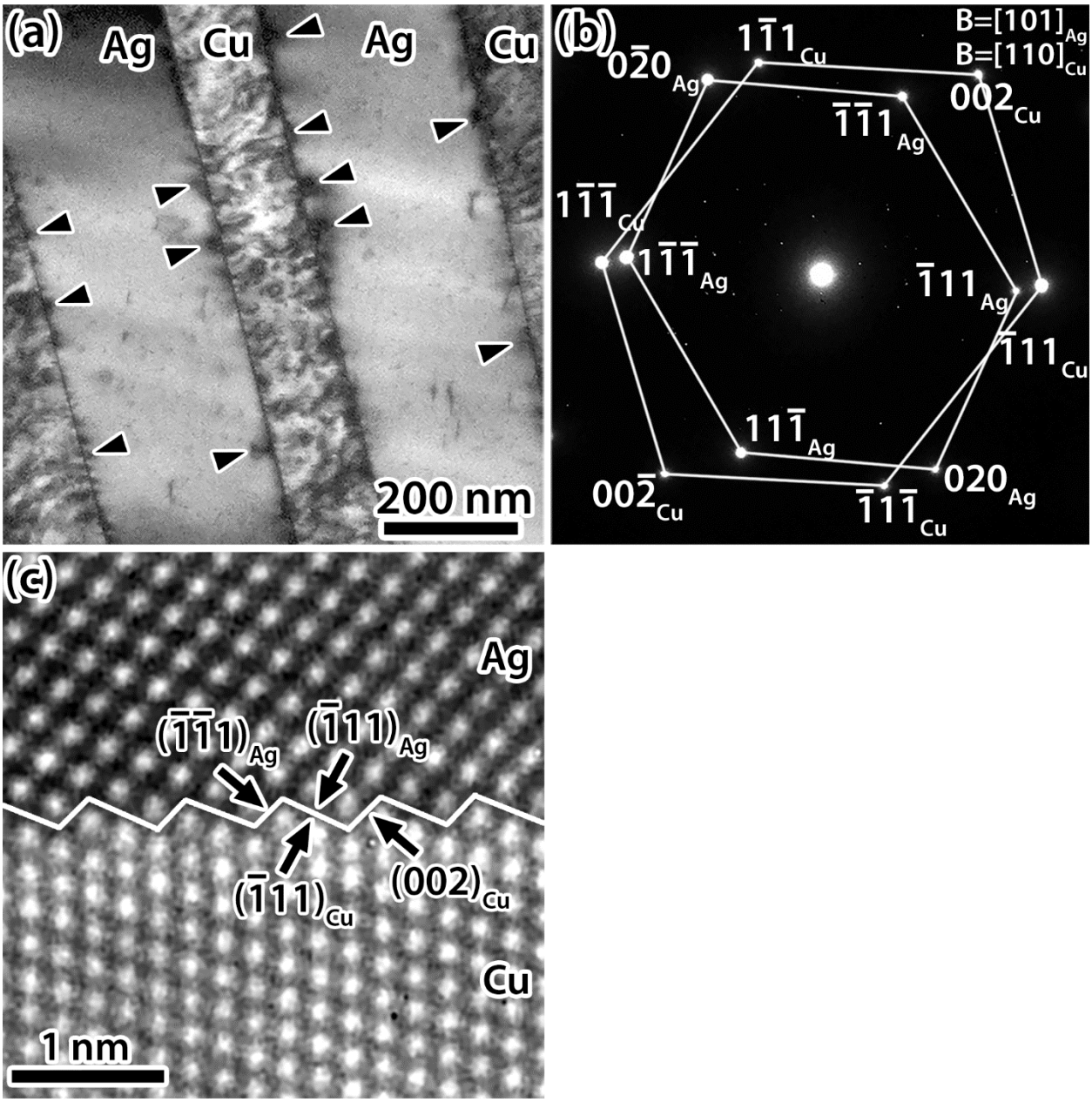

Figure 4.12: (a) Bright-field electron micrograph and (b) corresponding selected area diffraction pattern of a region with incoherent twin interfaces between Ag and Cu. (c) High resolution electron micrograph of an incoherent twin interface. Arrowheads mark interfacial dislocations. Material was grown at 73 mm/hr and has 500 nm bi-layer thicknesses.

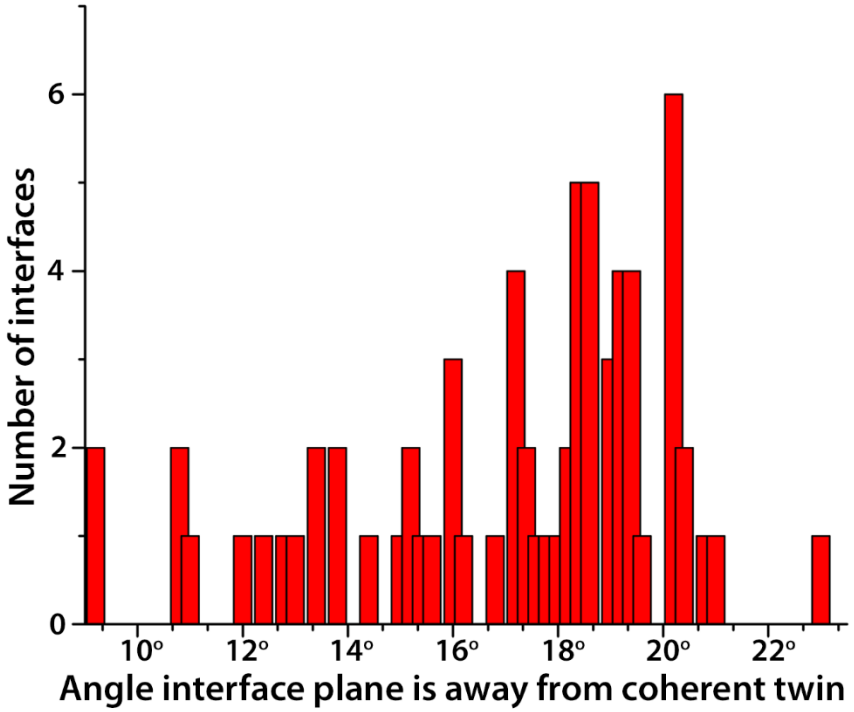

Figure 4.13: Distribution of angle away from a coherent twin habit plane for Ag with 0.2° increments.

Table 4.1 summarizes the initial microstructures of the three growth rates in terms of length-scale, morphology, and interface type. Increasing the growth rate decreases the bi-layer thickness and increases the proportion of incoherent twin interfaces.

Table 4.1: Bi-layer thickness and proportion of cube-on-cube and incoherent twin interfaces at the three growth rates.

Growth rate (mm/hr)	Bi-layer thickness (nm)	% cube-on-cube (globular platelet)	% incoherent twin (lamellar)
0.46	2200	100	0
7.3	1100	85	15
73	500	<34	>66

4.1.2 Mechanical testing

Mechanical testing of the directionally solidified material characterized in the previous section was conducted to determine the evolution of microstructure after deformation. Engineering stress-

strain curves from the split-Hopkinson pressure bar tests, 10^3 s^{-1} strain rate compression, were provided by Dr. Owen Kingstedt and select curves are presented in Fig. 4.14; more details of the mechanical response can be found in Kingstedt *et al.* [111, 113, 114]. One sample with a 500 nm bi-layer thickness and loaded along the growth direction was loaded 4 times to a total strain of 21.5%; the stress-strain curve for this case is not shown. The variation in the strain level for the different samples is attributed to the difficulty of precisely controlling strain with this loading method. Additionally, the actual strain, measured manually with a micrometer, of the samples will be higher than shown in the stress-strain curves because of multiple stress waves and are the values mentioned in the text. To summarize the response, the yield strength of the AgCu eutectic increases with decreasing feature size and increasing proportion of incoherent twin interfaces, and is dependent on the loading orientation relative to the growth direction. The contribution from increasing proportion of incoherent twin interfaces can be surmised from the more significant increase in yield strength between the 1100 nm and 500 nm bi-layer thickness material than between the 2200 nm and 1100 nm bi-layer thickness material when loading along the growth direction, 58% increase compared to a 27% increase. This is despite the difference in bi-layer thickness of both being approximately a factor of two. The 2200 nm and 1100 nm bi-layer thickness materials have 0% and 15% by area with incoherent twin interfaces while the 500 nm bi-layer thickness material has 66% or greater. From this it appears the increased portion of incoherent twin interfaces contributes to increasing the yield strength of the material. The yield strength impact from loading orientation with respect to the interfaces was more straightforward, at each bi-layer thickness the yield strengths from highest to lowest were loading parallel, perpendicular, and 45° to the growth direction.

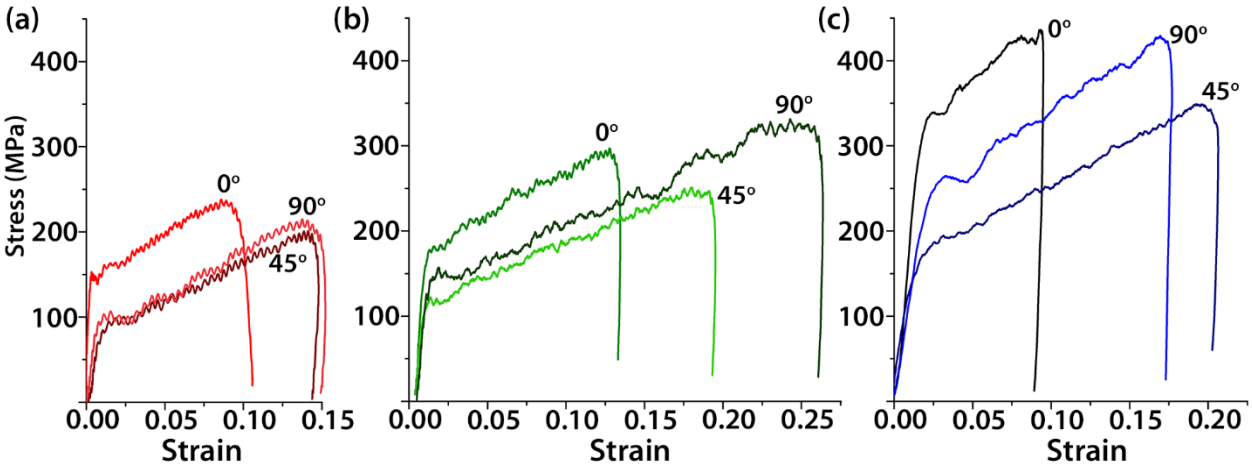

Figure 4.14: Engineering stress strain curves for different bi-layer thicknesses and loading directions. (a) 2200 nm (b) 1100 nm and (c) 500 nm bi-layer thickness.

Unexpectedly, and only in the samples with a 500 nm bi-layer thickness loaded along the growth direction, inelastic strain recovery of up to 3.5% was measured; the details of the mechanical behavior of those samples can be found in Kingstedt *et al.* [111]. Consequently, the reported microstructures of this loading condition are of the recovered deformed state. This response was repeatable and was not unique to a specific sample or a particular casting as two samples were tested from each of two castings. The amount of inelastic strain recovered with different amounts of strain for these different specimens is presented in Fig. 4.15. To identify the process associated with this recovery, molecular dynamics computer simulations were performed through a collaboration with Mr. Ao Li, a graduate student in the group of Professor Szlufarska at the University of Wisconsin-Madison. The results of that work will be used in the discussion of the mechanisms behind the formation of the recovered microstructure.

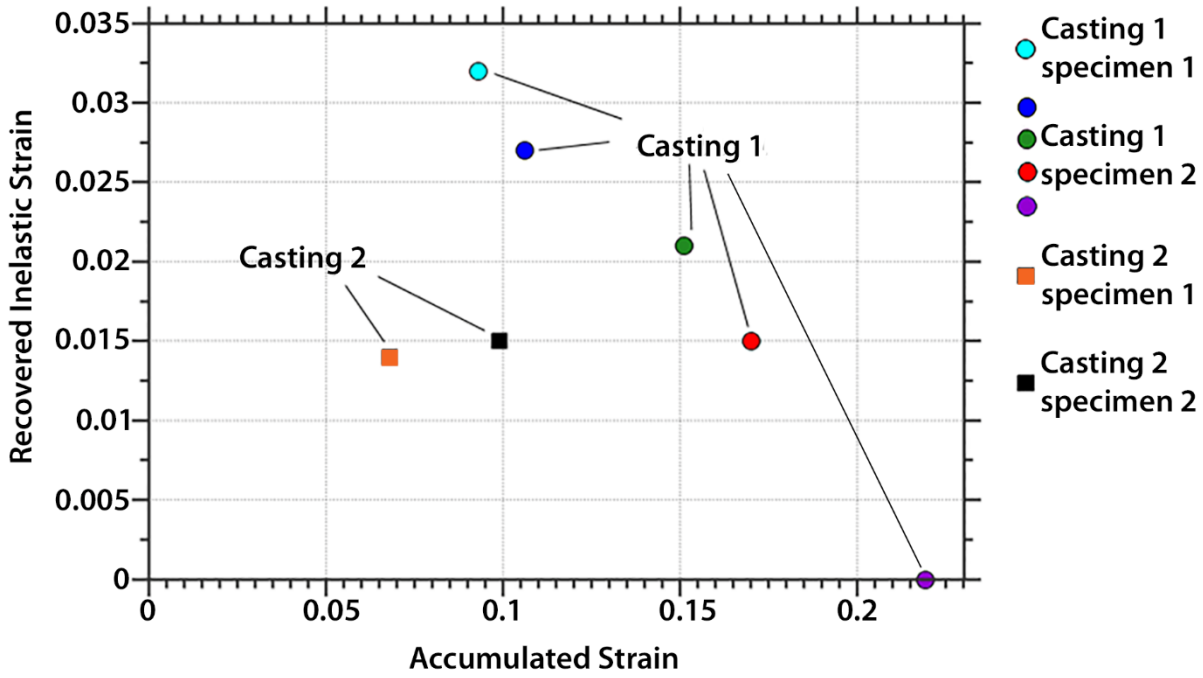

Figure 4.15: Recovered inelastic strain versus dynamic strain of samples with 500 nm bi-layer thickness loaded along the growth direction [111].

4.1.3 Deformation microstructures

Deformation microstructure of directionally solidified 2200 nm bi-layer thickness AgCu eutectic

For the directionally solidified AgCu eutectic with 2200 nm bi-layers, details of the initial microstructure can be found in Figs. 4.1-4.4, it is noted the orientation relationship between the Ag and Cu is exclusively cube-on-cube. Three orientations (0°,45°, and 90°) with respect to the growth direction were loaded in compression with SHPB. Loading along the [101] growth direction to a 10.5% compressive strain, produced a high density of dislocations that result in the formation of dislocation tangles in both phases. An example is presented in the bright-field electron micrograph shown in Fig. 4.16(a) and the corresponding selected area diffraction pattern in Fig. 4.16(b). The dislocation density in Ag increases near the Cu platelets with the Ag/Cu interfaces showing the highest density of dislocations. This suggests the interfaces act as either sources or barriers for dislocations and dislocations are more easily retained in Ag than in Cu. In

contrast, the dislocation content in the Cu-phase tends to be more localized, for instance the location marked by the arrowhead in Fig. 4.16(a).

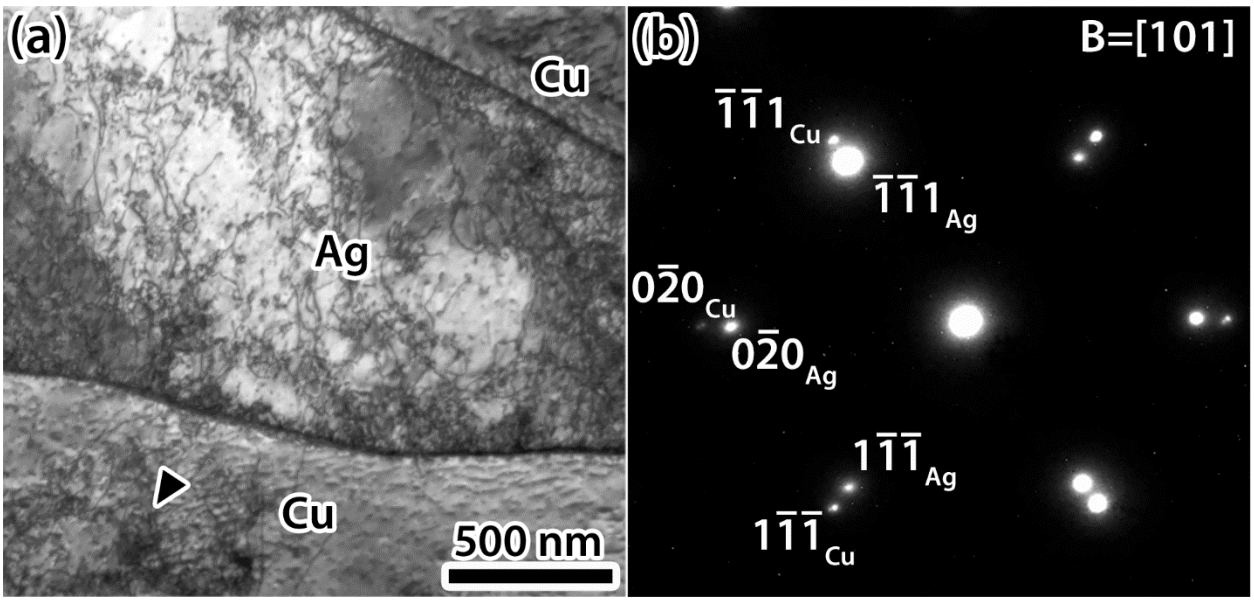

Figure 4.16: Bright-field electron micrograph of directionally solidified AgCu with 2200 nm bi-layer thickness compressed along the growth direction corresponding to a load orientation of 0° to the growth direction and to a strain of 10.5%. Selected area diffraction pattern for image shown in (b).

Loading 45° to the [101] growth direction, to a compressive strain of 14.7% and with a [001] local load orientation, resulted in dislocation slip and profuse deformation twinning in both Ag and Cu. An example of the twinned microstructure is presented in Figs. 4.17(a) and (b), and the corresponding selected area diffraction patterns with twin spots in Figs. 4.17(c) and (d). In the diffraction patterns, spots due to Cu and Ag are indicated, and matrix and twin spots are distinguished by subscripts m and t, respectively. Inspection of the deformation twins shows that the density of deformation twins is higher in the Ag-phase than in the Cu-phase. Some interactions of twins in Ag with the interfaces result in no evidence of strain being transmitted from the Ag-phase into the Cu; an example of this is indicated by arrows in Fig. 4.17(a). In other regions, the deformation twins in Ag terminate at the Ag/Cu interface, and dislocations are generated in the

Cu-phase, Fig. 4.17(b). The arrowheads mark deformation twins in Ag and the arrow marks dislocation emission in Cu in Fig. 4.17(b). The selected area diffraction patterns confirm deformation twinning in Ag and Cu in Fig. 4.17(a) and only in Ag in Fig. 4.17(b). Additionally, there is streaking of the Ag and Cu diffraction spots in Fig. 4.17(c) and streaking of the Ag diffraction spots in Fig. 4.17(d), indicating the presence of stacking faults in addition to the twins.

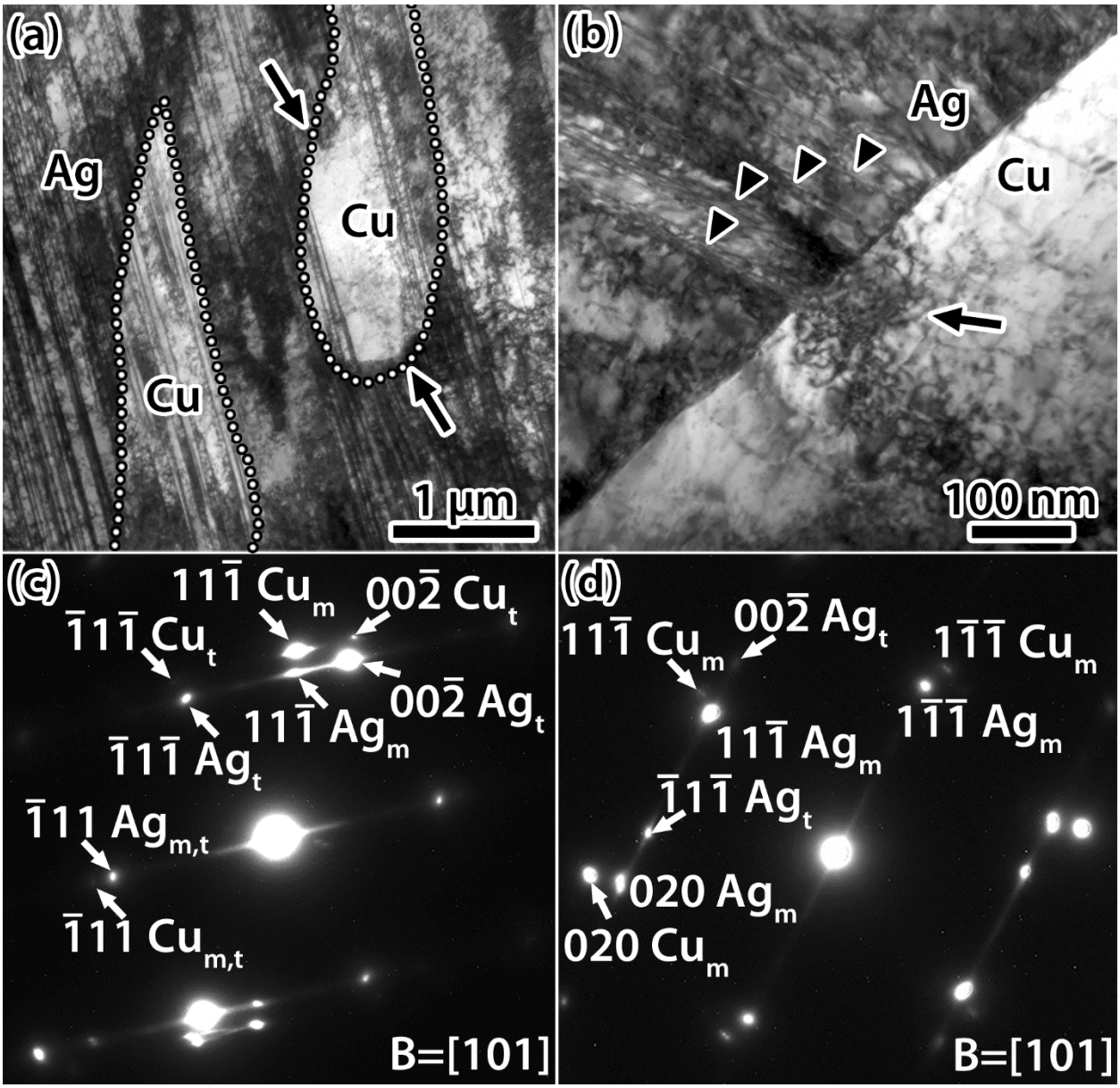

Figure 4.17: Bright-field electron micrographs of directionally solidified AgCu with 2200 nm bi-layer thickness compressed 45° to the growth direction to 14.7% strain corresponding to a load orientation of [001]. Selected area diffraction pattern for image (a) and (b) shown in (c) and (d), respectively. Ag/Cu interfaces marked in (a). Arrows in (a) mark regions of the interfaces with twinning on the Ag side and no twinning on the Cu side. Arrowheads mark deformation twins in Ag and the arrow marks dislocations in Cu in (b).

Loading at 90° to the growth direction of the 2200 nm bi-layer thickness material, to a compressive strain of 15.2%, resulted in deformation structures that were dependent on crystal orientation. This dependence and detailed deformation response is shown in the TEM micrographs

presented in Fig. 4.18. For a local load orientation of $[11\bar{1}]$, the deformation occurs by both dislocation slip and deformation twinning in Ag and Cu, Fig. 4.18(a). Locations of the deformation twinning in the Ag and Cu at the interface exhibits an abrupt orientation change due to rotation of the interface during the transfer of twinning defects across it as indicated by the arrowheads in Fig. 4.18(a). A higher magnification image of a region of the interface showing the rotations is presented in the inset of Fig. 4.18(a) and the rotation is measured to be around 34°. Fig. 4.18(b) contains both near $[11\bar{1}]$ and $[10\bar{1}]$ local load orientations in the right and left colonies, respectively. Consistent with Fig. 4.18(a), the near $[11\bar{1}]$ load orientation shows both deformation twinning and dislocation slip in both phases. While the near $[10\bar{1}]$ load orientation exhibits only dislocation slip in both phases. The selected area diffraction patterns in Fig. 4.18(c) and (d) confirm the presence of twins which are marked with a subscript t and streaking of the spots indicate the presence of stacking faults. In Fig. 4.18(d), however, twin spots are only present for the right colony. The diffraction pattern in Fig. 4.18(d) has only the Ag labeled for simplicity and spots from the left and right colonies, from Fig. 4.18(b), are labeled with subscripts L and R. Spots from L and R lie on the solid white lines and dotted white lines placed on the diffraction pattern, respectively. EBSD analysis, Fig. 4.19, confirmed the orientation dependence on deformation twinning on a larger scale. The inverse pole figures, of orientation maps Figs. 4.19(a) and (b), in Figs. 4.19(c) and (d) show deformation twins for the near $[11\bar{1}]$ load orientation but not for the near $[10\bar{1}]$ load orientation.

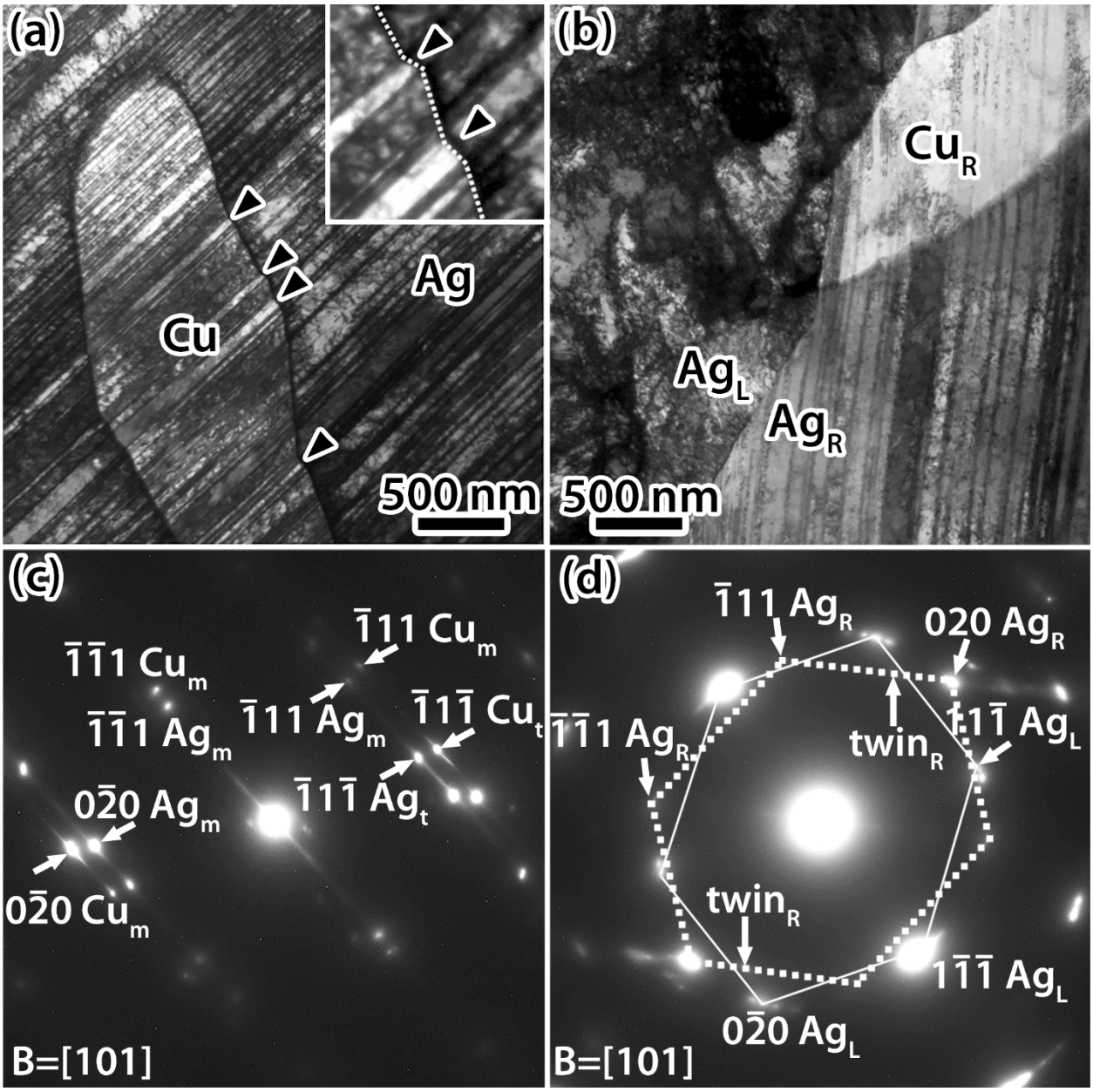

Figure 4.18: (a) and (b) Bright-field electron micrographs of directionally solidified AgCu with 2200 nm bi-layers loaded 90° to the growth direction to 15.2% strain. (c) and (d) are the corresponding selected area diffraction patterns for (a) and (b), respectively. Arrowheads in (a) mark select regions of the interface with abrupt changes indicating interfacial rotation. Subscripts m and t in the indexed diffraction spots in (c) corresponds to matrix and twin, respectively. Diffraction spots for Ag corresponding to the left and right grains of (b) are marked with L and R subscripts, respectively, in (d).

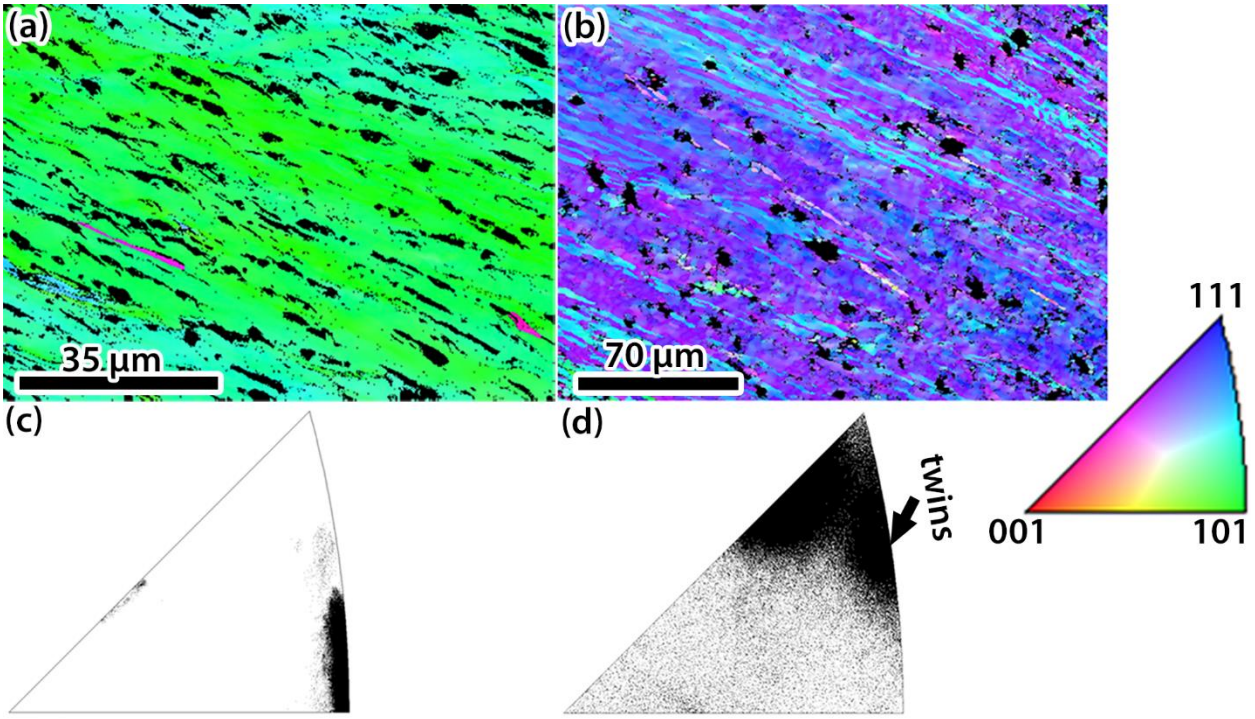

Figure 4.19: EBSD maps of a directionally solidified sample loaded 90° to the growth direction, 15.2% strain. (a) Grain loaded near the $[10\bar{1}]$ orientation. (b) Grain loaded near the $[11\bar{1}]$ orientation. (c) and (d) Inverse pole figure of (a) and (b), respectively. The twins are light blue in (b).

Deformation microstructure of 1100 nm bi-layer thickness directionally solidified AgCu eutectic

Deformed microstructures of the 1100 nm bi-layer thickness material with cube-on-cube and incoherent twin interfaces were characterized by TEM and examples of it are presented in Figs. 4.20 and 4.21, respectively. For comparison to the 2200 nm thick bi-layer material, the 1100 nm thick bi-layer material exhibited a slightly higher mechanical strength for each of the loading orientations. Additionally, at this bi-layer thickness there are regions with incoherent twin interfaces, which were not present in the 2200 nm bi-layer thickness material.

Deformation mechanisms observed in the intermediate length-scale, 1100 nm bi-layer thickness, in regions with the cube-on-cube orientation relationship, are load orientation dependent. Loading along the [101] growth direction to a strain of 13.5% resulted in dislocation

slip on several systems in both phases; see for example Fig. 4.20(a). Dislocation tangles, forming cells of varying sizes and cell wall thickness, were evident in both phases; arrowheads in Fig. 4.20(a) indicate select examples. The dislocation density is lower and less uniform in the Cu than in the Ag-phase. Changing the loading direction to either 45° or 90° to the growth direction, Figs. 4.20(b) and (c), caused the deformation response to be carried by both dislocation slip and deformation twinning, consistent with the 2200 nm thick bi-layer material. In the samples loaded at 45° to the growth direction to 25% strain, the deformation microstructure had dislocation cells in both phases and deformation twinning in only the Ag-phase; arrows in Fig. 4.20(b) mark examples of deformation twins in the Ag-phase. The white dotted lines in Fig. 4.20(b) indicate the approximate location of the Ag/Cu interfaces. In contrast, in the sample loaded at 90° to the growth direction to 32% strain, deformation twinning occurred in both phases and appeared to be continuous across the interface. That is, deformation twinning in Cu was associated with twinning in Ag. Examples are marked by arrows in Fig. 4.20(c). When twins cross an interface, a rotation of the interface occurs. The inset in Fig. 4.20(c), which is of the interface region marked by the arrowhead, highlights this rotation and shows it is around 30°. Rotations of the interface were less clear in other regions of the interface likely from dislocation slip.

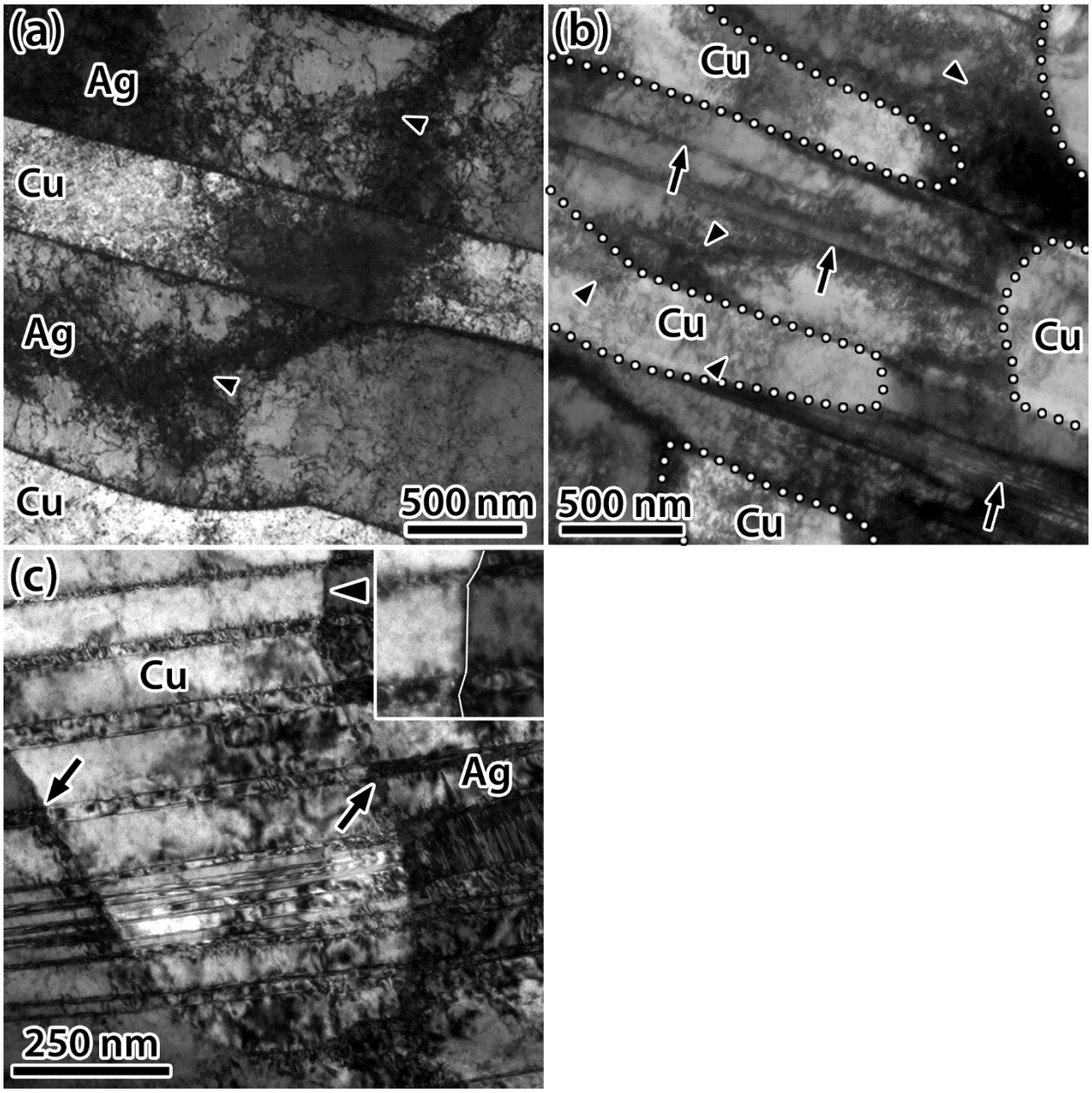

Figure 4.20: Bright-field electron micrograph of the deformed microstructure of 1100 nm bi-layer thickness material in regions of cube-on-cube orientation relationship between Ag and Cu after loading at (a) 0°, (b) 45° and (c) 90° to the growth direction to 11.1%, 25.0%, and 32.0% strains, respectively.

The two phases deform differently in regions exhibiting the twin orientation relationship between Ag and Cu. In the 1100 nm bi-layer thickness material loaded at 45° and 90° to the growth direction, deformation twinning was observed in the Ag-phase but it does not communicate across the incoherent twin interface into Cu, Fig. 4.21. The deformation twins in Ag were only

observed to form on the $(1\bar{1}\bar{1})_{\mathrm{Ag}}$ plane which is the twin plane shared between Ag and Cu, the Ag/Cu interfaces as a reminder are incoherent twin. Twins were observed occasionally in the Cu layer, but these were transmitted from an adjacent Ag layer that had a cube-on-cube interface with some fraction of the Cu layer. Dislocations were observed in both phases in the layer interiors in the form of dislocation tangles. Regions of incoherent twin interfaces of the 1100 nm bi-layer thickness material loaded along the growth direction were not found in the samples prepared, and are therefore not presented.

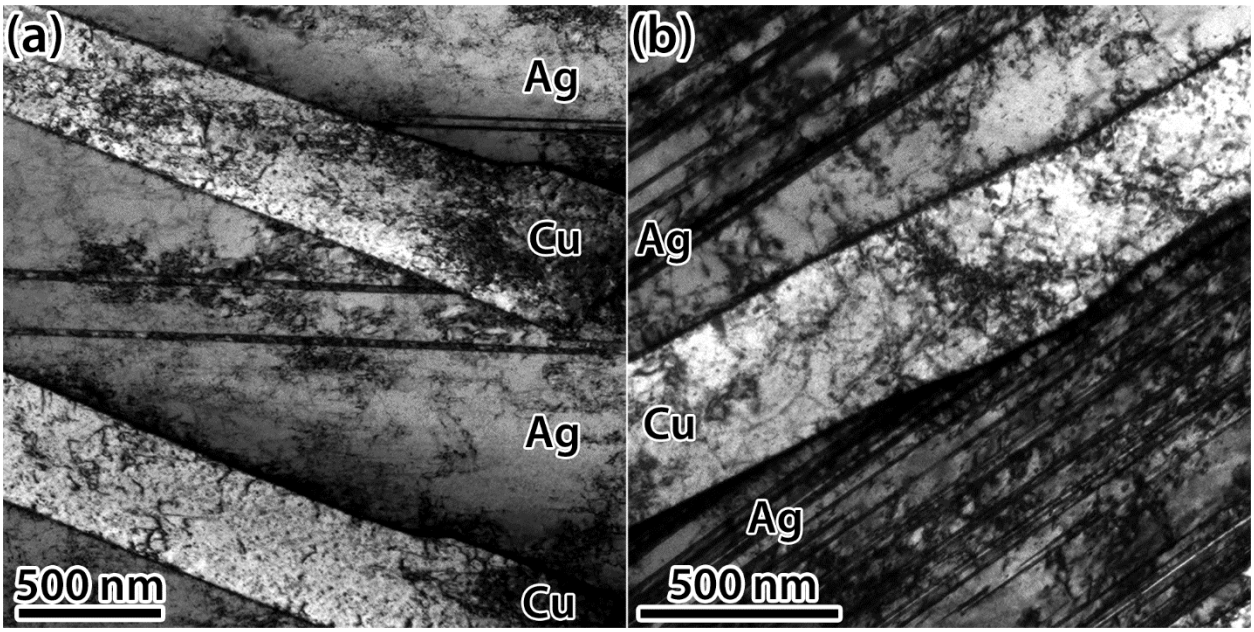

Figure 4.21: Bright-field electron micrographs of the deformed microstructure of the 1100 nm bi-layer thickness material in regions with incoherent twin interfaces between Ag and Cu after loading (a) 45° and (b) 90° to the growth direction to 20.4% and 32.0% strains, respectively.

Deformation microstructure of 500 nm bi-layer thickness directionally solidified AgCu eutectic

Deformed microstructures of the 500 nm bi-layer thickness material with cube-on-cube and incoherent twin interfaces were characterized by TEM and representative microstructures are present in Figs. 4.22-4.27. Mechanically, the 500 nm material had a higher mechanical strength for each of the load orientations than the 2200 nm and 1100 nm bi-layer material. Additionally,

this is the only length-scale where the incoherent twin interfaces accounted for the majority of the material, greater than 66%.

In regions of the material with a bi-layer thickness of 500 nm and cube-on-cube interfaces, the deformation was distinct from the 1100 nm and 2200 nm thick bi-layers. Dislocation slip was the dominant deformation mode in samples loaded at 0° and 45° to the growth direction and to strains of 5.5% and 19.0%, respectively. No deformation twins were found in material loaded at 0° but a low density of deformation twins existed in the Ag-phase in material loaded at 45° to the growth direction. Examples of these responses are shown in the bright-field micrographs presented in Figs. 4.22(a) and (b); the arrows mark regions of dislocations and the arrowhead in Fig. 4.22(b) shows twins.

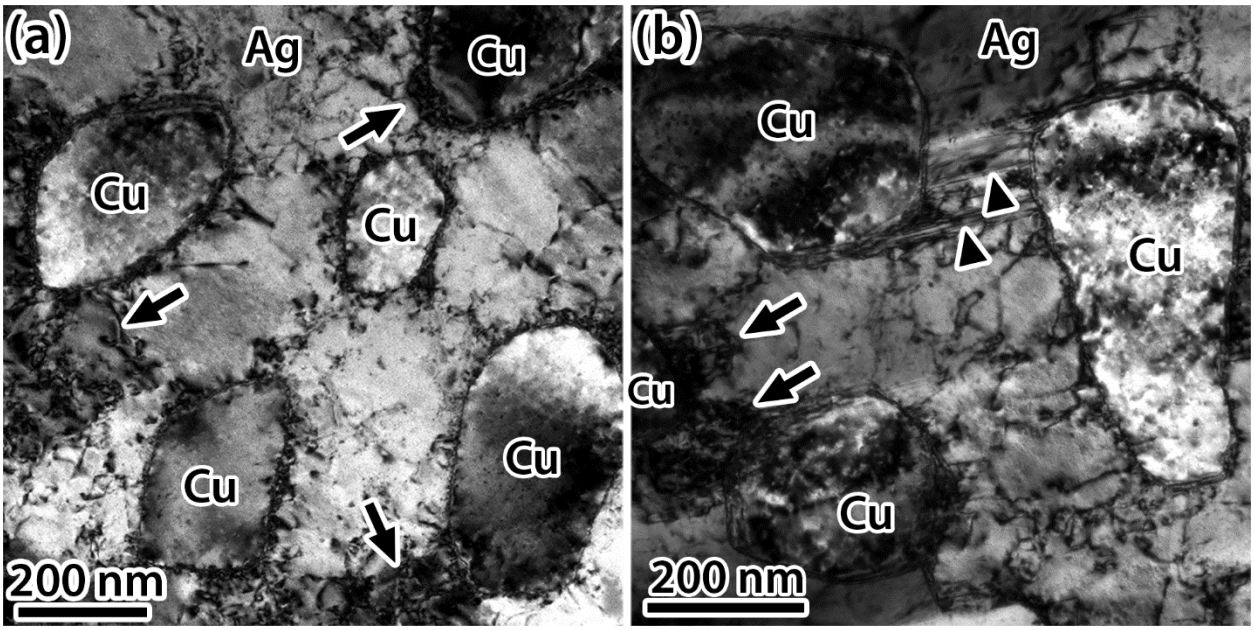

Figure 4.22: Bright-field electron micrograph of the deformed microstructure of 500 nm bi-layer thickness material in regions of cube-on-cube orientation relationship between Ag and Cu after loading (a) 0° and (b) 45° to the growth direction to 5.5% and 19.0% strains respectively. Arrows and arrowheads mark dislocation concentrations and twins respectively.

The deformation response in the material loaded at 90° was dependent on the colony, with some deforming exclusively by dislocation slip in both phases and others showing dislocation slip and deformation twinning in both phases. Examples of these deformation behaviors are shown in Fig. 4.23. The deformation twins in Cu appeared continuous with deformation twins in Ag but not all deformation twins in Ag resulted in twinning in the Cu-phase. The twins that cross the interface also rotate it by around 35° as seen in the inset shown in Fig. 4.23(a). The selected area electron diffraction pattern, Fig. 4.23(b), confirms the presence of deformation twins in both phases. The deformation was not uniform throughout the sample and appeared to be sensitive to even small changes in load orientation. For example, the bright-field electron micrograph presented in Fig. 4.23(c) exhibits a lower dislocation and deformation twin density than the region in Fig. 4.23(a) despite the regions being in close proximity and the load orientation difference being on the order of 5°. The region presented in Fig. 4.23(e) was also in close proximity to the other regions and the load orientation difference from Fig. 4.23(a) was on the order of 14°, in this region the material deformed exclusively by dislocation slip and the dislocation density was even lower.

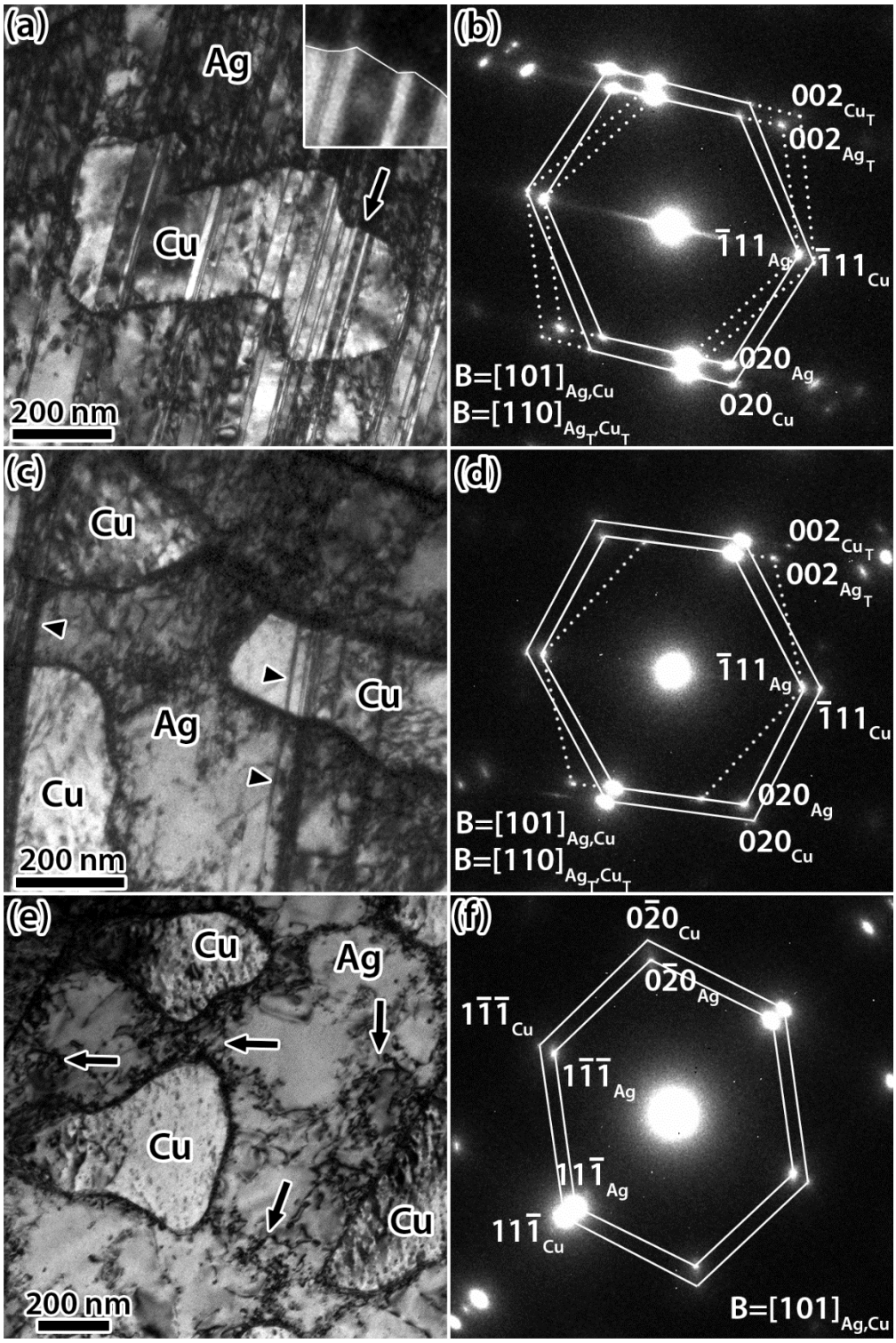

Figure 4.23: (a), (c), and (e) Bright-field electron micrographs of regions of cube-on-cube orientation relationship in the sample with 500 nm bi-layer thickness loaded 90° to the growth direction to 14.2% strain. (b), (d), and (f) Selected area diffraction patterns corresponding to (a), (c), and (e), respectively. Arrow marks the region shown in the inset in (a). Arrowheads mark select twins in (c). Arrows mark dislocation tangles in (e).

Regions of incoherent twin Ag/Cu interfaces in the smallest length scale, 500 nm bi-layers, deformed primarily by dislocation slip in both Ag and Cu at the three different load orientations. The dislocations in each load orientation have self-organized into a dislocation cell structure in Ag; the dislocations in Cu are more localized. Representative electron micrographs showing this deformation microstructure for the different loading orientations are presented in Fig. 4.24. Arrowheads mark regions of concentrated dislocations in Cu. A few regions in the samples loaded at 90° to the growth direction to a strain of 14.2% show twinning, however, in the Ag-phase only. An example is shown in Fig. 4.25; deformation twinning occurred only on the plane corresponding to the Ag/Cu twin plane and twins are marked by arrowheads. This region is on the border of a colony boundary with part of the colony boundary marked by an arrow. In contrast to the cube-on-cube interface regions, deformation twins were not observed in Cu.

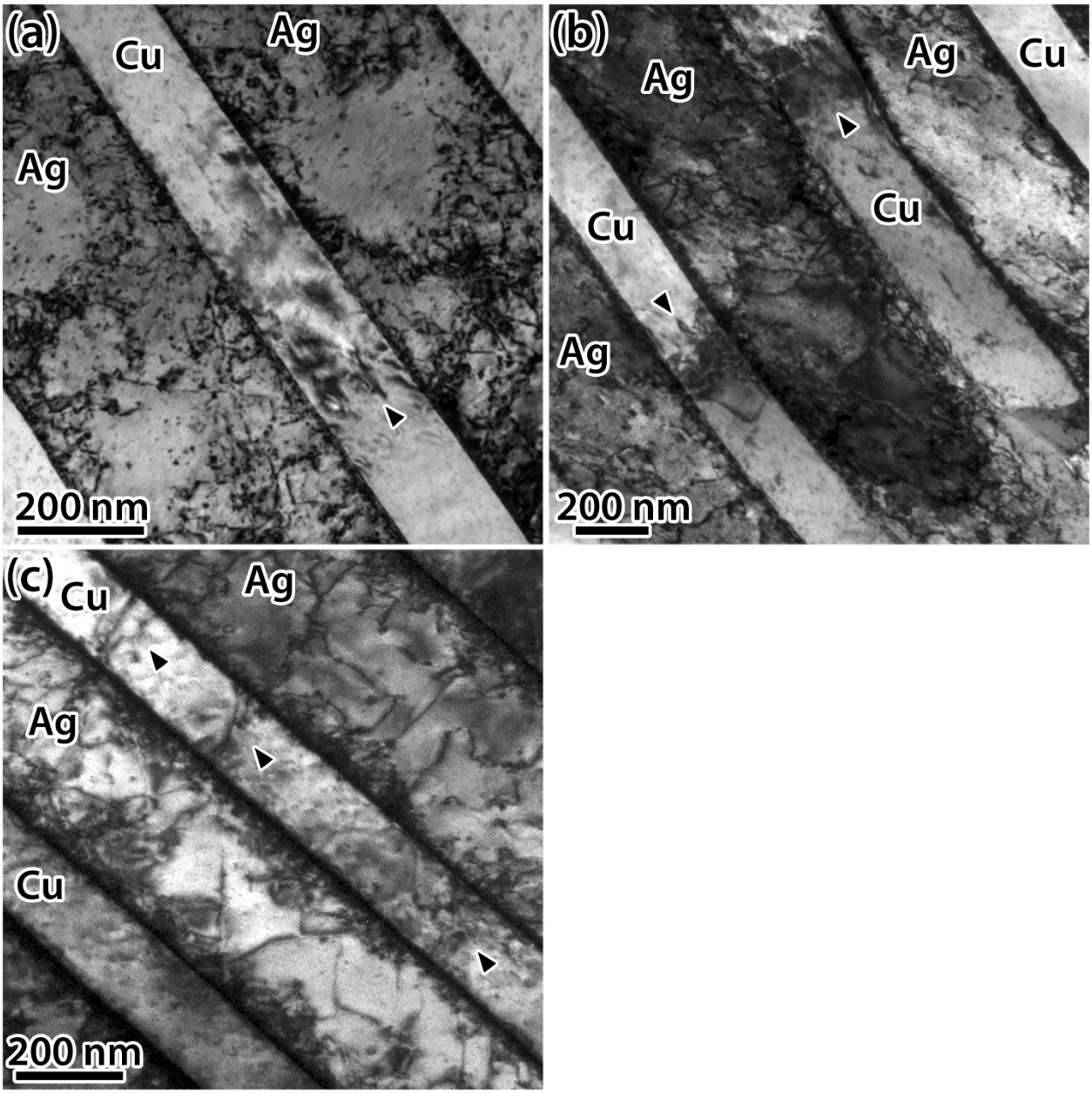

Figure 4.24: Bright-field electron micrographs of the deformed microstructure of 500 nm bi-layer thickness material in regions with incoherent twin interfaces between Ag and Cu after loading (a) 0°, (b) 45° and (c) 90° to the growth direction to 21.5%, 19.1%, and 14.2% strains, respectively. Arrowheads mark localized dislocation content in Cu.

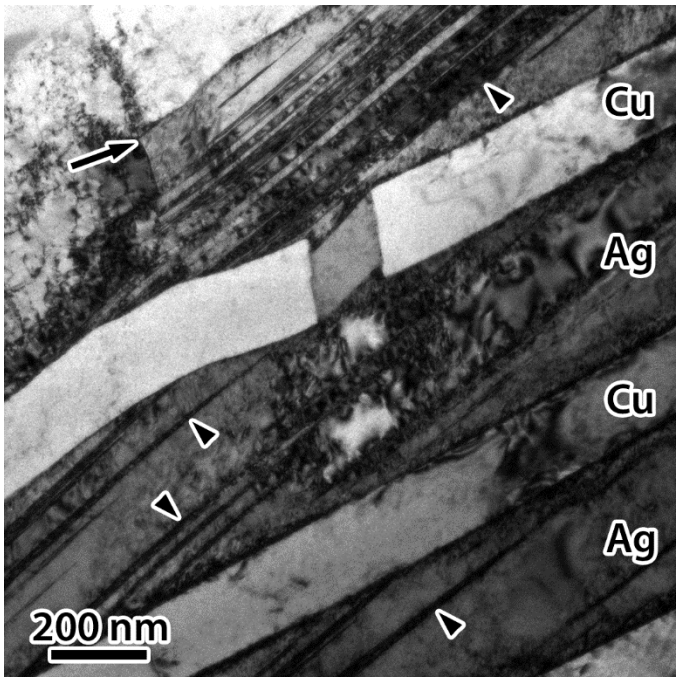

Figure 4.25: Bright-field electron micrograph of the deformation microstructure in a region of incoherent twin interfaces between Ag and Cu with 500 nm bi-layer thickness loaded 90° to the growth direction to 14.2%. A colony boundary is marked by the arrow. Twinning defects in the Ag-phase are marked by arrowheads. The discontinuity in the top Cu layer is a bridge of Ag-phase oriented cube-on-cube with respect to the Cu.

Samples with 500 nm bi-layer thickness loaded along the growth direction were distinct from the other samples because when loading dynamically with SHPB to strains at or lower than 17%, plastic strain recovery occurred. The following compares the deformation microstructures of incoherent twin interface regions of three samples with 500 nm bi-layer thickness and loaded along the growth direction: i) to 5.5% strain dynamically, ii) 21.5% dynamically, and iii) 4% quasi-statically. Only the sample loaded to 5.5% dynamically exhibited plastic strain recovery. In the sample strained dynamically 5.5% along the growth direction, dislocations are mostly at the interfaces, this can be seen in the bright-field TEM micrograph presented in Fig. 4.26(a). Whereas straining dynamically to 21.5%, dislocations were observed at the interfaces as well as layer

interiors. The dislocations in the Ag layer interiors form tangles and in many cases organize into dislocation cells, with cell walls marked by arrowheads in Fig. 4.26(b). The sample loaded 4% quasi-statically contained dislocations in the layer interiors as well, Fig. 4.26(c). In contrast to the sample loaded 21.5% dynamically, dislocations in the layer interiors for the sample loaded quasi-statically to 4% were in dislocation tangles but did not form into cell structures.

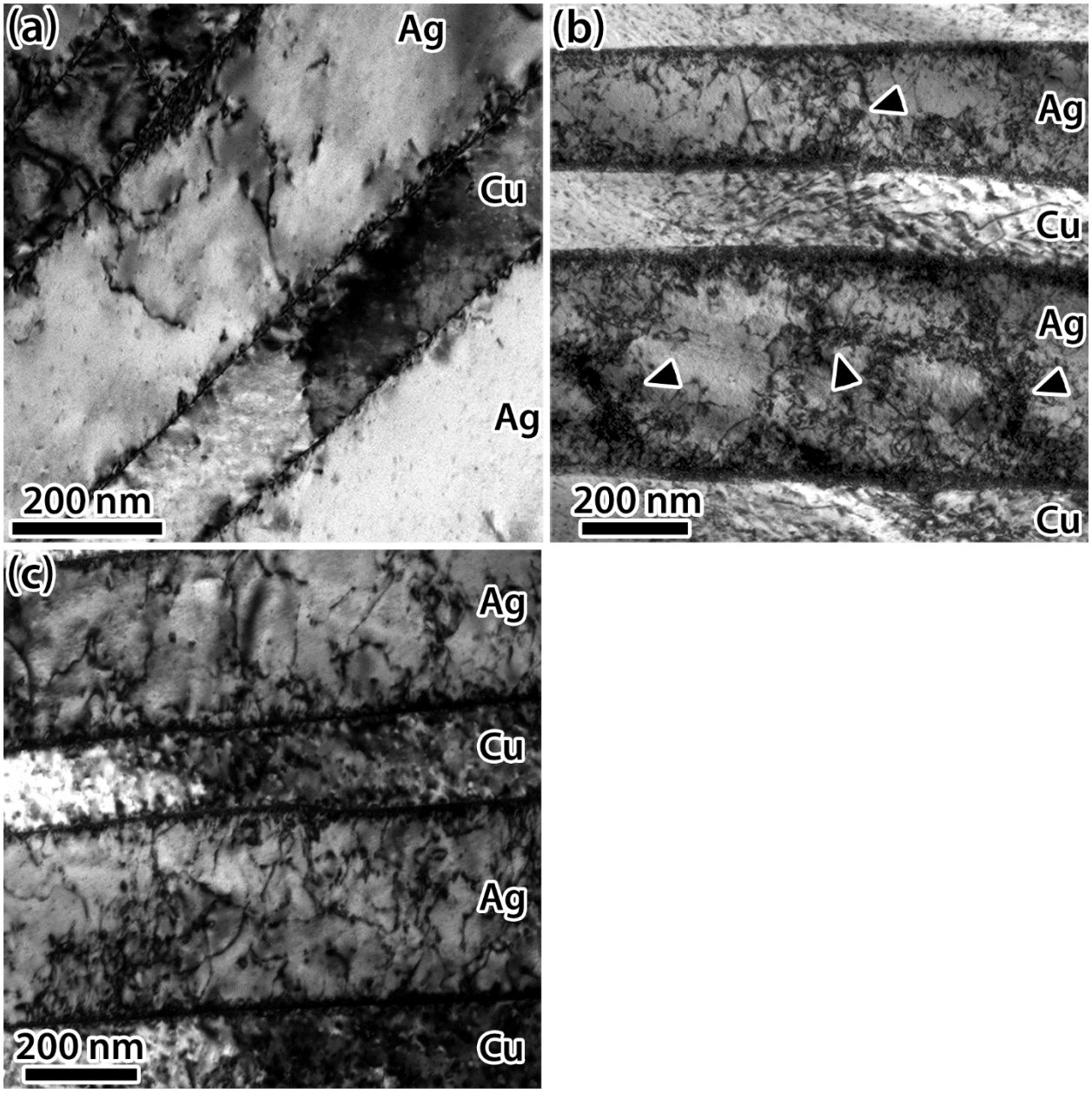

Figure 4.26: Bright-field electron micrographs of incoherent twin interface material loaded dynamically to strains of (a) 5.5%, and (b) 21.5% and quasi-statically to a strain of (c) 4%. Arrowheads in (b) mark dislocation cell walls.

For the same three samples, representative zone-axis TEM micrographs and corresponding selected area diffraction patterns are compared in Fig. 4.27. There is also a rotation away from the twin orientation relationship in all samples with 500 nm bi-layer thickness strained along the $[101]_{\mathrm{Ag}}||[110]_{\mathrm{Cu}}$. The change in orientation relationship did not occur for the cube-on-cube

orientation relationship regions, 1100 nm and 2200 nm bi-layer thickness material, or samples loaded 45° or 90° to the growth direction. This rotation is measured by the angle between the Ag/Cu twin plane diffraction spots, and can be visualized by the dotted lines in the selected area diffraction patterns in Figs. 4.27(d)-(f). The rotation away from the twin orientation relationship is summarized in Table 4.2. When loading along $[101]_{Ag}||[110]_{Cu}$, the rotation away from the twin orientation relationship increases with increasing strain.

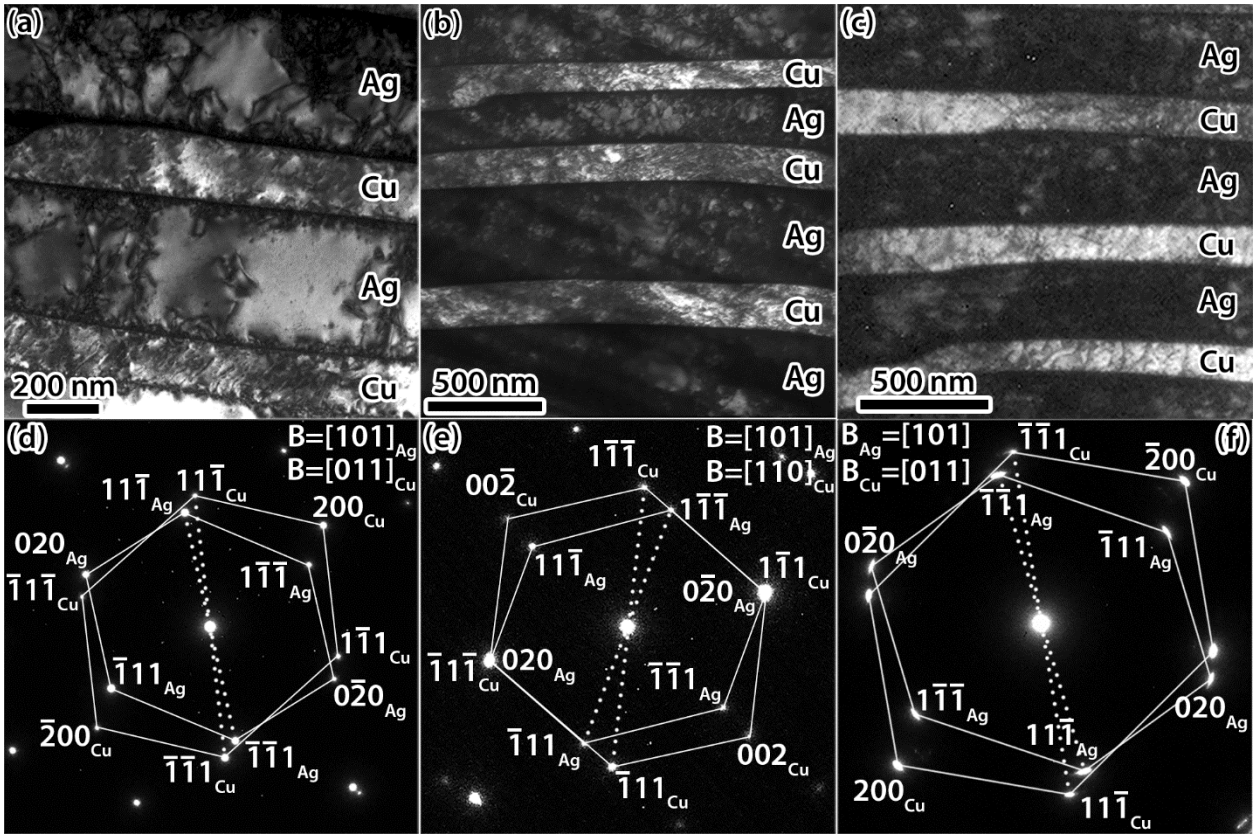

Figure 4.27: Electron micrographs of the 500 nm bi-layer thickness material loaded along the growth direction with SHPB to (a) 5.5% and (b) 21.5%, and quasi-statically to 4% strain (c). (d), (e), and (f) corresponding selected area diffraction patterns.

Table 4.2: Loading conditions and change in orientation relationship.

Test method, Strain (%), and load orientation with respect to the growth direction	Range of rotation away from the twin orientation relationship (average value)
Undeformed material	0.7° to 2.4° (1.7°)
SPHB, 9.5%, 0°	5.9° and 9.8° (7.6°)
SHPB, 23.5%, 0°	5.3° and 14.0° (10.3°)
SHPB, 15.4%, 90°	0.0° to 5.2° (1.8°)
Quasi-static, 4%, 0°	(6.3°)

4.2 Water quenched AgCu eutectic

4.2.1 Initial microstructure

The AgCu eutectic quenched in water exhibits a microstructure consisting of randomly oriented colonies of Ag and Cu lamellae. An example of this microstructure is shown in the backscattered electron SEM image presented in Fig. 4.28, which shows several colonies containing lamellae of Ag and Cu; here Cu is the darker phase. The size of the colonies varied and can be up to tens of microns wide. The thickness of the Ag and Cu bi-layers range from 120 to 200 nm with the Cu layer thickness approximately half that of Ag. The dislocation content in the interior of both layers is low. This undeformed microstructure is seen in the bright-field TEM image presented in Fig. 4.29(a). This image also shows that the Cu layers are discontinuous; examples are indicated by arrows in Fig. 4.29(a). The diffraction pattern shown as Fig. 4.29(b) shows the interfaces between the Cu and Ag is close to a coherent twin though the interfaces have curvature resulting in sections of incoherent twin interfaces. This is in contrast to the directionally solidified material in which the interfaces were incoherent twin. Some interfaces have a cube-on-cube orientation relationship between Ag and Cu as well. Additionally, the habit plane between the two phases is {111} for both the twin and cube-on-cube orientation relationships for both phases.

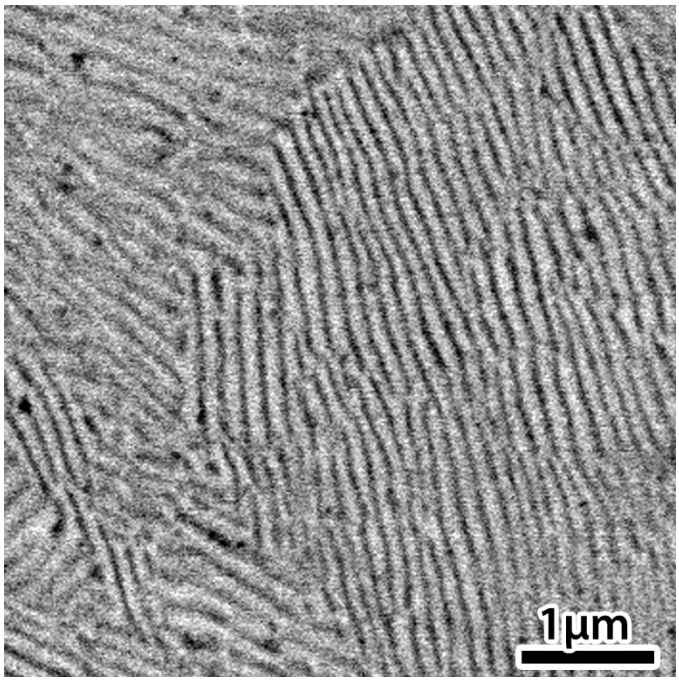

Figure 4.28: Backscattered electron micrograph of water quenched AgCu eutectic. Ag appears grey and Cu appears black.

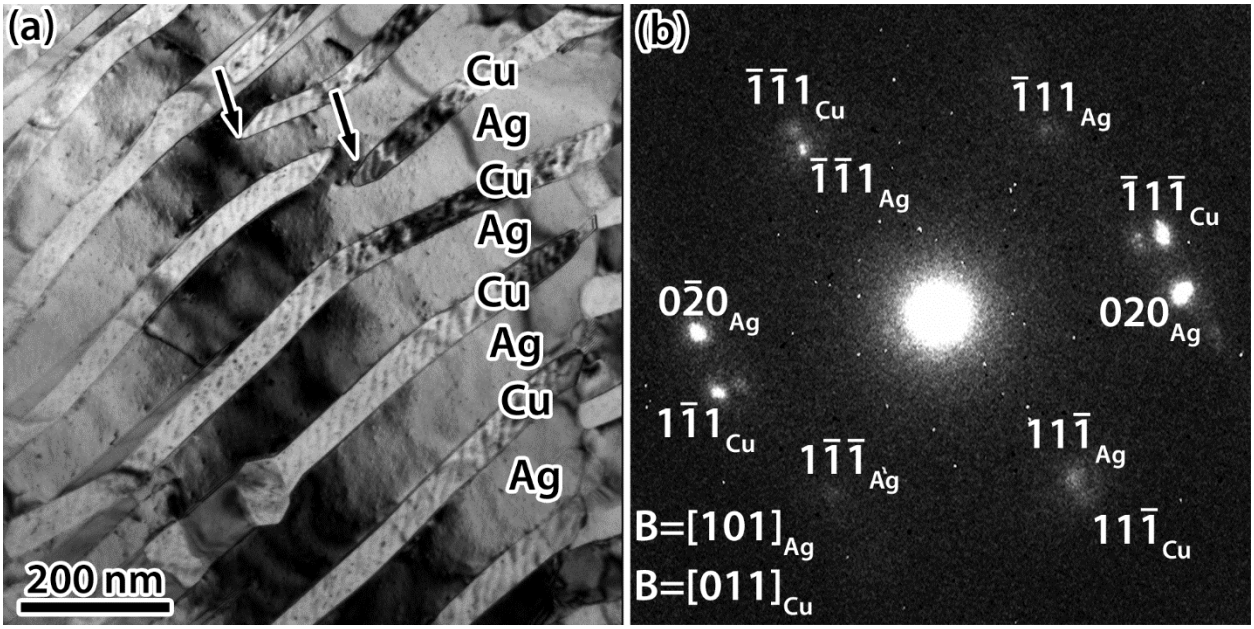

Figure 4.29: Undeformed AgCu cast by water quench with near coherent twin interfaces. (a) bright-field electron micrograph and (b) selected area diffraction pattern showing the diffraction spots of Ag and Cu. Arrows mark discontinuities in the Cu layers.

The structure of the interfaces was examined using high-resolution imaging conditions. Examples of an interface with a cube-on-cube and a coherent twin orientation relationship are shown in Figs. 4.30(a) and 4.30(b), respectively. These images show the interfaces are semi-coherent, due to the misfit dislocations, and that there is some periodic elastic strain. The orientation relationship can be assessed from the Fast Fourier Transform, FFT, of these high resolution images. The FFT results are shown as insets in each phase and confirm that for both cube-on-cube and twin orientation relationships, the interface planes are $\{111\}_{\mathrm{Ag}}||\{111\}_{\mathrm{Cu}}$. However, as observed in Fig. 4.29 the interfaces are not straight but exhibit some curvature especially close to termination points of the Cu-phase. The existence of this curvature implies local deviations from the twin habit plane but this is most likely accommodated by interface steps that preserve the original orientation relationship. The observation of both cube-on-cube and coherent twins suggests both have a similar energy [10]. This was confirmed by using molecular dynamics computer simulations to calculate the interfacial energy of the cube-on-cube and coherent twin orientation relationships with $\{111\}_{\mathrm{Ag}}||\{111\}_{\mathrm{Cu}}$ interfaces. The energy was 251 and 243 mJ/m^2 for the cube-on-cube and coherent twin relationship, respectively [120].

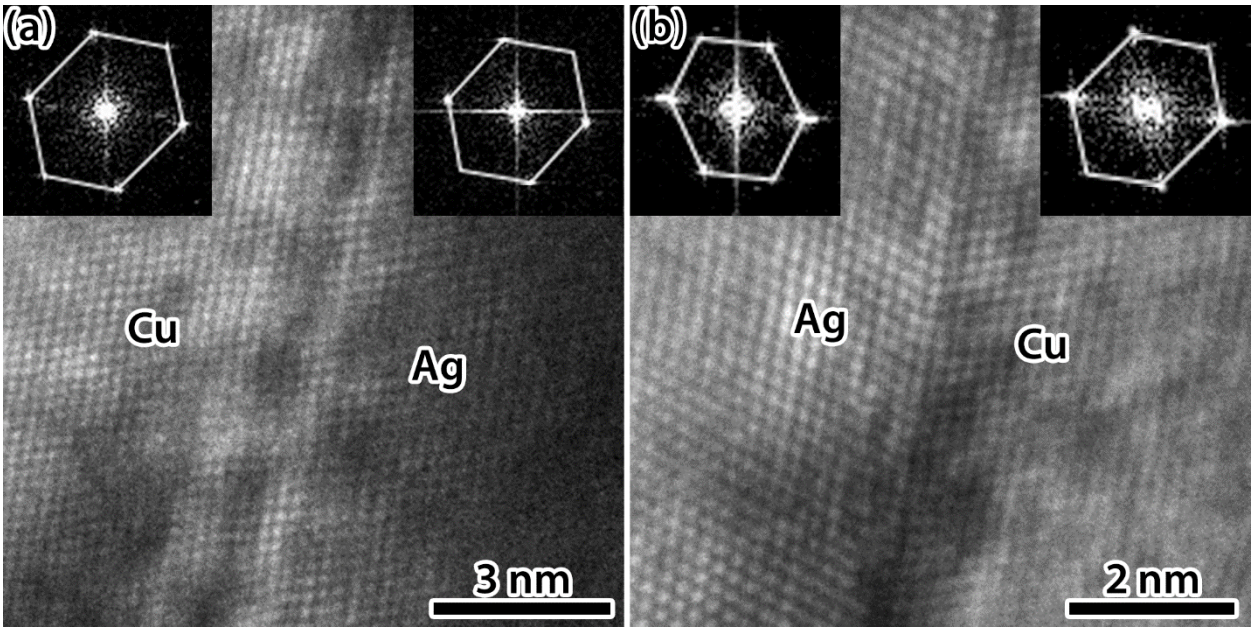

Figure 4.30: (a) HRTEM image of cube-on-cube interface in undeformed material. [011] beam direction. Fast Fourier transform (FFT) of both Cu and Ag included in the top left and right of image respectively. (b) HRTEM of AgCu coherent twin interface in undeformed material. FFT for both Ag and Cu included in top left and right, respectively.

4.2.2 Mechanical testing

High strain-rate compression tests were performed by Dr. Owen Kingstedt using a split Hopkinson pressure bar (SHPB) to investigate the high strain-rate response. In addition, conventional quasi-static compression tests were conducted to observe the strain-rate effect. Figure 4.31 shows the stress-strain curves for both quasi-statically and high strain rate loadings. The plots show little strain-rate dependence over six orders of magnitude. None of the samples failed during the compression experiments. Note the strength of the material is higher than any of the directionally solidified samples despite having a random orientation of colonies. More details on the macroscopic mechanical behavior can be found in Kingstedt *et al.* [113].

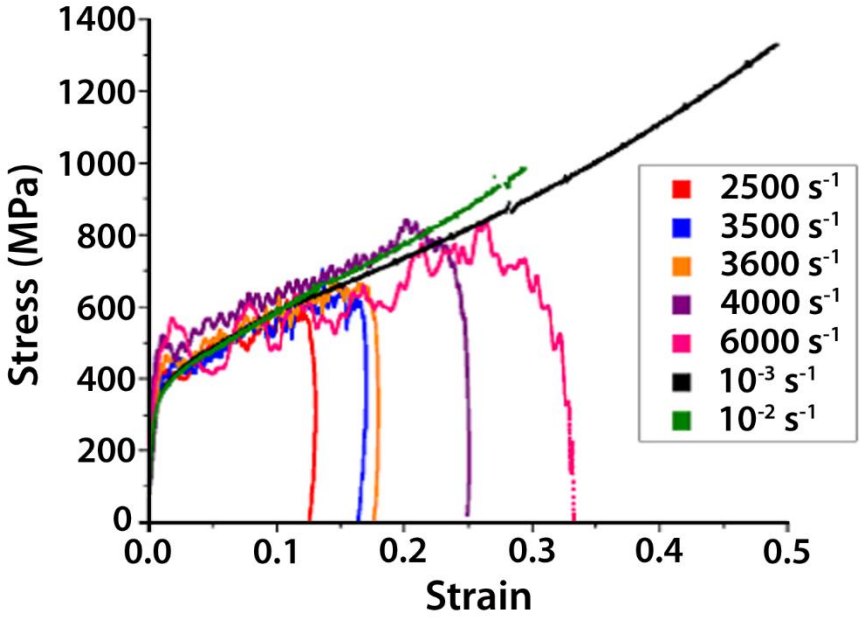

Figure 4.31: Stress strain results from SHPB and load frame compressive straining experiments on the water quenched AgCu.

4.2.3 Deformation microstructures

Both deformation twinning, parallel and inclined to the interfaces, and dislocation slip was observed in this material. Fig. 4.32(a) shows a bright-field electron micrograph of the deformed microstructure following high strain-rate compressive loading to 20% strain. Dislocations are observed in both Ag and Cu layers, although the density in Cu is low and non-uniformly distributed. Discontinuities in the Cu layers appear to be accumulation points for dislocations, suggesting that they serve either as nucleation sites for dislocations or as obstacles to them; examples of such sites are indicated by arrows in Fig. 4.32(a). Dislocations, at least in the Ag layer, extend across the layer although the density remains highest at the interface implying these serve as dislocation nucleation sites and barriers to dislocation slip. The diffraction pattern, Fig. 4.32(b), shows that both the Ag and Cu (111) spots are elongated and split indicating some rotation between layers of the same phase.

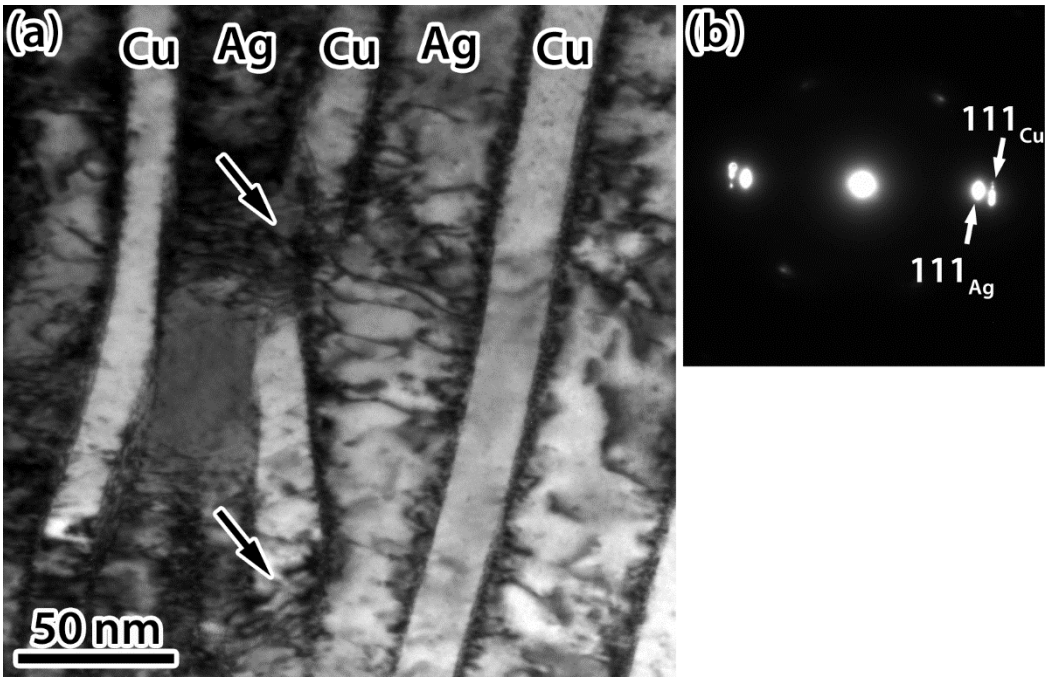

Figure 4.32: (a) Bright-field electron micrograph of water quenched material after 20% strain by split-Hopkinson pressure bar and (b) corresponding selected area diffraction pattern. Arrows mark discontinuities in the layered structure.

An example of deformation twinning parallel to the Ag/Cu interfaces is presented in Fig. 4.33(a) and is marked by arrows in both Ag and Cu-phases; a coherent twin interface between Ag and Cu is indicated by the dotted line on the left and a cube-on-cube interface on the right. Ag is twinned to the Cu orientation relationship at the right interface. The twin relationship between the Ag and Cu-phases can be seen in the diffraction pattern presented in Fig. 4.33(b); the twin diffraction spots are indicated by the subscript T. The twinning defects are generated from either colony boundaries or interfaces with deviations from the ideal {111}. Twinning in the Cu-phase was less common than in the Ag-phase.

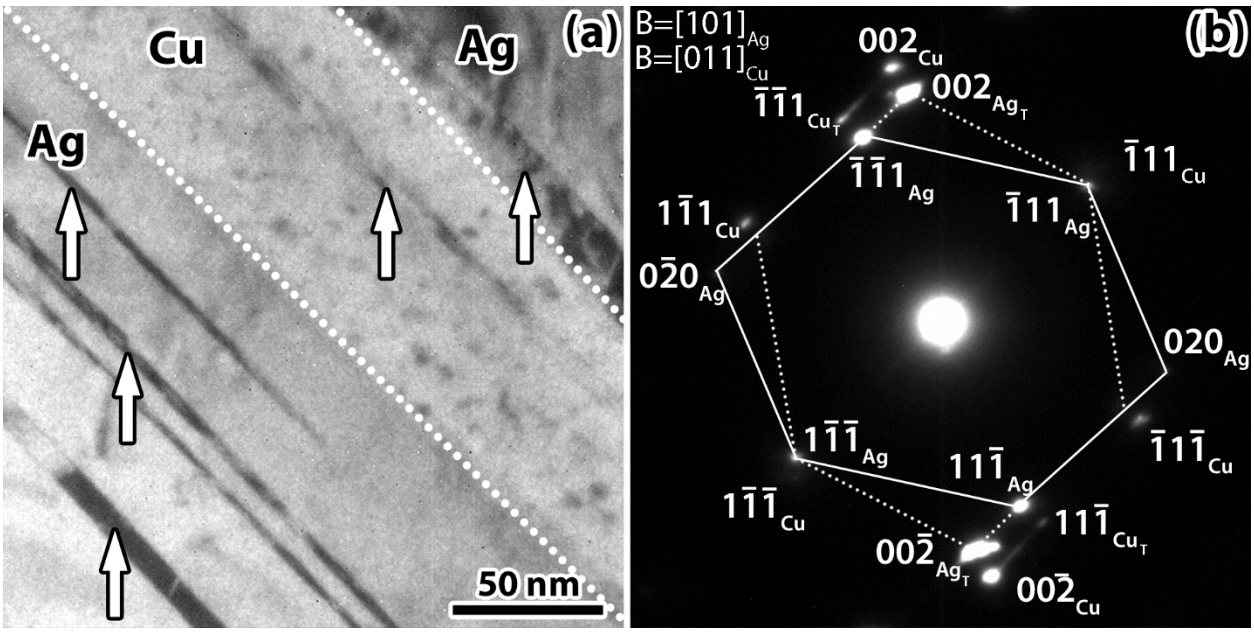

Figure 4.33: (a) Bright-field electron micrograph of water quenched material after 4% strain by split-Hopkinson pressure bar and (b) corresponding selected area diffraction pattern. Twin defects parallel to Ag/Cu interfaces in both Ag and Cu. Ag/Cu interfaces are marked with dotted lines.

Deformation twins inclined to the interface were also observed and are able to communicate across the cube-on-cube interfaces indicated by the continuity of twinning between Ag and Cu layers. An example of this effect is shown in the bright-field electron micrograph presented in Fig. 4.34(a). This shows a high density of deformation twins in Ag and Cu continuous across the cube-on-cube interface, though some are not continuous across the interface. Examination of the boxed region in Fig. 4.34(a) under high-resolution imaging conditions, Fig. 4.34(b), shows that in regions where the twins appear continuous across the interface, the interface as seen from the diffraction pattern, Fig. 4.34(c), has rotated from $(1\bar{1}\bar{1})_{\mathrm{M}}$ to $(200)_{\mathrm{T}}$ where subscript M is for matrix and subscript T is for twin. This rotation is consistent with dislocation theory for twinning partial dislocation transmission across a $(1\bar{1}\bar{1})_{\mathrm{M}}$ interface and indicates the twinning partial dislocations responsible for the interfacial rotation have a Burgers vector of either $\frac{a}{6}[2\bar{1}1]$ or $\frac{a}{6}[\bar{1}\bar{1}\bar{2}]$, see discussion section for details.

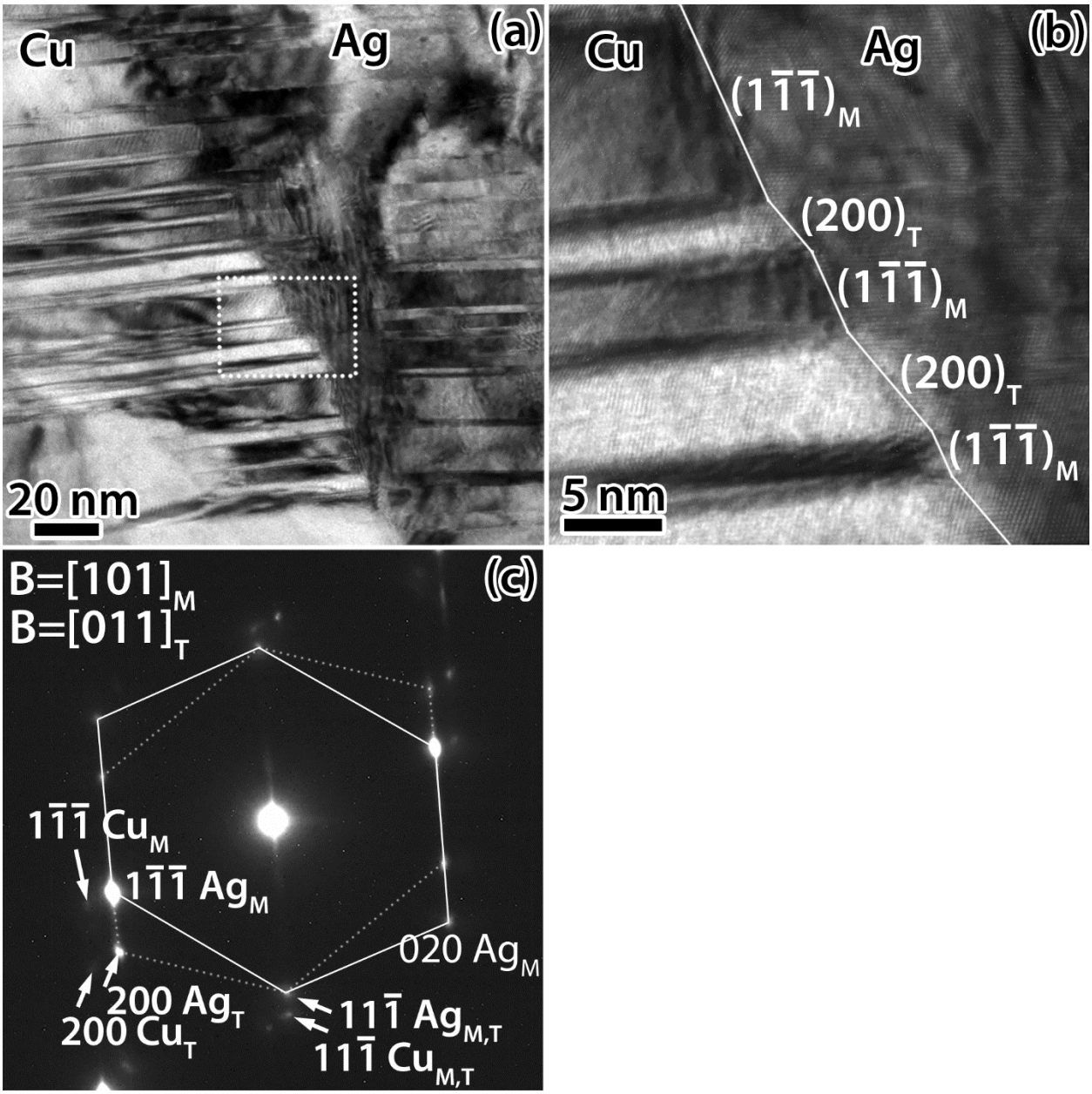

Figure 4.34: Bright-field TEM (a) and HRTEM (b) of water quenched material compressed to 4% strain by split-Hopkinson pressure bar. Twinning defects continuous across a cube-on-cube Ag/Cu interface. (c) Corresponding selected area diffraction pattern. (b) an inset of (a) and subscripts M and T correspond to matrix and twin.

4.3 *In situ* transmission electron microscope straining

The biggest limitation to using bulk *ex situ* straining experiments to study dislocation/interface interactions is the deformation processes are not directly observable. Therefore, it is necessary to interpret the observations of the final evolved microstructural state in terms of known deformation

processes and possible interactions between dislocations and the different types of interfaces. In contrast, *in situ* TEM straining experiments can be used for direct observation of dislocation/interface interactions. The possible impact of the proximity of the free surfaces does, however, need to be accounted for in the interpretation of the observations. Nevertheless, this technique has been used successfully to understand dislocation interactions with grain boundaries [86, 87, 92, 121]. Herein *in situ* TEM straining is used to understand the dependence of interface type on dislocation/interface interactions in AgCu eutectic. In the following, dislocation interactions with cube-on-cube, incoherent twin, and coherent twin type interfaces are investigated by using the *in situ* TEM straining method.

4.3.1 Cube-on-cube interfaces

Dislocation interactions with cube-on-cube interfaces observed during *in situ* TEM straining experiments showed that perfect dislocations require the assistance of a dislocation pile-up to communicate strain across the interfaces, i.e. dislocation absorption into the interface and emission into the neighboring phase, whereas twinning partial dislocations transmit unimpeded. The following observations are covered: single dislocation interactions, pile-ups, cross-slip before interfaces, and twin transmission across cube-on-cube interfaces.

Single perfect dislocations interacting with cube-on-cube interfaces are blocked at the Ag/Cu interface. In Fig. 4.35, for example, a single perfect dislocation in Ag is observed propagating towards a Ag/Cu interface. This dislocation appears as a short segment because it is viewed nearly edge on. The slip trace of this dislocation on the sample surface as it approaches the grain boundary can be seen in Fig. 4.35(b), indicated by an arrow. On encountering the grain boundary, it appears this dislocation is incorporated at least partially with the interface but primarily remains in Ag. Straining the sample more produces a separate two dislocation pile-up that is blocked by

the interface, arrowheads in Fig. 4.35(c). These dislocations also appear as short segments because they are viewed nearly edge on. The dislocations propagated too quickly to observe their approach when using 10 frames per second recording, however, following the slip traces to their origin indicates the dislocations were emitted from a Ag/Cu interface. The dislocations pile-up at the interface rather than absorb into the interface and transmit into Cu, likely from the dislocation content at the interface.

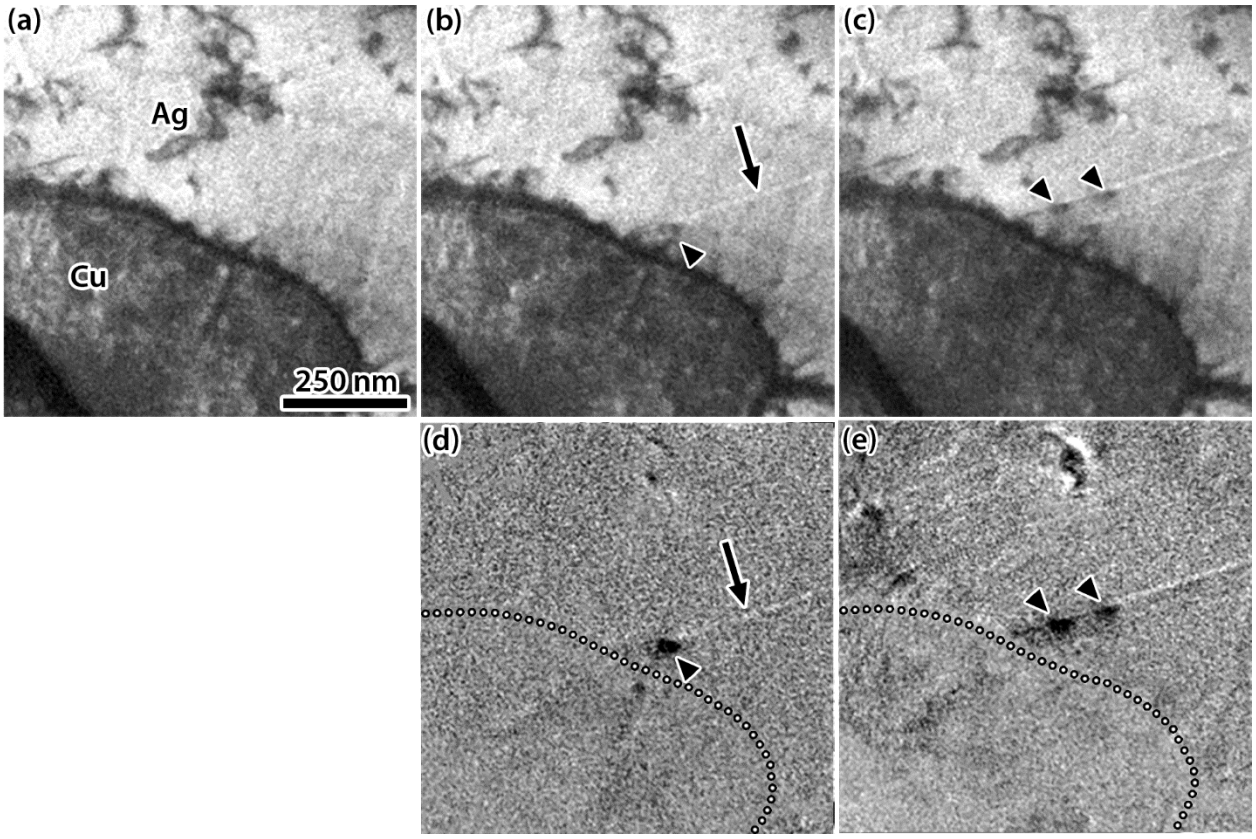

Figure 4.35: (a),(b) and (c) Time resolved images of AgCu eutectic with 1100 nm bi-layer thickness and cube-on-cube orientation relationship. (d) and (e) Difference images. Arrowheads mark dislocations. Arrows mark slip traces. The Ag/Cu interface in the difference images is marked with a dotted line.

Pile-ups of dislocations at the interfaces have been observed to form in both Cu and Ag-phases; examples of dislocation pile-ups forming in Cu and in Ag are shown in Figs. 4.36 and 4.37, respectively. A series of time-resolved images showing perfect dislocations in Cu, numbered in

Figs. 4.36(a)-(c), interacting with a cube-on-cube interface in the 2200 nm bi-layer thickness material is shown in Fig. 4.36. Several dislocations prior to recording the interaction, however, had communicated across the interface as indicated by dislocations in Ag, marked by arrowheads, and the interface had been sheared, both of which are evident in Fig. 4.36(a). Not all of the dislocations in Ag originate from the location of the pile-up. The displacement, shearing, of the interface due to prior dislocation slip transmission is indicated in Fig. 4.36(a) by the black lines, which indicate the approximate position of the interface. The slip traces in the Ag indicate slip remained on the same slip plane when it communicated across the interface. The formation of the dislocation pile-up reflects that the rate of arrival of dislocations is faster than the rate at which they can be accommodated in the interface. Transmission across the interface may be impacted by the accumulation of local damage in the form of residual dislocations left in the interface by previous transmission events.

To highlight the changes as strain progresses, difference images were formed by superimposing a negative image of the initial state on a positive image of the final state. The resultant difference images are presented in Figs. 4.36(d) and (e). In both of these images, the final state is compared to the initial state shown in Fig. 4.36(a); that is, Fig. 4.36(d) was formed by superimposing a negative of (a) on a positive of (b) and Fig. 4.36(e) by superimposing a negative of (a) on a positive of (c). To interpret these difference images, it is important to remember that a feature darker than the background represents a new position and a feature lighter than the background feature shows the initial position. Fig. 4.36(d), therefore, shows that between Figs. 4.36(a) and (b), increasing strain had moved dislocations closer to the interface with no plasticity evident in the adjoining Ag grain in the difference image, the shift in the bend contours indicates a small change in the elastic distortions. Between Figs. 4.36(b) and (c), one of the dislocations in

the pile-up absorbs into the interface and the change in strain contrast in Ag in the difference image Fig. 4.36(e), marked by the arrowhead, suggests dislocation emission into Ag.

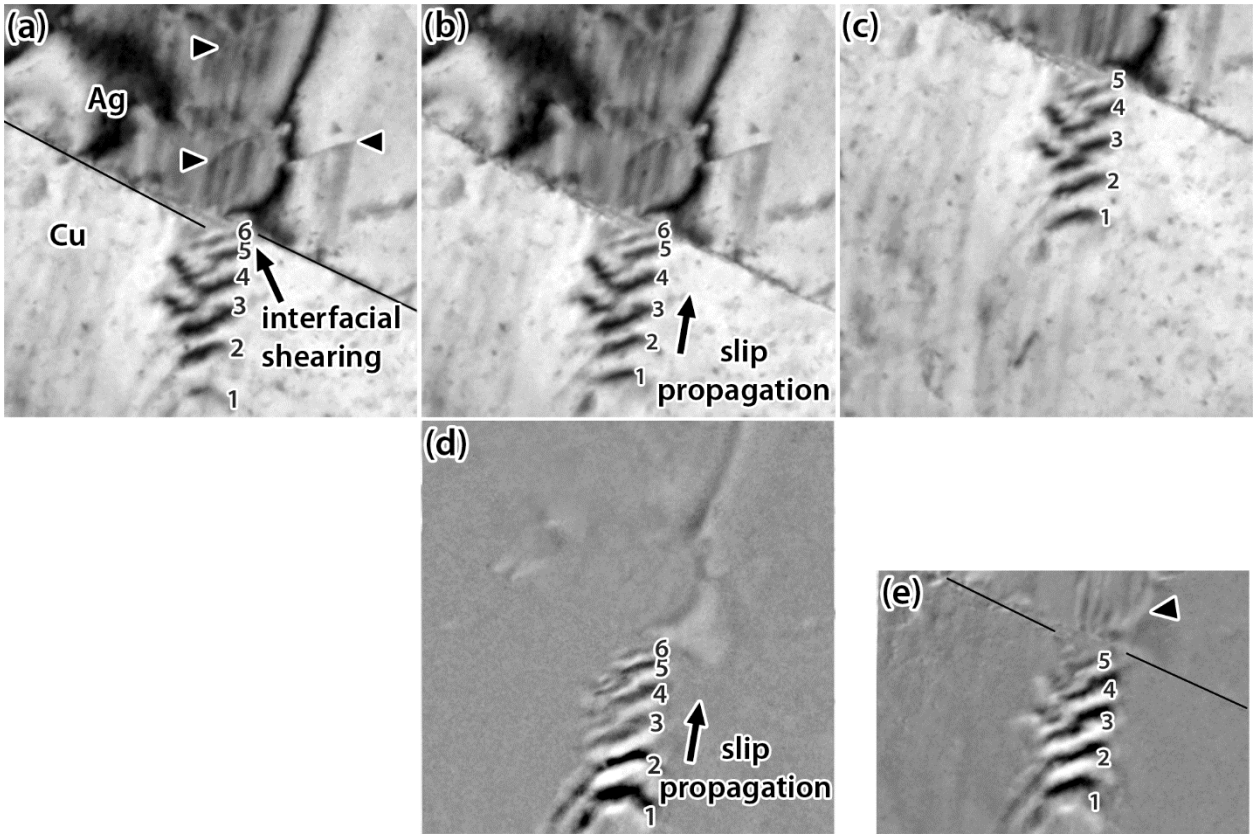

Figure 4.36: (a)-(c) Time resolved images of AgCu eutectic with 2200 nm bi-layer thickness and cube-on-cube orientation relationship. Difference images (d) and (e) correspond to subtracting (a) from (b) and (c), respectively. Interface in (a) marked with black lines. Arrowheads mark dislocations and elastic strain in (a) and (e) respectively.

Despite the continuity of slip systems across the cube-on-cube interfaces, cross-slip away from the pile-ups was common. An example of this is shown in the images presented in Fig. 4.37, in which dislocations in Ag can be seen to form a pile-up against the interface. Dislocation transmission into Cu occurred, but at a much slower rate than the rate at which dislocations joined the pile-up. In Fig. 4.37(a) a dislocation is marked with an arrowhead and a magnified view of the dislocation is shown in the inset. In Fig. 4.37(b) the dislocation had cross-slipped away. The conjugate plane has a plane normal perpendicular to the electron beam direction, and therefore

only the slip trace of the cross-slip dislocation is visible. The slip trace away from the pile-up is marked by arrows. The inset in Figs. 4.37(a) and (b) are of the same location and shows the dislocation is no longer there in (b); the arrowheads in Figs. 4.37(a) and (b) mark the position of the dislocation. The pile-up of dislocations and the cross-slip events indicate the Ag/Cu interface resists communication of dislocations into the Cu. It is unknown if the cross-slip of perfect dislocations would have occurred early in the deformation process when the interface contained less residual dislocation content and may have permitted transmission of dislocations across the interface more easily. The cross-slip of dislocations out of a dislocation pile-up is not unique to this study, such cross-slip events have been observed from dislocation pile-ups against grain boundaries in single-phase polycrystalline metals [86]. It was reasoned that this cross-slip behavior reflects the local stress condition and occurs when it is difficult to further decrease the dislocation-dislocation separation distance in the dislocation pile-up.

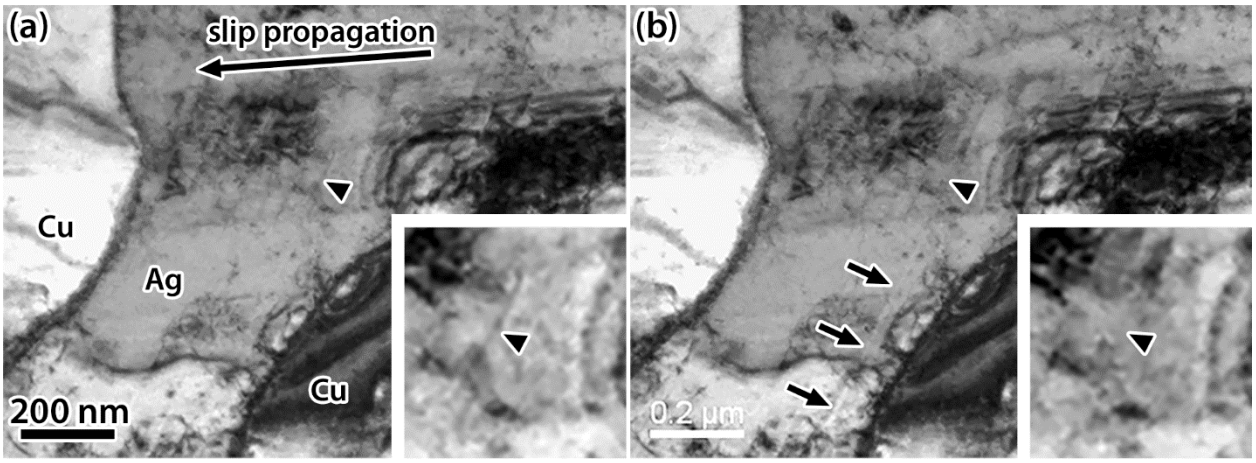

Figure 4.37: (a) and (b) Time resolved images of AgCu eutectic with 2200 nm bi-layer thickness and cube-on-cube orientation relationship. (c) Difference image corresponding to subtracting (a) from (b). Arrowheads mark location of a dislocation (a) and the same location in (b). Arrows mark a slip trace.

From the *in situ* TEM deformation experiments, twinning across the interfaces occurred more often than perfect dislocation slip across the interfaces. Fig. 4.38 contains two time-resolved

images of a continuous deformation twin across two Ag/Cu interfaces in the 1100 nm bi-layer material with the cube-on-cube orientation relationship between Ag and Cu. A deformation twin is seen, marked with arrows, to propagate through both the Ag and Cu-phases in Fig. 4.38(a). That is, the deformation twin has transferred across a Ag/Cu interface and across a Cu/Ag interface. With increasing strain, the deformation twin thickens to approximately 38 nm in both phases. A twin of that thickness would require 161 twinning partial dislocations in Ag, each on consecutive planes. The same number of twinning partial dislocations in Cu would result in a twin with a thickness of 34 nm, the difference in thickness could not be determined from the image. For the twin to transfer from Cu back into Ag, the thickness would return to 38 nm. Ultimately, the transfer of the twinning partial dislocations across the interface results in a rotation of the interface. Initially the interface is $(1\bar{1}\bar{1})_{\mathrm{M}}$ and after twin transmission it is $(\bar{1}1\bar{1})_{\mathrm{T}}$ indicating the twinning partial dislocations have a Burgers vector of $\frac{a}{6}[\bar{1}21]_{\mathrm{M}}$ and are glissile on the $(\bar{1}\bar{1}1)_{\mathrm{M}}$ plane; here M and T refer to the matrix and twin, respectively. The different planes are indicated in Fig. 4.38. The rotation of the interface was 39° which is consistent with rotations observed in SHPB deformed samples, see for example Figs. 4.18, 4.20, and 4.23. The rotation is larger than the 15.8° interface rotation observed in Fig. 4.34, also a SHPB sample, this is accounted for by the twinning partial dislocation Burgers vectors being different. The idea that twinning in the Cu-phase can be induced by Ag twinning partial dislocations is supported by this observation.

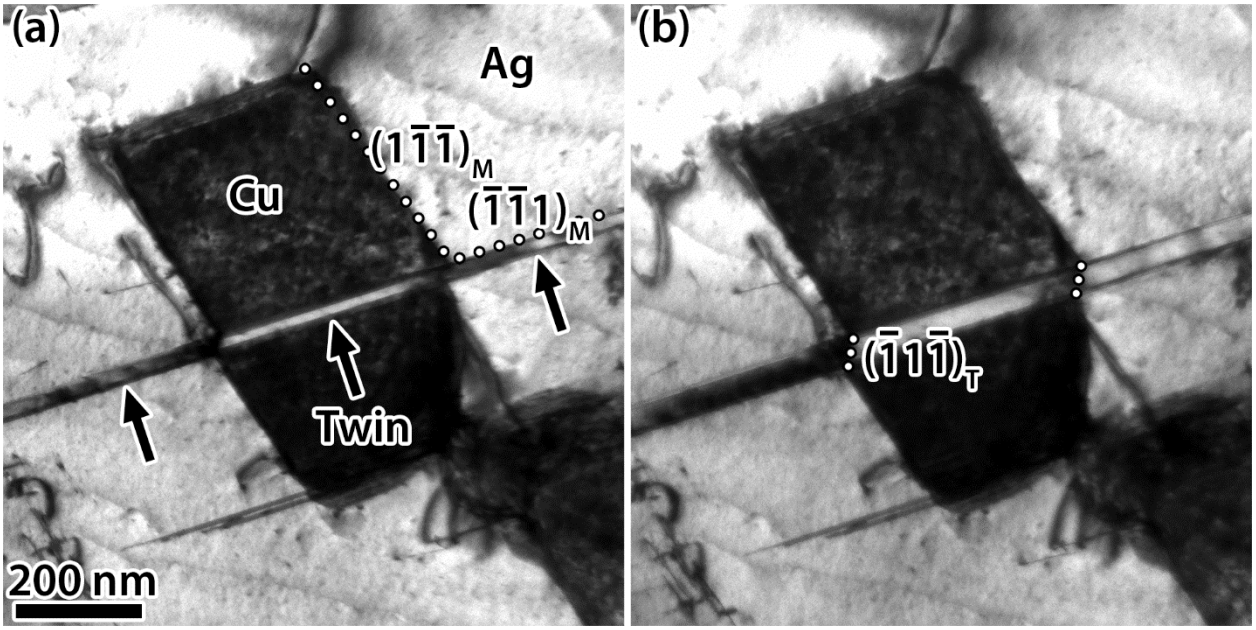

Figure 4.38: (a) and (b) Time resolved images showing the thickening of a deformation twin in both Ag and Cu that is continuous across two cube-on-cube interfaces with increasing strain. Arrows mark a deformation twin. White dotted lines mark interface planes, twin as well as Ag/Cu. Images from material with 1100 nm bi-layer thickness.

4.3.2 Incoherent twin interfaces

Dislocation interactions with the incoherent twin interfaces can be grouped into two categories: when the incoming slip system is i) on the shared plane, $(1\bar{1}\bar{1})_{\mathrm{Ag,Cu}}$, which is the twin plane between Ag and Cu and ii) on slip planes other than the shared plane. These result in a difference in relative interface barrier strengths to dislocation communication.

i) Slip on the shared plane

Incoherent twin interfaces have interface habit planes that are not the twin plane and therefore the twin plane is a slip plane shared between Ag and Cu continuous across the interface. Perfect dislocations on the shared plane have been observed to transfer across the interfaces and partial dislocations on the shared plane have been observed to be blocked. The observation of dislocations crossing the Ag/Cu interfaces is not without a cost, for each perfect dislocation to cross the interface a residual dislocation of magnitude $\mathrm{b_r} = \frac{a_{\mathrm{Ag}} - a_{\mathrm{Cu}}}{2}\langle 110\rangle$ is left at the interface. As

dislocation content builds at the interfaces, events such as back-emission into the layer, secondary-emission into the neighboring layer, and cross-slip have been observed to occur in Ag. Evidence for this is presented in the following figures.

During the *in situ* TEM straining experiments, formation of stacking-faults and twins on the $(1\bar{1}\bar{1})_{\mathrm{Ag,Cu}}$ shared plane was common in Ag but not in Cu. For example, in Fig. 4.39, which shows the final state of one of the deformation experiments, the Ag lamellae contain a high density of planar defects on the $(1\bar{1}\bar{1})_{\mathrm{Ag,Cu}}$, whereas in the Cu lamellae there are few instances of planar defects. From the selected area diffraction pattern, twin spots were not observed for Cu and the planar defects are believed to be stacking faults. Stacking faults in Cu are marked by the numbered arrows in Fig. 4.39 and the regions containing them are magnified in the insets at the right of the figure. Though the initial microstructure was not observed, the planar defects in Cu are believed to be from the *in situ* TEM deformation. Stacking faults in the Cu lamellae are not prevalent in the initial state of the material and one of the stacking faults in inset 3 was observed to propagate across the layer, marked by the arrowheads in Fig. 4.40. Examination of regions 1, 2, and 3 in Fig. 4.39 show thick twinned regions in the Ag associated with the stacking faults in the Cu. The origin of the stacking faults in Cu may be from stacking faults inside the Ag twinned regions transmitting directly into Cu. The twinned regions of Ag have a cube-on-cube orientation relationship with respect to the Cu layers which would allow transmission. One of the features of the cube-on-cube interfaces was the continuity of planar defects across the interface. It is not clear if there are corresponding stacking faults in the Ag twins because the twins are not viewed edge on. What Fig. 4.39 highlights is leading partial dislocations that created the stacking faults in Ag on the shared plane are prevalent and do not transmit across the interfaces into Cu as a leading partial dislocation on the shared plane. Planar defect nucleation in Cu is not a characteristic of the

deformation response. The deformed microstructure is consistent with the *ex situ* SHPB straining experiments for bulk specimens.

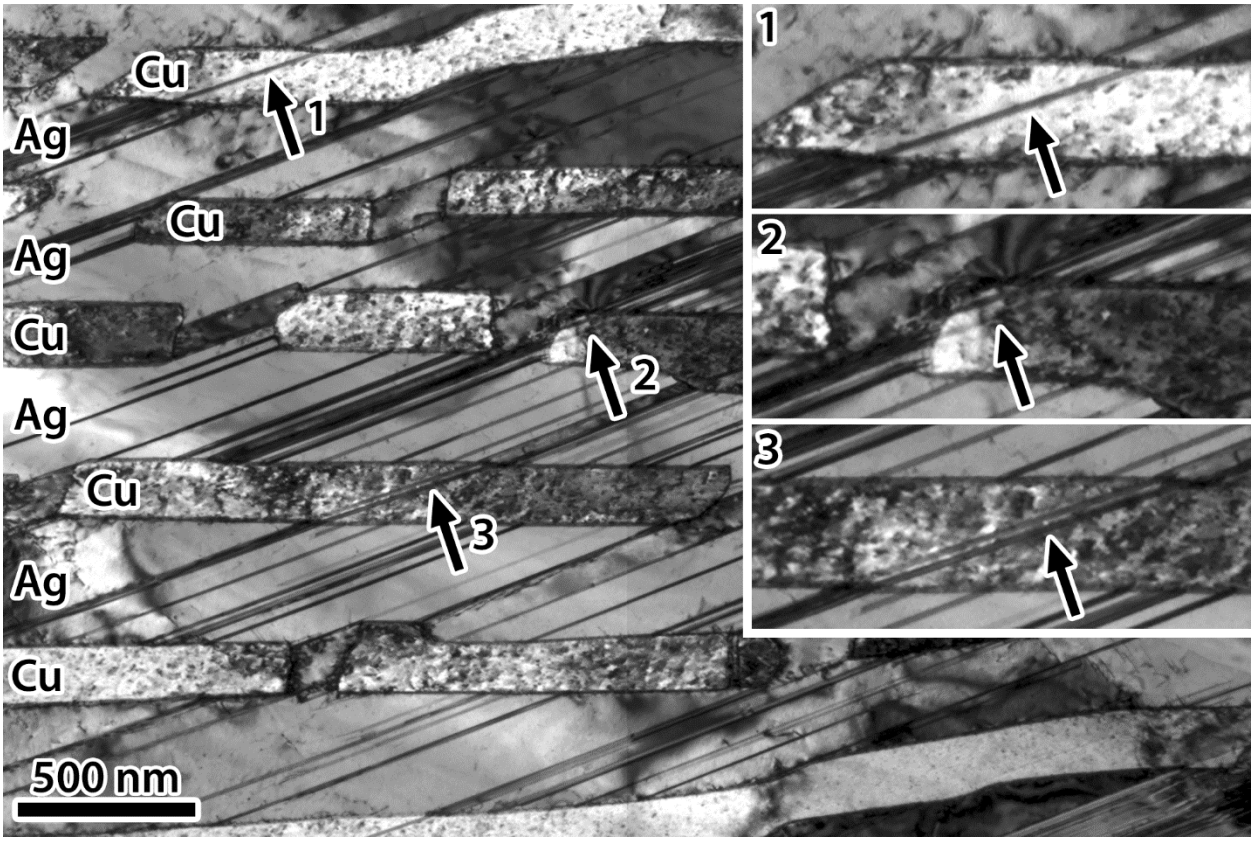

Figure 4.39: Bright-field electron micrograph of AgCu eutectic with 500 nm bi-layer thickness viewed near the $[101]_{Ag}||[011]_{Cu}$ beam direction. Arrows mark planar defects in Cu lamellae and insets corresponding to each are on the right side of the figure.

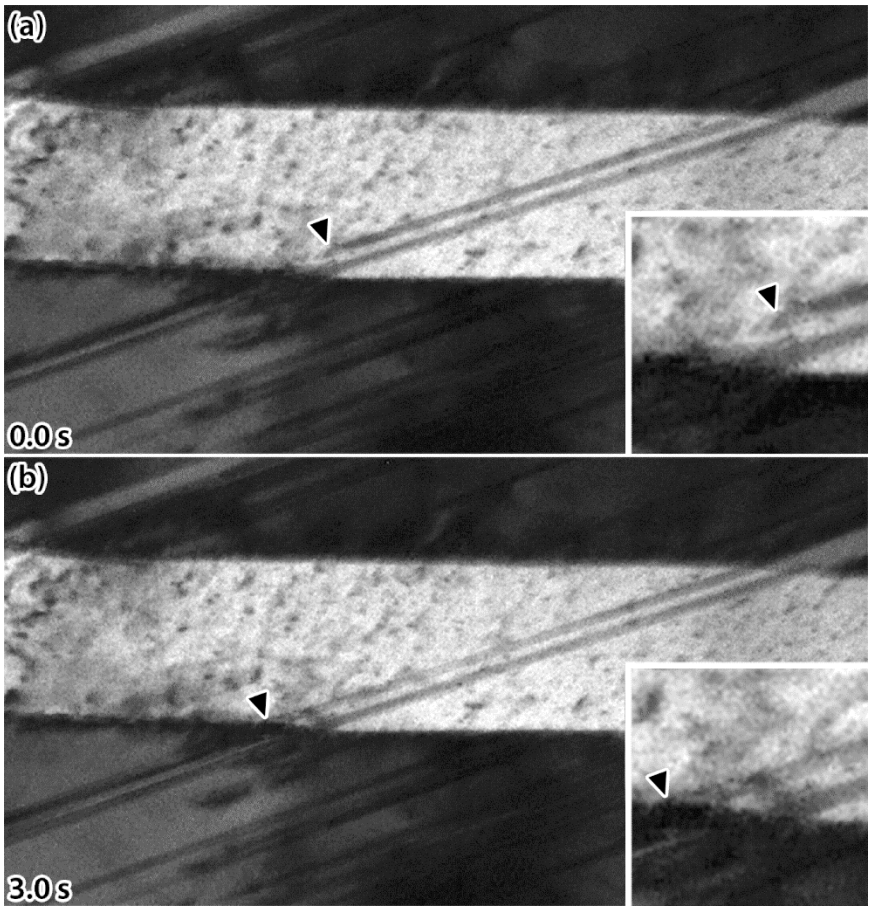

Figure 4.40: Time resolved images of AgCu eutectic with incoherent twin interfaces. Arrowheads mark a leading partial dislocation in Cu on the shared slip plane between Ag and Cu.

Partial dislocations are inhibited from communicating directly across incoherent twin interfaces on the shared plane as was shown in Fig. 4.39. Additional support for this statement comes from constriction of partial dislocations in Ag to a perfect dislocation before transferring across an interface to a perfect dislocation in Cu. An example of this is presented in Fig. 4.41. The stacking fault in Ag marked by the arrowheads in Figs. 4.41(a) and (c) was created by a leading partial dislocation. Straining the sample caused the stacking fault in Ag to clear and perfect dislocation slip in Cu. Both events are observed in the difference image Fig. 4.41(c) which was created by overlaying the inverse of (a) onto (b). Perfect dislocation slip in Cu was seen by the

displacement of sample preparation ion damage, marked by the arrow in Fig. 4.41(c). The stacking fault in Ag and perfect dislocation in Cu were on the same plane which can be seen by where the stacking fault in Ag had been and the perfect dislocation in Cu had slipped in the difference image. The events occurred too quickly to observe individually. However, the events are likely explained by first a trailing partial dislocation clearing the stacking fault in Ag and combining with the leading partial dislocation, that had created the stacking fault, to form a perfect dislocation in the Ag/Cu interface, i.e. constriction. The perfect dislocation in the interface then emits into the Cu layer on the same plane. What has been highlighted is dislocation slip can directly cross incoherent twin interfaces on the shared plane for perfect dislocations.

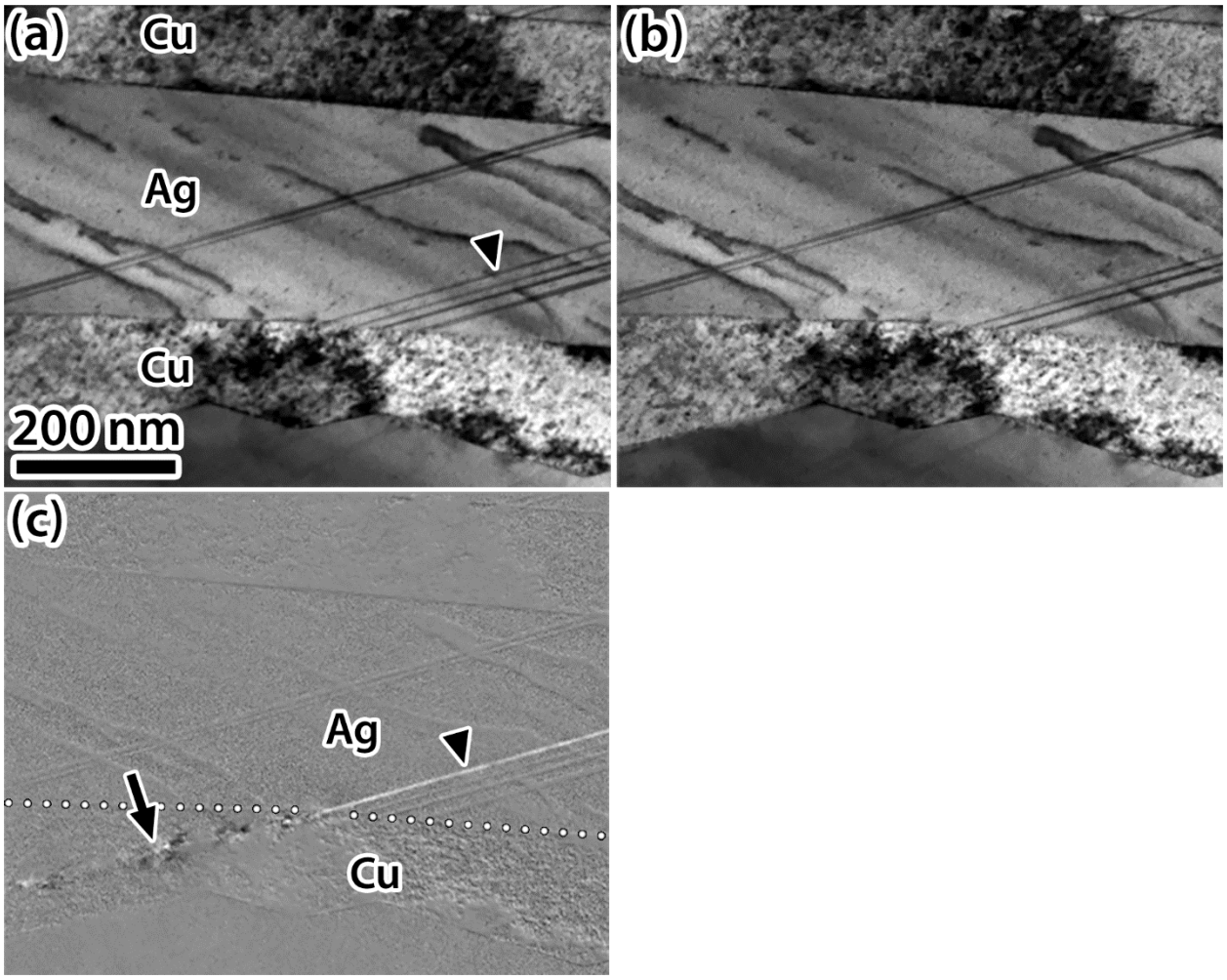

Figure 4.41: (a) and (b) Time resolved *in situ* straining of AgCu eutectic with 500 nm bi-layer thickness and incoherent twin interfaces and (c) difference image. Arrowheads mark stacking faults and the arrow marks displacement location of perfect dislocation slip in Cu. Interface in (c) is marked with the white dotted line.

As the number of dislocations that cross the interface increases, the deformation process can change, with the primary system shutting down and a new slip system being activated. For example, dislocations may be emitted back into a layer rather than being transmitted across the interface. An example of this is shown in Fig. 4.42. Initially perfect dislocations were being transmitted across an incoherent twin boundary from Ag to Cu on the $(1\bar{1}\bar{1})_{\mathrm{Ag,Cu}}$ shared plane which is a slip plane continuous across the interface. With continued straining, the transmission across the interface ceases, and a perfect dislocation is emitted from the interface back into the Ag

layer; the emitted dislocation is marked by an arrowhead in Fig. 4.42(b). The back emitted dislocation is a perfect dislocation on either $(111)_{Ag}$ or $(\bar{1}1\bar{1})_{Ag}$ slip planes. Back emission is likely recovery of the interface from buildup of residual dislocation content from the transmission events. Dislocation transmission frequency across the interface did not increase after the back-emission.

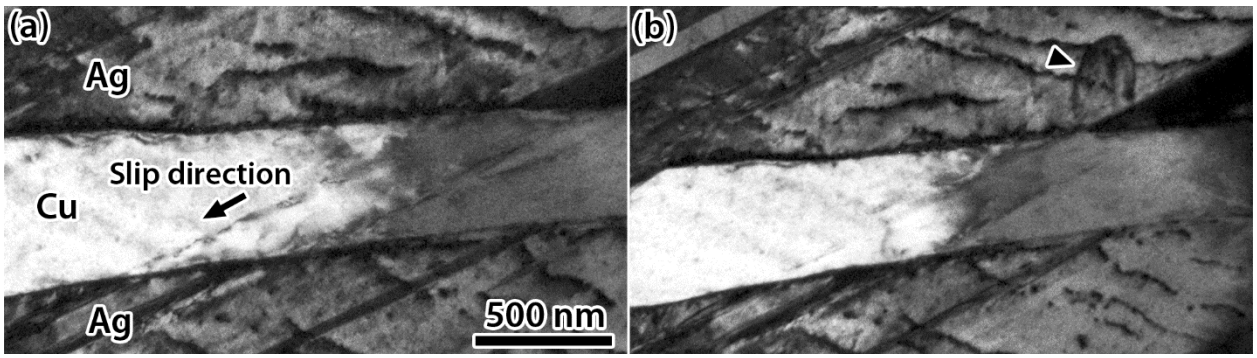

Figure 4.42: (a) and (b) Time resolved images of AgCu eutectic with 500 nm bi-layer thicknesses and incoherent twin interfaces. Arrowhead in (b) marks a dislocation.

Another example of dislocation interactions with already strained interfaces is presented in Fig. 4.43. Perfect dislocations that were in a pile-up that started in Ag_1, marked by arrowheads in Fig. 4.43(a), are observed to have progressed into the next Cu layer, Cu_1, on the twin plane, $(1\bar{1}\bar{1})_{Ag,Cu}$, between the Ag and Cu-phases, in Fig. 4.43(b). Progression into Cu_1 resulted in an increase in the strain contrast in the region marked by the arrow in Fig. 4.43(b). The dislocations could not be distinguished in the Cu_1 layer. Communicating strain from Cu_1 into Ag_2 occurred in stages. The first of the stages, in Fig. 4.43(b), four leading partial dislocations are observed to be emitted from the interface into the Ag_2 layer, marked by arrowheads. The four leading partial dislocations are trailed by stacking faults which are inclined and overlap in the image. Stacking faults cannot be on the same plane and are therefore on neighboring or nearby planes, this indicates the leading partial dislocation emission events occur at different locations of the interface. Further

straining causes trailing partial dislocations to be emitted from the interface which eliminates the fringe contrast associated with the inclined stacking faults and results in perfect or extended dislocations, arrowheads in Fig. 4.43(c). In Fig. 4.43(d), a second slip system is activated, a perfect dislocation on a different slip plane, $(111)_{Ag}$or $(\bar{1}1\bar{1})_{Ag}$. The perfect dislocation is nucleated and slips to the other side of the layer and is incorporated at the Ag/Cu interface; the dislocation is indicated in the image by an arrow.

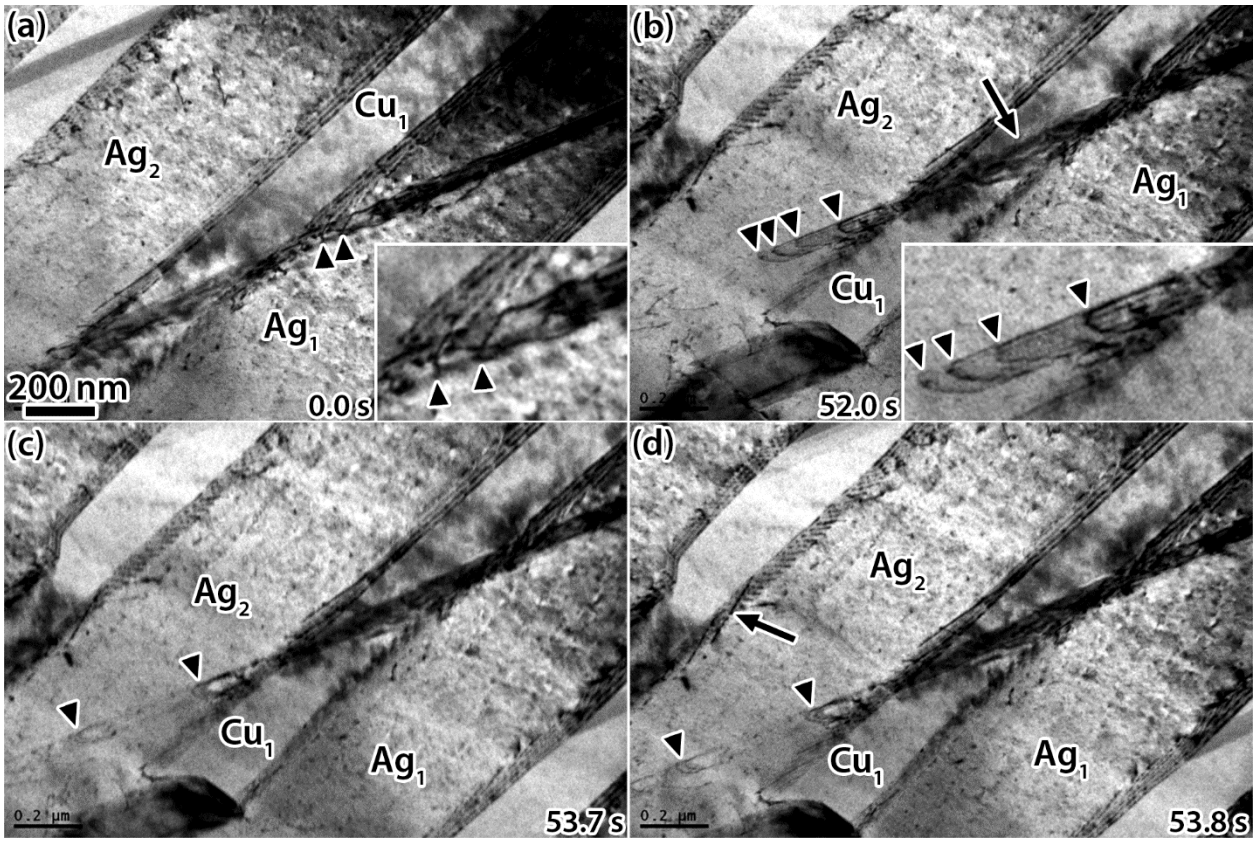

Figure 4.43: (a), (b), (c) and (d) Time resolved *in situ* straining of AgCu eutectic with 500 nm bi-layer thickness and twin incoherent twin interfaces between Ag and Cu. Arrows indicate strain in Cu and emission of a secondary slip system in Ag in (b) and (d) respectively. Arrowheads mark dislocations in Ag.

ii) *Slip on the non-shared planes*

When dislocations are on slip planes that are not the shared plane, the incoherent twin interfaces act as strong barriers. The possible resultant reactions include cross-slip, absorption into the interface and back-emission into the Ag layer, and localized dislocation activity in the adjacent Cu layer. The first example shows an existing dislocation pile-up in Ag on one of the non-twin planes, Fig. 4.44, and shows a dislocation cross-slipping away from the dislocation pile-up. After the cross-slip event, the five dislocation pile-up against an incoherent twin interface between Ag and Cu in Fig. 4.44(a), becomes a four dislocation pile-up in Fig. 4.44(b). Difference image Fig. 4.44(c) was formed by overlaying the inverse of (a) onto (b) and shows the slip trace, which is on the $(1\bar{1}\bar{1})_{\mathrm{Ag}}$ plane, going away from the dislocation pile-up. The arrows in Fig. 4.44(b) and the difference image (c) mark the slip trace of the dislocation that cross-slipped. Slip was limited to the Ag layer as no evidence of dislocation activity in the top Cu layer was found.

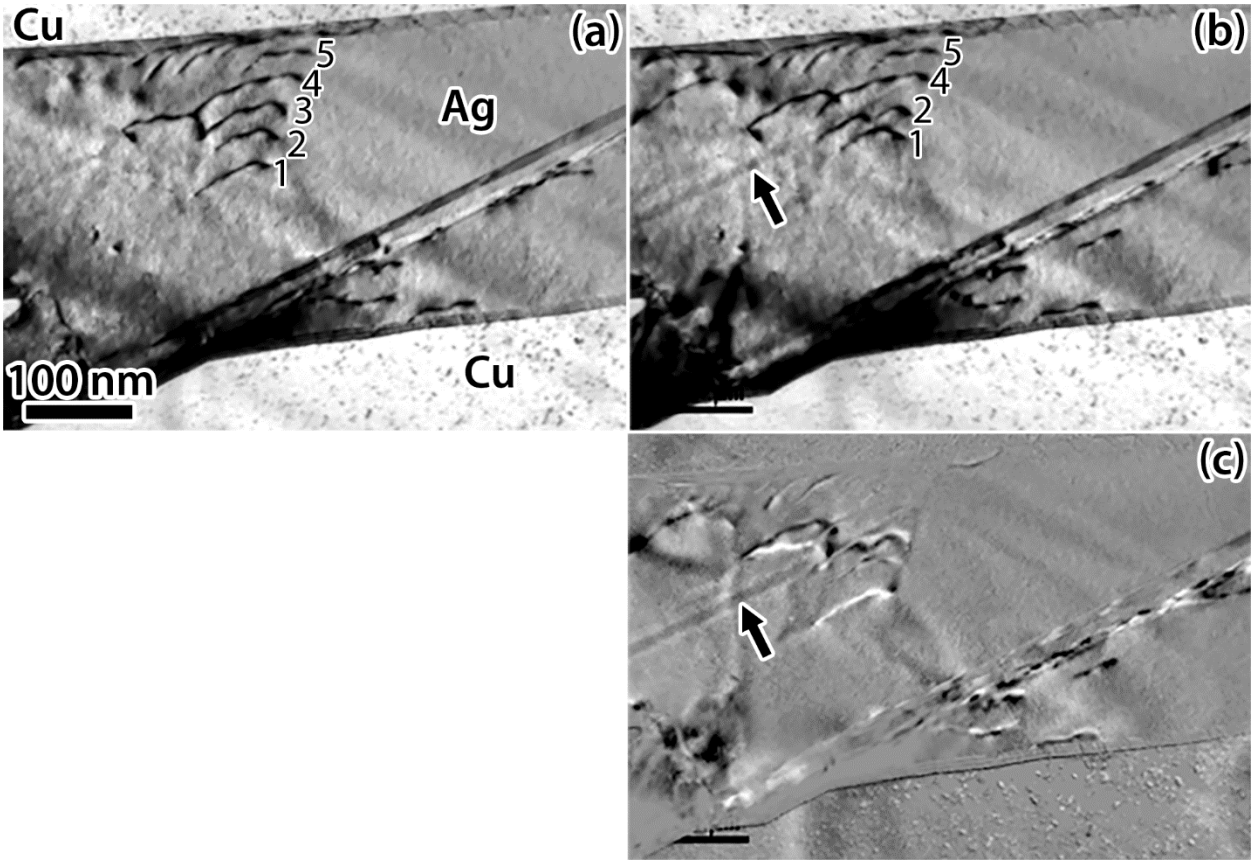

Figure 4.44: (a) and (b) Time resolved images of AgCu eutectic with 500 nm bi-layer thickness and incoherent twin boundaries between Ag and Cu. Image (c) is a difference image. Arrows mark a slip trace.

Emission of dislocations from the interface back into the Ag layer with the dislocation pile-up was also observed during the same straining experiment. In Fig. 4.45(b), emission of a partial dislocation from the interface is marked by an arrow. The emission occurred at a region of the interface that contained multiple dislocations. A short time later a second partial dislocation is emitted and they both extend into the Ag layer each trailing a stacking faults, Fig. 4.45(c). Contrast changes indicating dislocation emission into Cu were not observed throughout the straining indicating the plastic deformation was localized to the Ag layer. This experiment reveals that dislocations on the non-twin plane encounter a large barrier to communication across the interface

and the resulting dislocation pile-ups do not generate sufficient stress for dislocation emission from the incoherent twin interface into the Cu layer.

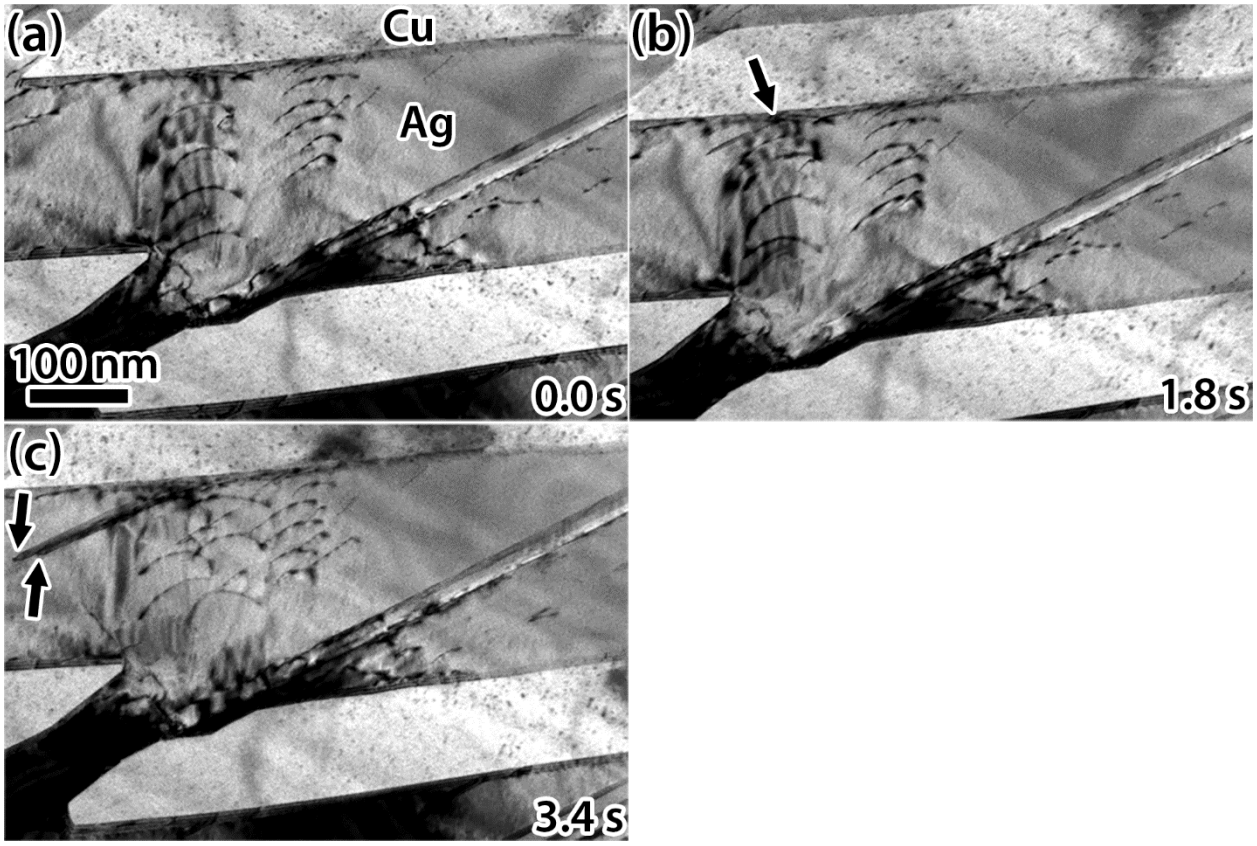

Figure 4.45: (a), (b) and (c) Time resolved images of AgCu eutectic with 500 nm bi-layer thickness and incoherent twin interfaces between Ag and Cu. Arrows in (b) and (c) mark the back emission of dislocations.

When a source for dislocation pile-ups is not present, such as discontinuities of the lamellae, dislocations nucleate more uniformly along the incoherent twin interfaces in Ag. An example of this is shown in Fig. 4.46 with slip of both partial and perfect dislocations occurring on planes other than the shared plane. The $(\bar{1}\bar{1}1)_{\mathrm{Ag}}$ has active slip in addition to $(111)_{\mathrm{Ag}}$ and/or $(\bar{1}1\bar{1})_{\mathrm{Ag}}$ slip planes. Dislocations in the Ag did not emit from a single location but instead at multiple locations along the interface, marked by arrowheads in Fig. 4.46(a). The dislocations emitted in Ag_1 are predominantly partial dislocations which can be seen by the fringe contrast associated with

the stacking faults trailing the dislocations. A few of the dislocations were, however, perfect dislocations. Though only the Ag is in contrast to properly observe dislocations, strain in Cu_1 is evident from the difference images and is marked by arrows in Figs. 4.46(d) and (e). Difference images Figs. 4.46(d) and (e) were formed by overlaying the inverse of (a) onto (b) and (c) respectively. Deformation is induced in the Ag_2 layer at the location of localized strain in the Cu layer, this is marked with an arrowhead in Figs. 4.46(e) and (f). If the strain was transferred plastically across Cu_1, dislocations in Cu_1 did not remain in the layer interiors, and were located in regions of high elastic strain which does not allow them to be observed or characterized experimentally. It is possible that elastic strain in Cu_1 was enough for emission of dislocations into Ag_2. In the course of the straining, deformation of the Ag layers is observed to occur to a greater extent than the Cu layers where deformation is more localized.

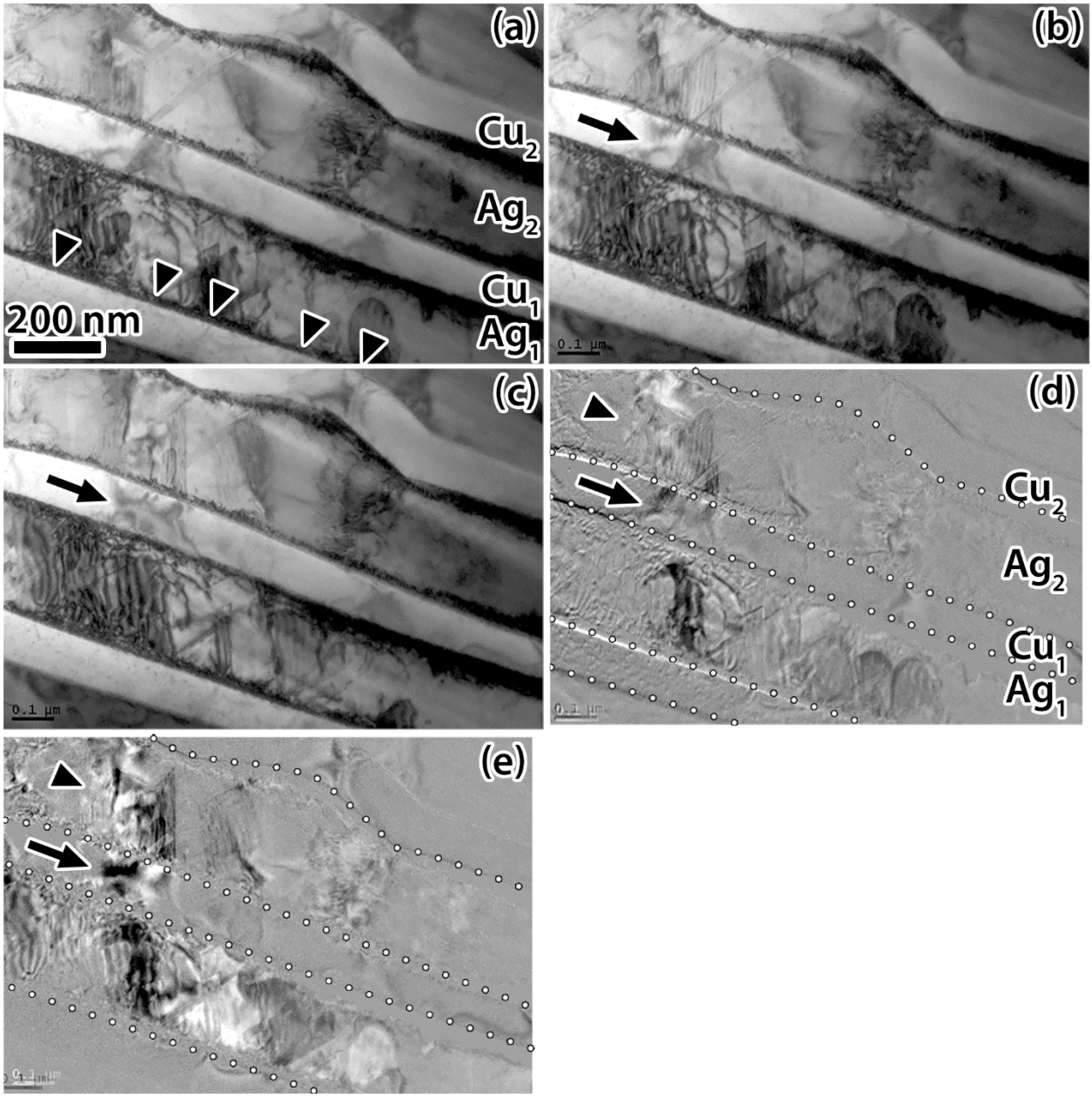

Figure 4.46: (a), (b), and (c) Time resolved *in situ* straining of AgCu eutectic with 500 nm bi-layer thickness and incoherent twin interfaces between Ag and Cu, difference images (d) and (e). Arrowheads mark dislocation nucleation locations in Ag in (a). Arrows mark strain in Cu. Arrowheads in (d) and (e) mark strain in Ag. White dotted lines mark the interfaces in the difference images (d) and (e).

4.3.3 Coherent twin interfaces

In situ TEM straining experiments of the water quenched material containing near coherent twin type interfaces show twinning and detwinning in Ag layers as well as transfer of strain across the Cu layers elastically. An example of this is shown in the series of images presented in Fig. 4.47. To illustrate the changes, difference images are provided as images in Figs. 4.47(d)-(f). Formation of the difference images Figs. 4.47(d) and (e) was done by overlaying the inverse of (a) onto (b) and (c), respectively. Difference image Fig. 4.47(f) is an inset of (e). The difference images in Fig. 4.47 show the strain progresses from the bottom right to the top left. During the straining both twinning and detwinning occur in the Ag layers. Twins that detwin are marked by arrowheads in Figs. 4.47(a) and (b), and the locations of where the twins had been appear white in the difference images (c) and (e), also marked by arrowheads. Twinning is observed by the twinning partial dislocations present as the black dots in the inset of Fig. 4.47(f). In Cu, however, dislocations were not observed and instead the Cu layers exhibited changes in elastic strain contrast which is observed in the difference images.

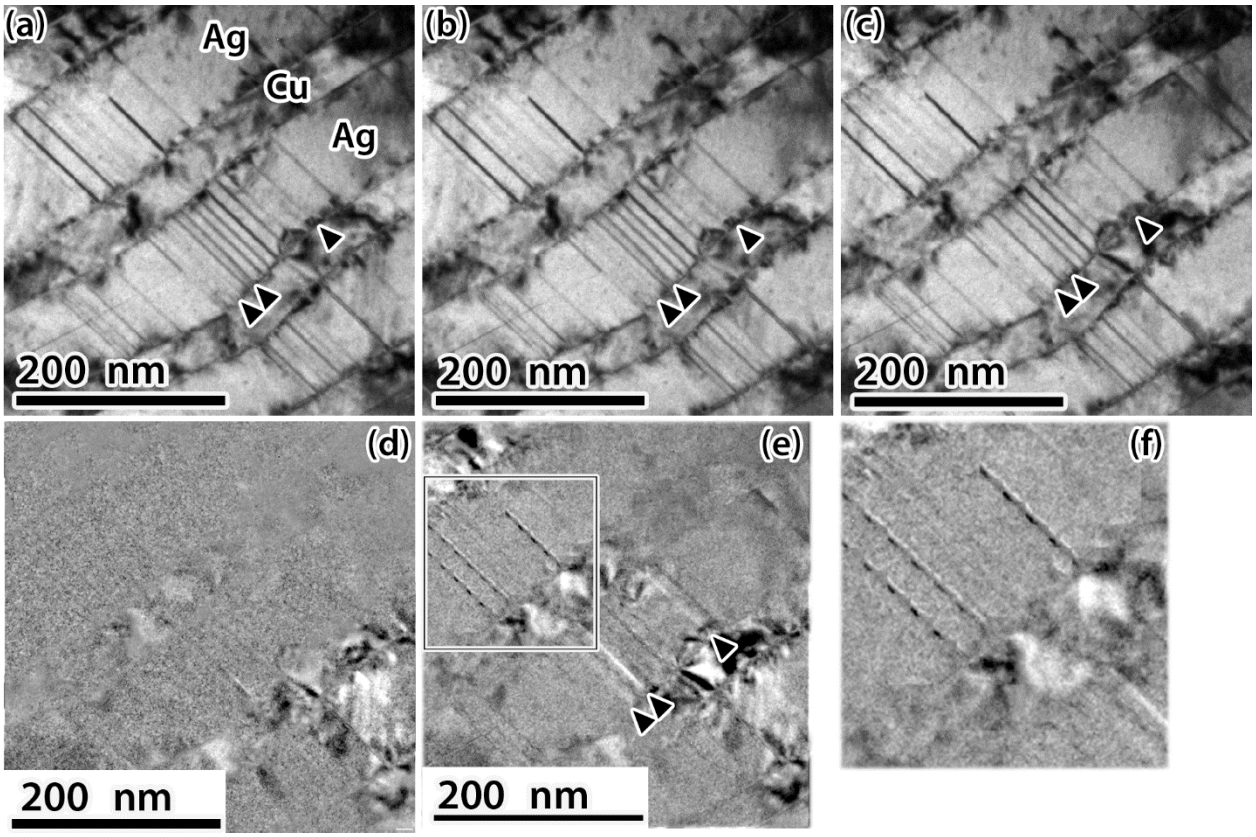

Figure 4.47: (a), (b), and (c) Time resolved *in situ* TEM straining of AgCu eutectic with 150 nm bi-layer thickness and near coherent twin interfaces between Ag and Cu, difference images (d), (e) and (f). (f) is an inset of (e). Arrowheads mark locations of twins.

CHAPTER 5

DISCUSSION

To determine the interactions of perfect and partial dislocations with the different Ag/Cu interfaces two approaches were used: *in situ* TEM straining experiments as well as characterization of the evolved microstructural state following high-strain compressive loading. Processing enabled both cube-on-cube and incoherent twin interfaces to be produced. The interactions will be compared to models previously proposed for bi-phase interfaces and also slip transfer criteria developed for grain boundaries in single-phase metals. Bulk mechanical response is then discussed in terms of interface type dependent dislocation/interface interactions, as well as load orientation dependence in terms of activated slip systems. Experimental observations of interactions of dislocations with the two interface types, $\{111\}_{\mathrm{Ag}}||\{111\}_{\mathrm{Cu}}$ with a cube-on-cube orientation relationship and incoherent twin, will be considered. The key observations that will be discussed are:

1. Deformation twinning is observed in the Cu-phase only when the interface type is cube-on-cube and the deformation twins are associated with deformation twinning in the Ag-phase.
2. Load orientation with respect to the interfaces impacts both deformation mechanisms and mechanical strength.
3. The cube-on-cube interface type is a weak barrier to dislocations, particularly to partial dislocations.
4. The incoherent twin interface is a strong barrier to dislocations except when the dislocations are perfect dislocations on the twin plane.

5.1 Processing and initial structure of AgCu eutectic

Interface type and to a lesser extent bi-layer thickness are important for dislocation/interface interactions, and processing was key to producing cube-on-cube and incoherent twin interfaces using directional solidification. The results are compared to what is expected for eutectics in general as well as specific studies on AgCu eutectic. To compare how the length-scale changes reported here compares to what has been reported by others [18, 19, 36], the bi-layer thickness as a function of growth rate for AgCu eutectic is presented in Fig. 5.1. The datasets from each study were fitted to the expression $\lambda = C * v^k$, where λ is the bi-layer thickness, v is the growth rate and C and k are constants. The values of C and k are compared in Table 5.1. While C was inconsistent between the other studies, k was between -0.452 and -0.590. These values are consistent with eutectic solidification, which generally follows $\lambda^2 v = C$ [122]. In contrast, the results presented in this study yield a value of k that was determined to be -0.272 whereas a value closer to -0.500 was expected. However, with only three data points, it is possible this difference is not significant. Though the relationship $\lambda^2 v = C$ is thought to be independent of morphology it is not known if interface type could be a contributing factor to this difference. To explore the kinetics of solidification, a directionally solidified rod in which the growth rate is varied along the length of the rod should be conducted. In principle, such a test would yield a number of different growth rates which would allow the transition in morphology to be determined and along with it the orientation relationship.

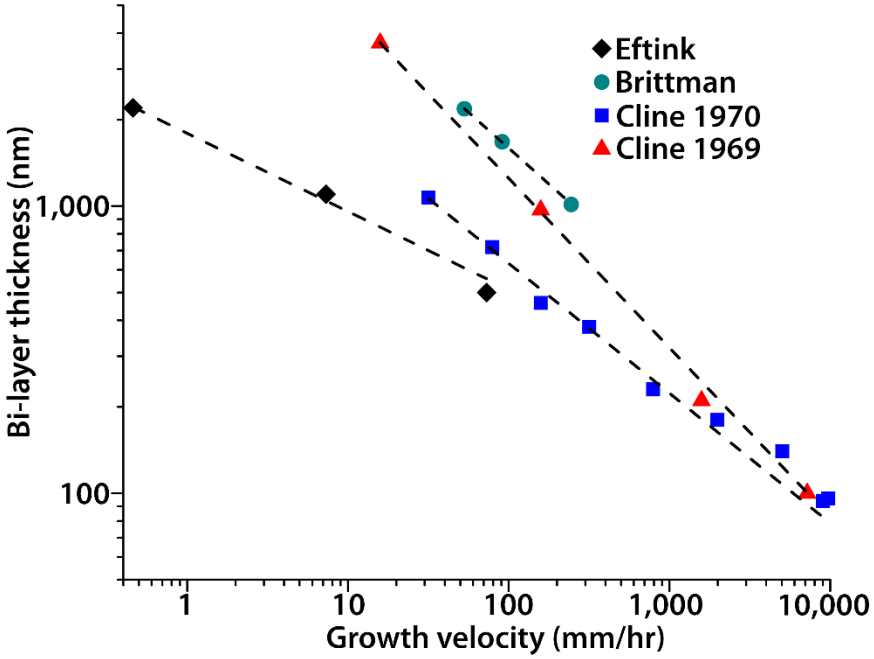

Figure 5.1: Bi-layer thickness as a function of growth velocity for AgCu eutectic in four studies [18, 19, 36].

Table 5.1 : Fitting parameters for $\lambda = C * v^k$ from Fig. 5.1.

$\lambda = C * v^k$		
	C	k
Brittman[19]	15880±430	-0.50±0.01
Cline 1969 [18]	18890±640	-0.59±0.01
Cline 1970 [36]	5069±390	-0.45±0.02
Eftink [123]	1790±60	-0.27±0.02

As reported in Chapter 4, the prevalence of incoherent twin interfaces increases from 0% at 0.46 mm/hr to 15% at 7.3 mm/hr to greater than 66% at 73 mm/hr, with cube-on-cube interfaces accounting for the rest. The interfacial energy of the incoherent twin interface, the cube-on-cube interface and coherent twin interface were compared using molecular dynamics simulations and the interface models are shown in Fig. 5.2 [120]. The simulated interface structures correspond well to the experimental results. The incoherent twin interface with $\{\bar{3}13\}_{Ag}||\{\bar{1}12\}_{Cu}$ habit plane is a low energy configuration, 161 mJ/m^2, which is lower than the energy for the cube-on-cube

orientation relationship with $(111)_{Ag}||(111)_{Cu}$ habit plane interfaces and twin orientation relationship with $(111)_{Ag}||(111)_{Cu}$ habit plane interfaces, which have energies of 251 mJ/m^2 and 243 mJ/m^2, respectively. The transition from cube-on-cube interfaces (higher interfacial energy) to incoherent twin interfaces (lower interfacial energy) as the growth rate increases is not explained by traditional eutectic growth mechanisms. Interface structures, or at least morphology, in eutectics are not considered controllable by the growth rate, except at very high undercoolings when anomalous structures emerge [124-126]. Instead, the relative volume fraction of the phases dictates whether lamellar or fiber morphology occurs in eutectics [122, 127, 128]. This is because the interfacial area is smaller for a fiber morphology when one phase volume fraction is significantly smaller, less than $1/\pi$, otherwise the lamellar structure is predicted [122]. This assumes the interfaces between the phases are isotropic in energy for both morphologies. For the AgCu eutectic, the relative volume fractions straddle that of lamellar and fiber such that both may be observed [19]. In AgCu eutectic, a transition from cube-on-cube interfaces to coherent twin interfaces has been suggested as undercooling increases, however, the transition has not been shown previously [10, 24]. Here, it is shown that a transition from cube-on-cube to incoherent twin interfaces occurs with increasing growth rate in AgCu eutectic. Coherent twin interfaces in AgCu eutectic likely occur at growth rates higher than 73 mm/hr as they have been observed in this work in water quenched material as well as in other studies in which the undercooling was high [10, 24]. Interface type will be shown in the remaining sections to be important in the deformation response.

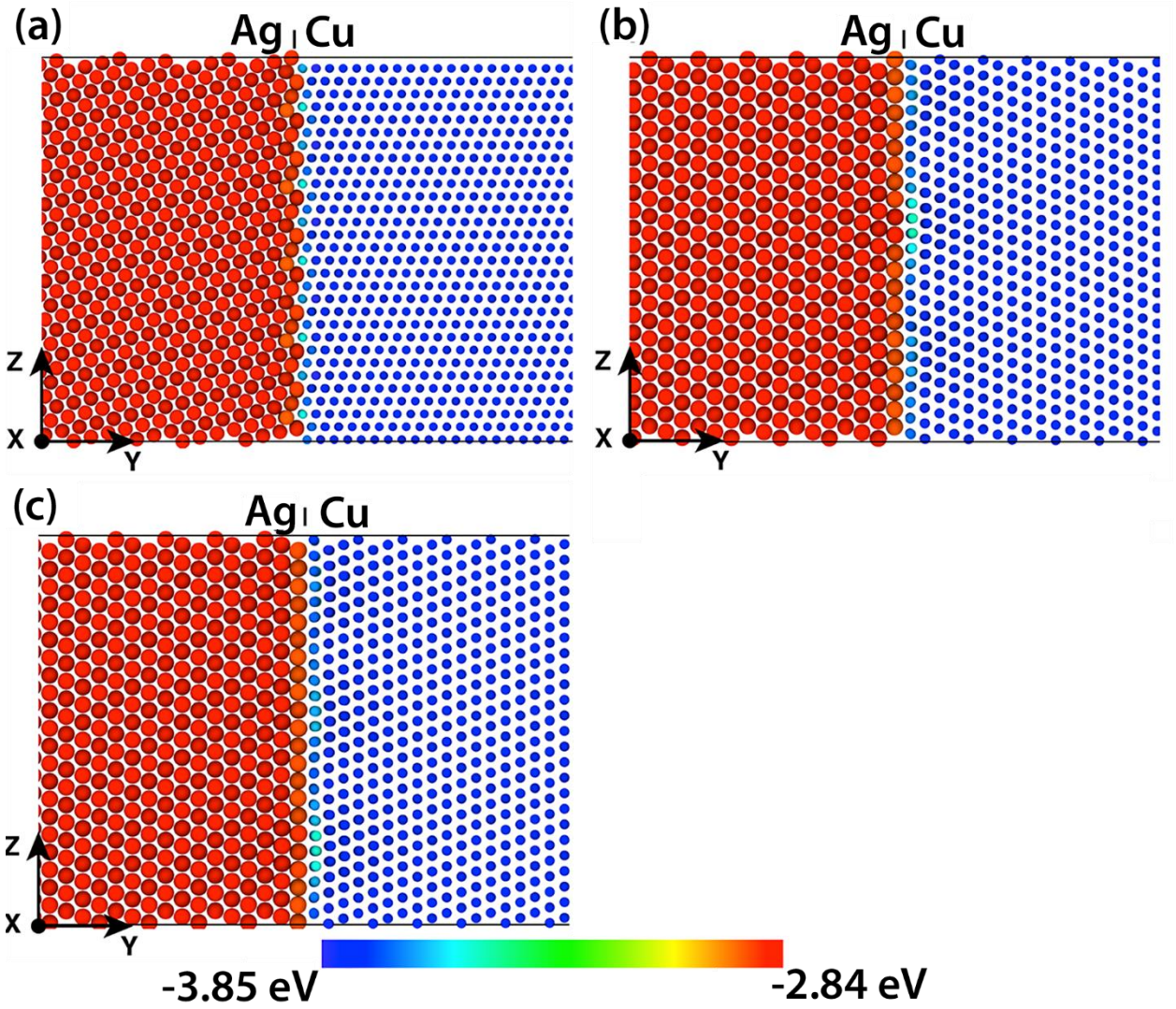

Figure 5.2: MD simulation of the atomic structures of (a) an incoherent twin interface with $\{\bar{3}13\}_{Ag}||\{\bar{1}12\}_{Cu}$ habit plane, (b) a cube-on-cube interface with $\{111\}_{Ag}||\{111\}_{Cu}$ habit plane, and (c) a coherent twin interface with $\{111\}_{Ag}||\{111\}_{Cu}$ habit plane [120].

5.2 Deformed microstructure as a function of length-scale and orientation of interfaces with respect to the load

The deformation response of a AgCu eutectic alloy following high strain-rate loading has been shown to be dependent on the nature of the interface between the Ag and Cu-phases, thickness of the bi-layer, the orientation of the compressive loading with respect to the growth direction, and the crystallographic orientation of the Ag-phase to the loading direction. A summary of the

deformation mechanisms in terms of interface type and bi-layer thickness is presented in Table 5.2. In terms of the impact of the interface type on the deformation response it is seen from Table 5.2 that cube-on-cube interfaces permit transfer of deformation twins into Cu whereas incoherent twin interfaces prohibit transfer of deformation twins. Additionally, the incoherent twin interfaces can act as sources for deformation twins in the Ag layers but not the Cu layers. Dislocation slip can be communicated across incoherent twin interfaces from Ag to Cu, but this appears to be localized. As the bi-layer thickness decreases for both interface types, the dislocation density in Cu is observed to decrease with very few defects observed in the Cu-phase with 500 nm thick bi-layers. When loading, at least, along the growth direction, $[101]_{\mathrm{Ag}}||[110]_{\mathrm{Cu}}$, both Ag and Cu have to deform to the same strain levels suggesting the dislocation slip activity in both should be similar. Image forces would drive dislocations in Cu to the interfaces because Ag is more compliant, this force is inversely proportional to distance which would explain the decrease in dislocation content in Cu with decreasing layer thickness.

For different loading orientations the most significant factor in deformation mechanisms is the crystallographic load orientation. This was observed to dictate the activation of deformation twinning. For example, when loading along the growth direction deformation twinning was not observed. In FCC materials deformation twinning is not a favorable deformation mode for loading in compression along the $\langle 101 \rangle$, which is the growth direction for the directionally solidified AgCu eutectic alloy used [48]. Loading away from the growth axis will have crystallographic load orientations for which deformation twinning is favorable such as in the $[11\bar{1}]$ when loading 90° to the growth direction or the $[001]$ when loading 45° to the growth direction. There also appears to be a component of interface orientation with respect to the load with regards to activation of deformation twinning because loading 45° to the growth direction at both 1100 nm and 500 nm

resulted in a much lower density of deformation twins in Ag and none in Cu. The reason behind interface orientation with respect to the load dependence on deformation twinning is unclear, however, it may be due to twin nucleation from the interface into Ag.

Table 5.2: Summary of the deformation responses as a function of loading direction, bi-layer thickness and interface type.

Bi-layer thickness (nm)	Interface type	Loading direction		
		0°	45°	90°
2200	Cube-on-cube	Dislocation slip in both phases. 10.5% strain	Dislocation slip in both phases. Deformation twinning in both phases. 14.7% strain	Dislocation slip in both phases. Deformation twinning in both phases but only for specific loading orientations. 15.2% strain
1100	Cube-on-cube	Dislocation slip in both phases. 11.1% strain	Dislocation slip in both phases. Deformation twinning in Ag. 25.4% strain	Dislocation slip in both phases. Deformation twinning in both phases. 32% strain
500	Cube-on-cube	Dislocation slip in both phases. 5.5-21.5% strain	Dislocation slip in both phases. Low density of deformation twins in Ag only. 19.1% strain	Dislocation slip in both phases. Deformation twinning in both phases but only for specific loading orientations. 14.2% strain
1100	Incoherent twin	NA	Dislocation slip primarily in Ag Deformation twinning in Ag-phase. 25.4% strain	Dislocation slip primarily in Ag Deformation twinning in Ag. 32% strain
500	Incoherent twin	Dislocation slip primarily in Ag + rotation of the interface. 5.5-21.5% strain	Dislocation slip primarily in Ag. 19.1% strain	Dislocation slip primarily in Ag Deformation twinning in Ag. 14.2% strain

5.3 Inducing deformation twinning in Cu

Ex situ SHPB experiments and *in situ* straining TEM experiments confirm twinning occurs in both Ag and Cu when the orientation relationship between the two is cube-on-cube. It had been proposed for AgCu alloys that deformation twinning in Ag is necessary to initiate deformation twinning in Cu [30]. This conclusion raises the important question about the interaction of twinning partial dislocations in Ag with the interface and causing deformation twinning in the Cu. One possible explanation is that the interface is effectively transparent to the Ag twinning partial dislocations. Molecular dynamics computer simulations of a Ag/Cu interface with a cube-on-cube orientation relationship supports this mechanism [28]. In the simulations, two sets of twinning partial dislocations were considered to be able to form the twin in Ag; partial dislocations with a Burgers vector of $\mathrm{b}_{\mathrm{Ag}} = \frac{a}{6}[112]$ or an equal combination of partial dislocations with Burgers vectors of $\mathrm{b}_{\mathrm{Ag}} = \frac{a}{6}[\bar{2}1\bar{1}]$ and $\mathrm{b}_{\mathrm{Ag}} = \frac{a}{6}[1\bar{2}\bar{1}]$. In the latter case the partial dislocations occur on alternate planes. Interaction of either set of the partial dislocations would result in the formation of intrinsic interfacial dislocations and a rotation of the interface plane. The first set of partial dislocations, $\mathrm{b}_{\mathrm{Ag}} = \frac{a}{6}[112]$, will leave a residual dislocation with a Burgers vector of magnitude, $|\mathrm{b}_{\mathrm{res}}|$ = 0.20 Å for each partial dislocation transmitted and will rotate the interface from $(111)_{\mathrm{M}}$ to $(1\bar{1}1)_{\mathrm{T}}$ where subscripts M and T denote matrix and twin. The second set, alternating partial dislocations with Burgers vectors of $\mathrm{b}_{\mathrm{Ag}} = \frac{a}{6}[\bar{2}1\bar{1}]$ and $\mathrm{b}_{\mathrm{Ag}} = \frac{a}{6}[1\bar{2}\bar{1}]$, would leave a residual dislocation with a Burgers vector of magnitude 0.20 Å for each pair of partial dislocations, that is two dislocations, and a rotation of the interface from $(111)_{\mathrm{M}}$ to $(010)_{\mathrm{T}}$.

The magnitude of the rotation of cube-on-cube interfaces with the passage of twinning partial dislocations can be quantified geometrically. The following are for an initial Ag/Cu interface on the $(\bar{1}\bar{1}1)$ plane and a twin on the $(1\bar{1}\bar{1})$ plane. Note, this selection of planes differs from those defined by Wang *et al.*, but the rotations of the interfaces are equivalent and these planes are consistent with the analysis reported in this work. There are two possible interface rotations. The first considers the interaction of partial dislocations with a Burgers vector of $\frac{a}{6}[12\bar{1}]$. To determine the rotation of the original interface consider the translation caused by one $\frac{a}{6}[12\bar{1}]$ partial dislocation on the $(1\bar{1}\bar{1})$ twin plane as shown in Fig. 5.3(a). This causes a rotation of the original interface by an angle θ. To determine the magnitude of θ, l_1 in Fig. 5.3(b) is determined by dividing the interplanar d_{111} spacing by the $\sin(70.52°)$; the angle is that between two $\{111\}$ planes. To complete the calculation, l_2 as shown in Fig. 5.3(c) is determined by

$$l_2 = \frac{a}{6}[12\bar{1}] * \cos(70.52°) \tag{9}$$

Solving for both l_3 and l_4 yields

$$l_3 = l_1 - l_2 \tag{10}$$

and

$$l_4 = \frac{a}{6}[12\bar{1}] * \sin(70.52°) \tag{11}$$

which gives the magnitude

$$\theta = \tan^{-1}({}^{l_4}/_{l_3}) = 38.9° \tag{12}$$

The sense of this rotation is such that it will rotate the $(1\bar{1}\bar{1})_M$ interface to $(1\bar{1}1)_T$ which is consistent with the magnitude and direction of the rotation observed in Figs. 4.20, 4.23, and 4.38.

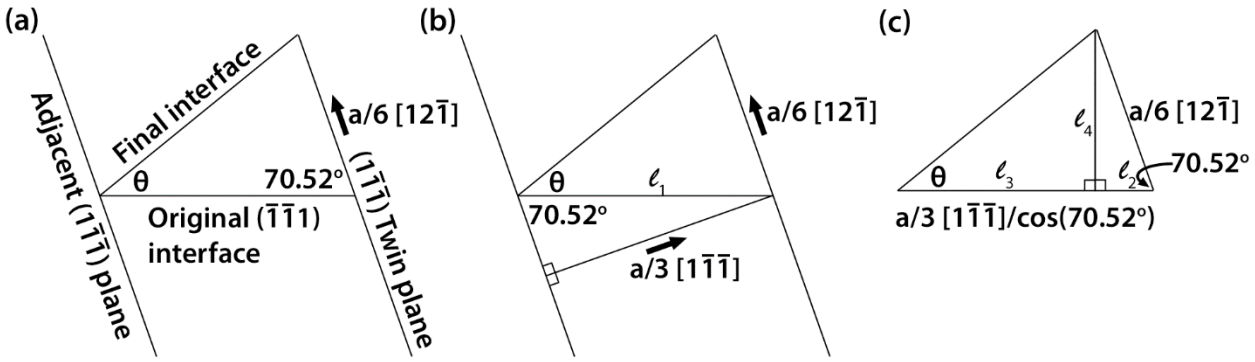

Figure 5.3: Geometric analysis of interface rotation due to the passage of $\frac{a}{6}[12\bar{1}]$ twinning partial dislocations.

The second interfacial rotation is caused by one of either $\frac{a}{6}[\bar{2}\bar{1}\bar{1}]$ or $\frac{a}{6}[1\bar{1}2]$ partial dislocations on the $(1\bar{1}\bar{1})$ twin plane. Each of these dislocations has a shear component of $\frac{a}{12}[\bar{1}\bar{2}1]$ that is not in the interface. From Case I the magnitude of l_1 is known, and from the Thompson tetrahedron the direction of l_1 is known. Therefore, as marked in Fig. 5.4(b), l_1 is the vector $\frac{a}{4}[1\bar{2}\bar{1}]$. By vector addition

$$\frac{a}{4}[1\bar{2}\bar{1}] + \frac{a}{12}[\bar{1}\bar{2}1] = \frac{a}{6}[1\bar{4}\ \bar{1}] \tag{13}$$

and the vectors in equation (13) are marked in Fig. 5.4(c). The angle between the vectors $\frac{a}{4}[1\bar{2}\bar{1}]$ and $\frac{a}{6}[1\bar{4}\bar{1}]$ is 15.8° and this is the magnitude of the interface rotation. This results in an interface of $(001)_T$ which, again, is consistent with the experimental observations, see Fig. 4.34.

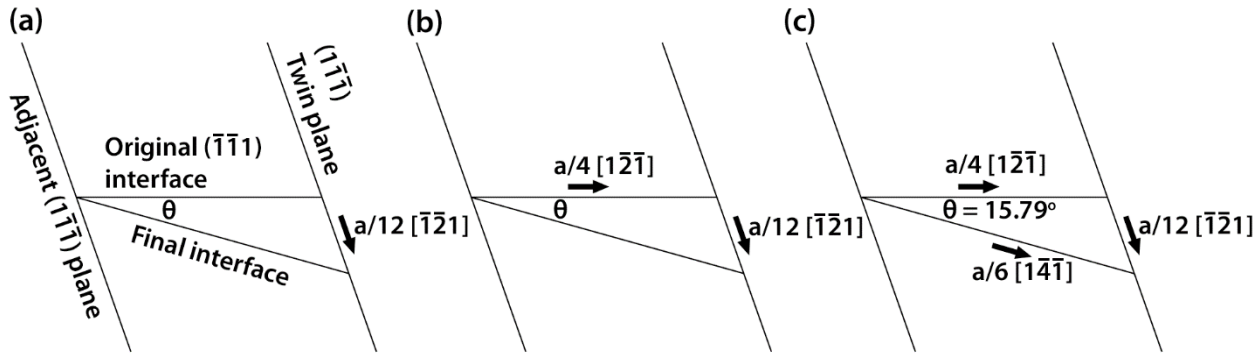

Figure 5.4: Geometric analysis of interface rotation due to the passage of either $\frac{a}{6}[\bar{2}\bar{1}\bar{1}]$ or $\frac{a}{6}[1\bar{1}2]$ twinning partial dislocations.

Wang *et al*. proposed that the rotation of the interface to $(010)_T$ is more favorable because reactions involving a set of Ag twinning partial dislocations with different Burgers vectors transmit more easily than twin partial dislocations of a single type [28]. This is from the smaller magnitude of the residual dislocations left at the interface [28]. For example, if one of $\frac{a}{6}[\bar{2}\bar{1}\bar{1}]$ and $\frac{a}{6}[1\bar{1}2]$ partial dislocations on the $(1\bar{1}\bar{1})$ twin plane slip on neighboring planes, the combined Burgers vector for the two twinning partial dislocations is

$$\frac{a}{6}[\bar{2}\bar{1}\bar{1}] + \frac{a}{6}[1\bar{1}2] = \frac{a}{6}[\bar{1}\bar{2}1]$$

which is the same magnitude of one partial dislocation, transmitting the two will result in a $|b_{res}|$ of 0.20 Å by a transmission event. The study assumed an equal combination of two different partial dislocations and not one or the other. If the twining partial dislocations were exclusively one or the other, the residual Burgers vector would be the same as the first case. The study did not account for interfacial energy of the rotated region of interface, $(111)_{Ag}||(111)_{Cu}$ has an interfacial energy of 247 mJ/m^2 compared to $(100)_{Ag}|(100)_{Cu}$ with an energy of 395 mJ/m^2 [129], rotating to a higher interface energy would have an associated energy cost. Both interface rotations were observed in experiments presented here, Figs. 4.18, 4.20, 4.23, and 4.38 correspond to the

larger rotation and Fig. 4.34 to the smaller rotation. In the limited observations made in this work the larger rotation was observed more frequently. Additionally, Wang *et al.* suggested that the total energy of the accumulated intrinsic interfacial dislocations could be reduced by the interface ejecting other dislocations in addition to the Cu twinning partial dislocations [28]. Such a response from an interface occurred during multiple *in situ* TEM straining experiments but not in relation to the transfer of twinning partial dislocations across the interface. It would appear that the process of deformation twin transfer across a cube-on-cube interface is controlled by, minimization of the accumulation of intrinsic interfacial dislocations and not the preference of deformation mode for Cu which would otherwise not twin [28]. It also was found experimentally, see Fig. 4.38, that the deformation twins were transmitted from the Cu back into the Ag through a cube-on-cube interface. The rotation of the interface was of equal magnitude and direction as caused by the transfer of a twin from Ag to Cu. The independence of the rotation on the direction of twin transfer, Ag to Cu or Cu to Ag, can be accounted for by the geometric arguments. What remains to be discovered are the conditions under which a deformation twin in Ag is able to generate a deformation twin in Cu. In fact, blockage of the Ag deformation twins was common in the experiments. Molecular dynamics simulations of Li and Szlufarska suggest that the periodic array of misfit dislocations in the interface hinder the communication across it [130]. The role of these misfit dislocations remains to be verified. However, in a cube-on-cube interface they are spaced every 18.76 Å. The interplanar spacing of {111} planes in Ag is 2.36 Å. Therefore, even a deformation twin of just eight layers would encounter an interface dislocations. This suggests that other factors may be important in determining if a deformation twin in Ag generates one in Cu.

Incoherent twin interfaces did not allow communication of twinning partial dislocations from Ag into Cu. Deformation twinning in Cu is not expected on its own under the same loading

conditions though occasionally twins, either deformation or annealing, are observed in the Cu layers when the interfaces are incoherent twin. Twinning deformation is prohibited from direct communication across the incoherent twin interfaces even on the shared plane because the Burgers vectors of twinning partial dislocations for Ag and Cu are opposite in direction for this orientation relationship; this is discussed in detail in the next section. Nucleation of deformation twins from the interfaces into Cu also needs to be considered. Though a different material system, a study conducted on Cu/Nb bi-layers with $\{112\}\langle 110\rangle_{\mathrm{Cu}}||\{112\}\langle 111\rangle_{\mathrm{Nb}}$ interfaces as well as Kurdjumov-Sachs and Nishiyama-Wasserman interface types suggests two mechanisms for the generation of twins in Cu layers, (i) dissociation of twinning partial dislocations from the interfaces into Cu and (ii) transmission of dislocations from Nb into Cu twinning partial dislocations [85]. The stepped nature of the incoherent twin interfaces in the AgCu system places it as favorable to nucleate twins from the dissociation of twinning partial dislocations from the interface, however, deformation twins were not observed to nucleate from the interface and propagate into the Cu layer. The slip continuity for the cube-on-cube interfaces places it as favorable for twinning in Cu which is consistent with the experimental observations. Comparing the cube-on-cube and incoherent twin interface types reveals for the AgCu system that the transmissibility is applicable for twinning in Cu is applicable and the dissociation of interfacial dislocations for twinning in Cu is not at the layer thicknesses studied.

5.4 Comparison to strain transfer mechanisms

The *in situ* TEM straining observations of dislocation interactions with the Ag/Cu interfaces were consistent with dislocation reactions across grain boundaries in single-phase FCC materials. The controlling factor is related to the magnitude of the Burgers vector of the residual dislocation generated in the grain boundary by the transmission event [131]. This controlling condition

appears to be independent of dislocation type as well as grain boundary character in single phase materials [86]. The following discussion relates the experimental observations to the residual dislocation content left at the interfaces by the act of dislocation transmission through cube-on-cube and incoherent twin interfaces in a Ag/Cu eutectic alloy.

5.4.1 Cube-on-cube interfaces

Cube-on-cube interfaces are a simple case in regards to strain transfer because of the geometric relationship between the Ag and Cu-phase. The orientation relationship of Ag and Cu is visualized in Fig. 5.5 in which the Thompson tetrahedron for each phase is shown and the $(1\bar{1}\bar{1})_{\mathrm{Ag}}||(1\bar{1}\bar{1})_{\mathrm{Cu}}$ interface is shown as the grey plane. The Ag and Cu are crystallographically aligned such that the slip systems across the interfaces match. Consequently, the resolved shear stresses on the incoming and outgoing slip systems are similar and the transfer process generates an interface dislocation with a small Burgers vector. Therefore, the barriers to the transfer of perfect and partial dislocations are coherency strains, image (Koehler) stresses, energy to create a step at the interface, and interactions with the interface misfit dislocations [12, 18, 69]. It is predicted that dislocations after overcoming the barriers characteristic of bi-phase interfaces should communicate across the interfaces directly. Twinning partial dislocations were commonly observed to directly transmit across cube-on-cube interfaces in both *in situ* and *ex situ* TEM straining experiments. Direct transmission of a twinning partial dislocation from Ag into Cu leaves a small $|\mathrm{b}_{\mathrm{res}}|$ of 0.20 Å, and the lines of intersection of the slip planes with the interfaces match for the incoming and outgoing slip. Perfect dislocations observed in the *in situ* TEM straining experiments required the presence of a dislocation pile-up for transmission to occur. Like direct transmission of partial dislocations, a perfect dislocation absorbing into a Ag/Cu interface and emitting as a perfect dislocation on the same slip system in the neighboring phase requires leaving a dislocation with $|\mathrm{b}_{\mathrm{res}}|$= 0.34 Å, and

the lines of intersection of the slip planes with the interface match for the incoming and outgoing slip systems. All of the slip transfer criteria predict this to occur including the Livingston and Chalmers criterion, both geometric criteria, and the LRB criteria.

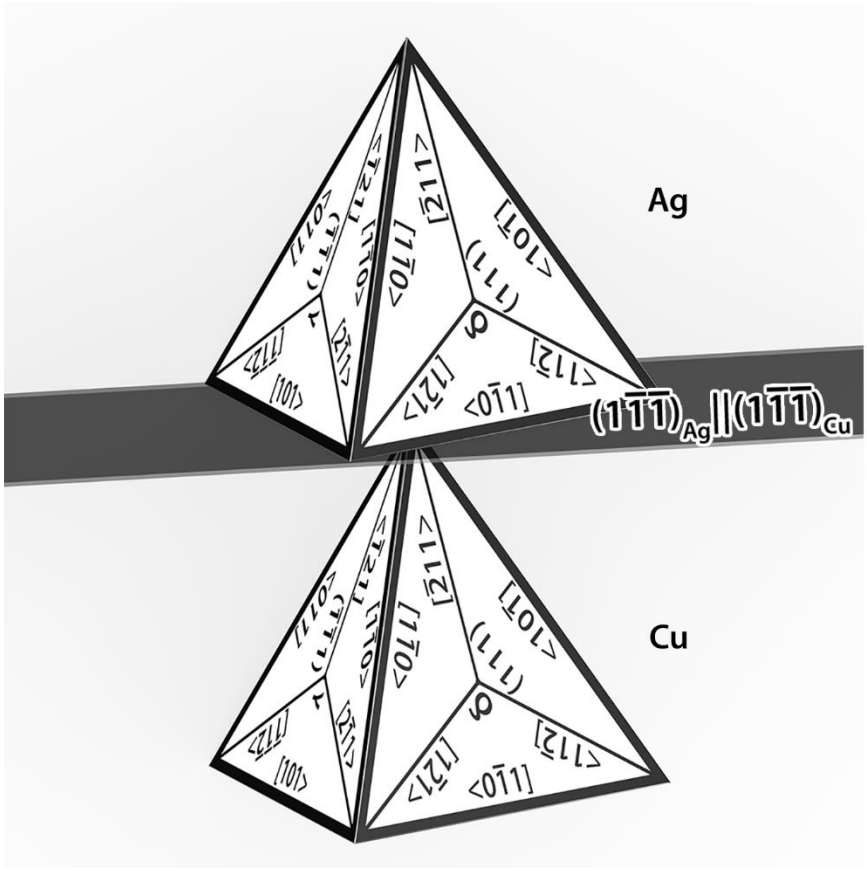

Figure 5.5: Crystallographic alignment of Ag and Cu with cube-on-cube interfaces as shown by the Thompson tetrahedra. The grey plane marks the interface.

5.4.2 Incoherent twin interfaces

Geometrically, incoherent twin interfaces are more complicated than the cube-on-cube interfaces. Dislocations encountering incoherent twin interfaces can be split into dislocations on the twin plane and dislocations on non-twin planes. The non-twin planes are equivalent due to symmetry of the twin orientation relationship. The barrier strength of incoherent twin boundaries to slip transmission is attributed to geometric factors of the boundary. Similar to a coherent twin

boundary, the incoherent twin boundary can either be a strong or weak barrier to dislocations. With coherent twin interfaces for example, screw dislocations can cross-slip across it without generating a residual dislocation if the lines of intersection with the boundary of the incoming and outgoing systems are the same and contained in the boundary [132, 133]. For all other slip interactions, the coherent twin boundary acts as a barrier. The incoherent twin boundary brings an additional path for dislocations to encounter a weak barrier and that is perfect dislocations on the twin plane, which is continuous across the interface. The interface geometry is visualized in Fig. 5.6 where the interface between Ag and Cu is the grey plane, and the twin plane is the green plane. In this Figure, the Thompson tetrahedra for included in the Ag and Cu layers and are oriented with respect to each other to take into account the twin orientation relationship.

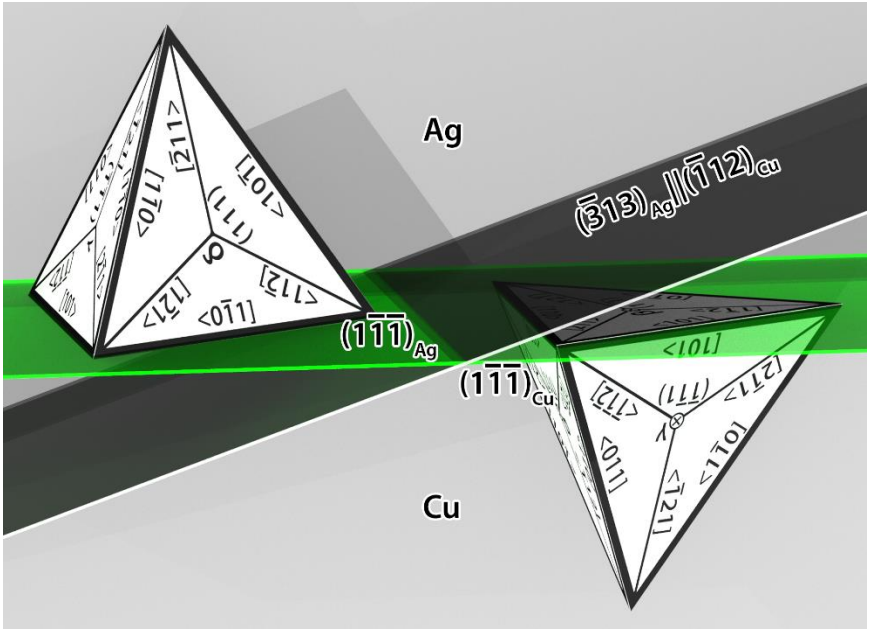

Figure 5.6: Crystallographic alignment of Ag and Cu with incoherent twin interfaces as shown by the Thompson tetrahedra. The grey plane marks the interface. The green plane marks the twin plane.

i.) Dislocations on the twin plane

Perfect dislocations on the twin plane in the Ag and the Cu are well-aligned with each other and the following dislocation reactions are predicted to leave minimal residual dislocation content at the interface: $\frac{a}{2}[101]_{\mathrm{Ag}}(1\bar{1}\bar{1})_{\mathrm{Ag}} \leftrightarrow \frac{a}{2}[110]_{\mathrm{Cu}}(1\bar{1}\bar{1})_{\mathrm{Cu}}$, $\frac{a}{2}[0\bar{1}1]_{\mathrm{Ag}}(1\bar{1}\bar{1})_{\mathrm{Ag}} \leftrightarrow \frac{a}{2}[101]_{\mathrm{Cu}}(1\bar{1}\bar{1})_{\mathrm{Cu}}$, $\frac{\mathrm{a}}{2}[110]_{\mathrm{Ag}}(1\bar{1}\bar{1})_{\mathrm{Ag}} \leftrightarrow \frac{a}{2}[01\bar{1}]_{\mathrm{Cu}}(1\bar{1}\bar{1})_{\mathrm{Cu}}$. After taking into account the 2° missorientation about the $[101]_{\mathrm{Ag}}$ and the difference in lattice parameters between Ag and Cu, the $|\mathrm{b}_{\mathrm{res}}|$ left for those reactions is 0.35 Å. The $|\mathrm{b}_{\mathrm{res}}|$ component due to the difference in lattice parameter only is 0.34 Å. The component due to the 2° misorientation is ignored through the rest of the analysis as it is small. Several reactions of perfect dislocations on the twin plane are listed in Table 5.3 along with the angle between the normal of the incoming and outgoing slip planes, the magnitude of Burgers vector of the residual dislocation left at the interface, and m'. From *in situ* TEM straining experiments, it was found that perfect dislocations on the twin plane absorb into the Ag/Cu interface and emit into the next lamellae on the same plane (the twin plane which is shared), for example in Figs. 4.41-4.43. All of the slip transfer criteria including the Livingston and Chalmers criterion, both geometric criteria, and the LRB criteria rationalize this observation.

Table 5.3: Dislocation reactions from Ag into Cu and corresponding angle between the slip plane normals, $|b_{res}|$, and m′ (geometric criterion) value.

Dislocation reaction at interface	Angle between slip plane normals	Magnitude of Burgers vector of the residual dislocation left at the interface (Å)	m′ (geometric criterion)
$\frac{a}{2}[0\bar{1}1](1\bar{1}\bar{1})_{Ag} \rightarrow \frac{a}{2}[101](1\bar{1}\bar{1})_{Cu}$	0.0	0.34	1.00
$\frac{a}{2}[0\bar{1}1](1\bar{1}\bar{1})_{Ag} \rightarrow \frac{a}{2}[101](\bar{1}\bar{1}1)_{Cu}$	70.5	0.34	0.33
$\frac{a}{2}[101](1\bar{1}\bar{1})_{Ag} \rightarrow \frac{a}{2}[110](1\bar{1}\bar{1})_{Cu}$	0.0	0.34	1.00
$\frac{a}{2}[101](1\bar{1}\bar{1})_{Ag} \rightarrow \frac{a}{2}[110](\bar{1}1\bar{1})_{Cu}$	70.5	0.34	0.33
$\frac{a}{2}[110](1\bar{1}\bar{1})_{Ag} \rightarrow \frac{a}{2}[01\bar{1}](1\bar{1}\bar{1})_{Cu}$	0.0	0.34	1.00
$\frac{a}{2}[110](1\bar{1}\bar{1})_{Ag} \rightarrow \frac{a}{2}[01\bar{1}](111)_{Cu}$	70.5	0.34	0.33
$\frac{a}{2}[0\bar{1}1](1\bar{1}\bar{1})_{Ag} \rightarrow \frac{a}{6}[2\bar{1}1](\bar{1}\bar{1}1)_{Cu}$	70.5	1.78	0.29
$\frac{a}{2}[0\bar{1}1](1\bar{1}\bar{1})_{Ag} \rightarrow \frac{a}{6}[1\bar{1}2](1\bar{1}\bar{1})_{Cu}$	0.0	1.78	0.87

The Burgers vectors of the three different leading partial dislocation on the twin plane in Ag are opposite in direction to the ones in Cu when the Ag and Cu have a twin orientation relationship. Results from both *in situ* and *ex situ* straining confirm stacking faults and twins in the Ag-phase rarely result in stacking faults in the Cu-phase. The generation of a perfect or a partial dislocation in Cu due to the interaction of a partial dislocation in Ag interacting with an incoherent twin interface produces a Burgers vector with a minimum magnitude of 1.39 Å and 1.30 Å, respectively. No cases of partial dislocations on the twin plane impinging on the incoherent twin interfaces were observed to generate slip in the next lamellae, which is probably due to the large magnitude of the Burgers vector of the residual dislocation that would be required to be left at the interface. Several of the dislocation reactions are presented in Table 5.4. An example of where the geometric criterion, m', deviates significantly from $|b_{res}|$ left at the interface is in the case of $\frac{a}{6}[1\bar{1}2](1\bar{1}\bar{1})_{Ag} \rightarrow \frac{a}{2}[110](1\bar{1}\bar{1})_{Cu}$ where $|b_{res}|$ is unfavorably large, 1.39 Å, and m′ is favorably

large, 0.866. The discrepancy is due to the reaction having a partial dislocation in Ag and a perfect dislocation in Cu. Since partial dislocations have a smaller magnitude of Burgers vector than perfect dislocations, the angle between the incoming and outgoing Burgers vectors does not correlate well to $|b_{res}|$.

Table 5.4: Dislocation reactions from Ag into Cu and corresponding angle between the slip plane normals, $|b_{res}|$, and m′ (geometric criterion) value.

Dislocation reaction at interface	Angle between slip plane normals	Magnitude of the Burgers vector of the residual dislocation left at the interface (Å)	m′ (geometric criterion)
$\frac{a}{6}[1\bar{1}2](1\bar{1}\bar{1})_{Ag} \rightarrow \frac{a}{2}[101](\bar{1}\bar{1}1)_{Cu}$	70.5	1.39	0.29
$\frac{a}{6}[1\bar{1}2](1\bar{1}\bar{1})_{Ag} \rightarrow \frac{a}{2}[110](1\bar{1}\bar{1})_{Cu}$	0.0	1.39	0.87
$\frac{a}{6}[1\bar{1}2](1\bar{1}\bar{1})_{Ag} \rightarrow \frac{a}{6}[21\bar{1}](\bar{1}1\bar{1})_{Cu}$	70.5	1.30	0.22

ii) Dislocations on non-twin plane

All of the planes that are not the twin plane have equivalent dislocation reactions in terms of residual Burgers vectors because of symmetry. Therefore only the $(\bar{1}1\bar{1})$ slip plane will be discussed, however, the analysis is the same as for the (111) and $(\bar{1}\bar{1}1)$ planes. From *in situ* TEM straining experiments the observed perfect dislocations were blocked by the interfaces when on these planes, Figs. 4.44 and 4.45. This is likely because the $|b_{res}|$ generated by the possible reactions, minimum of 1.61 Å and 1.53 Å for emitting perfect and partial dislocations respectively, is much higher than for reactions of perfect dislocations on the twin plane, and are therefore less likely. The exceptions involve the cross-slip of screw dislocations across the interfaces. Unlike a coherent twin interface, an incoherent twin has two slip planes a screw dislocation can cross-slip across the interface onto. For the slip system $\frac{a}{2}[110](\bar{1}1\bar{1})_M$, communication into the next layer can be accomplished by cross-slip onto the twin plane, $\frac{a}{2}[01\bar{1}](1\bar{1}\bar{1})_T$, or the $(\bar{1}\bar{1}1)_T$ non-twin

plane, $\frac{a}{2}[01\bar{1}](111)_{\mathrm{T}}$. The cross-slip events across the incoherent twin interface would leave a residual dislocation with a $|\mathrm{b}_{\mathrm{res}}|$ of 0.34 Å. This type of cross-slip was not observed. Observations of perfect dislocations on the non-twin plane, however, were limited and the Burgers vectors of the dislocations could not be determined conclusively. Therefore, favorability of cross-slip cannot be definitively stated. Several of the dislocation reactions for perfect dislocations on the non-twin plane are provided in Table 5.5.

Table 5.5: Dislocation reactions from Ag into Cu and corresponding angle between the slip plane normals, $|\mathrm{b}_{\mathrm{res}}|$, and m′ (geometric criterion) value.

Dislocation reaction at interface	Angle between slip plane normals	Magnitude of the Burgers vector of the residual dislocation left at the interface (Å)	m′ (geometric criterion)
$\frac{a}{2}[110](\bar{1}1\bar{1})_{\mathrm{Ag}} \rightarrow \frac{a}{2}[01\bar{1}](111)_{\mathrm{Cu}}$	39.0	0.34	0.78
$\frac{a}{2}[110](\bar{1}1\bar{1})_{\mathrm{Ag}} \rightarrow \frac{a}{2}[11\bar{2}](111)_{\mathrm{Cu}}$	39.0	1.78	0.67
$\frac{a}{2}[011](\bar{1}1\bar{1})_{\mathrm{Ag}} \rightarrow \frac{a}{2}[\bar{1}10](111)_{\mathrm{Cu}}$	39.0	1.60	0.65
$\frac{a}{2}[011](\bar{1}1\bar{1})_{\mathrm{Ag}} \rightarrow \frac{a}{2}[\bar{1}21](\bar{1}\bar{1}1)_{\mathrm{Cu}}$	56.3	1.53	0.53

Partial dislocations on the non-twin plane, however, were prevalent. Partial dislocations on the non-twin planes were observed to be blocked by the interfaces, Fig. 4.46. With the $\frac{a}{6}[\bar{1}12]_{\mathrm{Ag}}(\bar{1}1\bar{1})$ slip system, the smallest residual dislocation left at the interface would have a $|\mathrm{b}_{\mathrm{res}}|$ of 1.05 Å to communicate to a perfect dislocation in Cu. The other partial dislocations $\frac{a}{6}[\bar{1}\bar{2}\bar{1}]_{\mathrm{Ag}}$ and $\frac{a}{6}[21\bar{1}]_{\mathrm{Ag}}$ both result in at least a $|\mathrm{b}_{\mathrm{res}}|$ of 1.39 Å to communicate into a perfect dislocation in Cu. Any of the partial dislocations on the non-shared planes in Ag reacting to a partial dislocations in Cu, see Table 5.6, can leave a much smaller residual dislocation, with a $|\mathrm{b}_{\mathrm{res}}|$ of 0.56 Å comparable to the $|\mathrm{b}_{\mathrm{res}}|$ 0.34 Å the experimentally observed reactions with the perfect dislocations on the twin plane. Emitting a partial dislocation and therefore creating a

stacking fault into Cu, however, may be unfavorable because Cu has a stacking fault energy of 40 mJ/m^2 as compared to 11 mJ/m^2 for Ag.

Table 5.6: Dislocation reactions from Ag into Cu and corresponding angle between the slip plane normals, $|b_{res}|$, and m′ (geometric criterion) value.

Dislocation reaction at interface	Angle between slip plane normals	Magnitude of residual dislocation Burgers vector left at the interface (Å)	m′ (geometric criterion)
$\frac{a}{6}[\bar{1}12](\bar{1}1\bar{1})_{\mathrm{Ag}} \rightarrow \frac{a}{2}[011](\bar{1}\bar{1}1)_{\mathrm{Cu}}$	56.3	1.05	0.53
$\frac{a}{6}[21\bar{1}](\bar{1}1\bar{1})_{\mathrm{Ag}} \rightarrow \frac{a}{2}[01\bar{1}](111)_{\mathrm{Cu}}$	38.9	1.39	0.67
$\frac{a}{6}[\bar{1}\bar{2}\bar{1}](\bar{1}1\bar{1})_{\mathrm{Ag}} \rightarrow \frac{a}{2}[0\bar{1}1](111)_{\mathrm{Cu}}$	38.9	1.39	0.67
$\frac{a}{6}[21\bar{1}](\bar{1}1\bar{1})_{\mathrm{Ag}} \rightarrow \frac{a}{6}[11\bar{2}](111)_{\mathrm{Cu}}$	38.9	0.56	0.73
$\frac{a}{6}[\bar{1}\bar{2}\bar{1}](\bar{1}1\bar{1})_{\mathrm{Ag}} \rightarrow \frac{a}{6}[1\bar{2}1](111)_{\mathrm{Cu}}$	38.9	0.56	0.73
$\frac{a}{6}[\bar{1}12](\bar{1}1\bar{1})_{\mathrm{Ag}} \rightarrow \frac{a}{6}[\bar{1}21](\bar{1}\bar{1}1)_{\mathrm{Cu}}$	56.3	0.56	0.52

In summary, minimization of the residual Burgers vector at the interface corresponded well to predicting if strain transfers across an interface. When the reaction results in a small $|b_{res}|$ <0.56 Å, strain was observed to transfer across the interface even driving twinning in Cu when it otherwise would deform by dislocation slip only. With larger $|b_{res}|$, dislocation slip was effectively blocked by the interface. It was also determined that the geometric criterion $m' = \cos(\phi) \cdot \cos(\kappa)$, where ϕ is the angle between the slip plane normals, and κ the angle between the slip directions of the two neighboring crystals, does not predict the observed outcome when the reactions involve a perfect incoming dislocation and a partial outgoing dislocation and vice versa. The role of resolved shear stress on the outgoing system was not determined.

5.5 Bulk mechanical response in terms of deformation processes

Mechanical strength of the material as presented in Fig. 4.14, can be rationalized by the bi-layer thickness, interface type, and activated slip systems. While yield stress increased for decreasing bi-layer thickness, there was a significant increase between the 1100 nm and 500 nm bi-layer thickness material when loading along the growth direction from an average 190 MPa from three samples to an average 300 MPa from four samples, respectively. The yield stress of the 2200 nm material was 150 MPa. Despite the bi-layer thickness decreasing by half between the two steps, there was only an increase of 27% when going from 2200 nm to 1100 nm compared to an increase of 58% when going from 1100 nm to 500 nm. The key difference is the proportion of cube-on-cube and incoherent twin interfaces. The 2200 nm and 1100 nm bi-layer thickness materials have 0% and 15% by area with incoherent twin interfaces while the 500 nm bi-layer thickness material has 66% or greater. It was discussed in the previous section that geometry of the interfaces and slip systems has an impact on the barrier strength of an interface a dislocation encounters. Incoherent twin interfaces have a geometry that has limited pathways of easy strain transfer across the interfaces, limited to perfect dislocations on the twin plane. Cube-on-cube interfaces on the other hand have a geometry that has many pathways to easy strain transfer because all of the slip systems of both Ag and Cu are nearly perfectly aligned. This suggests the interface type plays a role in determining the bulk mechanical properties.

The orientation of the interfaces with respect to the load also significantly impacts the yield stress with loading 0°, 90°, and 45° to the growth direction listed in order of highest to lowest yield strength for each bi-layer thickness. These load orientation will activate different slip systems. In terms of loading 0° to the [101] growth direction, four slip systems are predicted to be activated, and the other eight slip systems have no resolved shear stress on them according to Schmid factor

analysis. The activated systems include on the (111) plane $\frac{a}{2}[0\bar{1}1]$ and $\frac{a}{2}[1\bar{1}0]$; and on the $(\bar{1}1\bar{1})$ plane $\frac{a}{2}[\bar{1}\bar{1}0]$ and $\frac{a}{2}[0\bar{1}\bar{1}]$. These slip systems have relatively short mean free paths of slip between interfaces which hinder dislocation slip, explaining why this load orientation exhibited the highest yield strength.

Schmid factor analysis for loading 45° and 90° to the growth direction is more complicated because the colonies of Ag and Cu globular platelets or lamellae are rotated about the growth direction. Instead of one set of active slip systems, it is a distribution. In the case of loading 45° to the growth direction, dislocations $\frac{b}{2}[101]$ on either $(1\bar{1}\bar{1})$ or $(\bar{1}\bar{1}1)$ will be primarily active for most colony orientations. These dislocations have a large mean free path of slip before encountering an interfaces because the slip is parallel to the interfaces. For this reason, loading 45° to the growth direction is the weakest orientation. Loading 90° results in a mix of slip with large and short mean free paths and is the intermediate strength orientation.

5.6 Inelastic recovery

To determine the mechanism for the plastic strain recovery observed in the 500 nm bi-layer material loading parallel to the growth direction, a collaboration with molecular dynamics computer simulation experts, Mr. Ao Li and Professor Szlufarska at Univeristy of Wisconsin-Madison was established; this work is being prepared for publication [134]. Although the specific interactions studied in the simulations could not be verified, there was a unique experimental signature to these deformations that could be used as a means to validate the simulations. It was found that the orientation relationship between Ag and Cu changed following mechanical testing which is summarized in Table 4.2. The change in orientation relationship was also found in the

simulations suggesting that despite the differences, the simulations could be used to yield insight to the physical mechanisms.

From MD simulations, it was found that the mechanisms for plastic strain recovery were based on back motion of dislocations and annihilation of dislocation content in the interfaces. The degree of plastic recovery decreased with increasing levels of strain. This was attributed to the increasing complexity of the dislocation structures formed with increasing strain. These mechanisms are dependent on the load orientation activating slip systems that result in changes to the interface structure. Those changes increase the energy of the interfaces, providing a driving force for dislocation back motion.

Changes to the interface structure, orientation relationship to be specific, are believed to drive the back motion of dislocations. Plastic strain recovery occurred for loading along the $[101]_{\mathrm{Ag}}$ and $[110]_{\mathrm{Cu}}$ growth direction. Anisotropic deformation occurs when loading single crystal Ag and Cu layers along those directions according to MD simulations showing preferential elongation in $[0\bar{1}0]_{\mathrm{Ag}}$ and $[00\bar{1}]_{\mathrm{Cu}}$ [130]. The behavior is also captured in AgCu multilayered simulations with incoherent twin interfaces and matches the change in interfaces observed experimentally. Table 5.7 compares the change in orientation relationship for both experimental observations and simulations at various loading conditions. Only the specimens with primarily incoherent twin interfaces loaded along $[101]_{\mathrm{Ag}}$ and $[110]_{\mathrm{Cu}}$ quasi-statically or to strains greater than 21.2% did not exhibit plastic strain recovery, despite showing the change in orientation relationship of the interface. When the original orientation relationship between the Ag and Cu layers is cube-on-cube and both phases are loaded along the [101] direction, Ag and Cu retain their original orientation relationship.

Table 5.7: Loading conditions and change in orientation relationship.

Test method, Strain (%), and load orientation with respect to the growth direction	Range of rotation away from the twin orientation relationship (average value)	Test method, Strain (%), and load orientation with respect to the growth direction	Range of rotation away from the twin orientation relationship (average value)
Undeformed material	0.7° to 2.4° (1.7°)	MD Undeformed	2.7° to 2.9° (2.8°)
SPHB, 9.5%, 0°	5.9° and 9.8° (7.6°)	MD, 10%, 0°	5.5° to 7.2° (6.2°)
		MD, 10% and 500 ns recovery, 0°	4.2° to 6.0° (5.1°)
SHPB, 23.5%, 0°	5.3° and 14.0° (10.3°)	MD, 25%, 0°	(10.5°)
		MD, 25% and 500 ns recovery, 0°	(10.4°)
SHPB, 15.4%, 90°	0.0° to 5.2° (1.8°)	MD, 10%, 90°	(2.6°)
Quasi-static, 4%, 0°	(6.3°)		

The driving force for the back motion of the dislocations causing plastic strain recovery is presumed to arise from contributions of the buildup of dislocation content at the interface and the increased energy from the change in orientation relationship between Ag and Cu. The change in interfacial structure and misorientation can be further interpreted from the perspective of energy. Local potential energy is plotted in Figs. 5.7(a)-(c) for the cases of (a) incoherent twin interfaces with the load $[101]_{\mathrm{Ag}}$ and $[110]_{\mathrm{Cu}}$, (b) incoherent twin interfaces with load direction 90° away from $[101]_{\mathrm{Ag}}$ and $[110]_{\mathrm{Cu}}$, and (c) cube-on-cube interfaces with loading along the $[101]_{\mathrm{Ag,Cu}}$. To calculate the local potential energy, the system is first divided into 4Å-thick slices parallel to Ag/Cu interfaces, and then the potential energy of all of the atoms in each slice is averaged. For nanolayers with incoherent twin interfaces, before compression (0% strain), energy at the interface region is slightly higher than the energy in the Ag layer by 0.0024eV. The energy in the Ag layer is close to the average potential energy per atom of single crystal Ag (-2.812eV). After the samples are

compressed to a strain of 10% with the load along $[101]_{\mathrm{Ag}}$ and $[110]_{Cu}$, the interfacial energy increases to -2.7968eV and the energy of the inner layers increases to -2.8082eV. After recovery, the interfacial energy decreases to -2.8000eV and energy of inner layers decreases to -2.8091eV. The decrease in energy at the interfaces is more significant than the decrease of energy inside the layers, Fig. 5.7(a).

After the nanolayers with incoherent twin interfaces are compressed to a strain of 10% with the load direction 90° away from $[101]_{\mathrm{Ag}}$ and $[110]_{\mathrm{Cu}}$, the interfacial energy increases to -2.7976eV and the energy of inner layers increases to -2.8096eV, Fig. 5.7(b). After recovery, the interfacial energy decreases to -2.8049eV and the energy of inner layers decreases to -2.8107eV. The decrease in energy at the interfaces is also higher than the decrease of energy inside layers, though the difference is not as significant as the previous case.

For nanolayers with cube-on-cube interfaces, before compression (0% strain), the average energy in the interface region and the average energy inside layers are the same, equaling -2.812eV. The energy is distributed more evenly than that of nanolayers with incoherent twin interfaces. After the samples are compressed to a strain of 10%, the interfacial energy increases to -2.7986eV and the energy of inner layers increases to -2.8021eV. After recovery, the interfacial energy decreases to -2.8035eV and the energy of the inner layers decreases to -2.8051eV, Fig. 5.7(c). Again the energy decrease at the interfaces is greater than the layer interiors, and not as significant as when loading the nanolayers with incoherent twin interfaces along $[101]_{Ag}$ and $[110]_{Cu}$.

A distinction between the case with plastic strain recovery, Fig. 5.7(a), to the two cases without plastic strain recovery, Figs. 5.7(b) and (c), can be made based on the ratio of energy change

between the interface and layer interior regions, Fig. 5.7(d). For all three cases the ratios are larger than 1, which means the energy change in the interface region is more significant than the layer interiors. This ratio, however, is much higher for the case with plastic strain recovery. The difference is related to the active slip systems. Loading along the growth direction for the incoherent twin interfaces activates dislocations that are blocked by the interfaces and also causes a change in orientation relationship, loading 90° to the growth direction when the interfaces are incoherent twins activates dislocations that can transfer across the interfaces and additionally the orientation relationship between Ag and Cu does not change. The cube-on-cube interfaces loaded along the growth direction retain their original orientation relationship and allow transfer of some of the dislocations as well. The retention of the initial orientation relationship results in a smaller residual stress to cause the direction of dislocation motion to reverse. This means incoherent twin interfaces with the load along $[101]_{\mathrm{Ag}}$ and $[110]_{\mathrm{Cu}}$ are more effective in decreasing dislocation density in the interface region after unloading causing plastic strain recovery, and corresponding to a bigger ratio of energy change between peak loading and recovery. While similar to the back motion of dislocations for plastic strain recovery cited in the penta-twinned Ag nano-wires, the AgCu eutectic, however, appears to require a change to the interface structure to drive this plastic recovery [110].

The MD simulations do not offer any explanation as to why quasi-statically deformed specimens with primarily incoherent twin interfaces compressed along $[101]_{\mathrm{Ag}}$ and $[110]_{\mathrm{Cu}}$ do not exhibit plastic strain recovery. However, by comparing the evolved deformation microstructures of the quasi-statically and dynamically deformed specimens, the formation of dislocation structures appear to inhibit plastic strain recovery. The quasi-statically deformed sample and the sample strained to 21.5% both exhibited dislocation cell structures and dislocation

tangles and neither exhibited plastic strain recovery. In these cases, the dislocation-dislocation interactions lock the structures and inhibit dislocation motion and hence the plastic strain recovery.

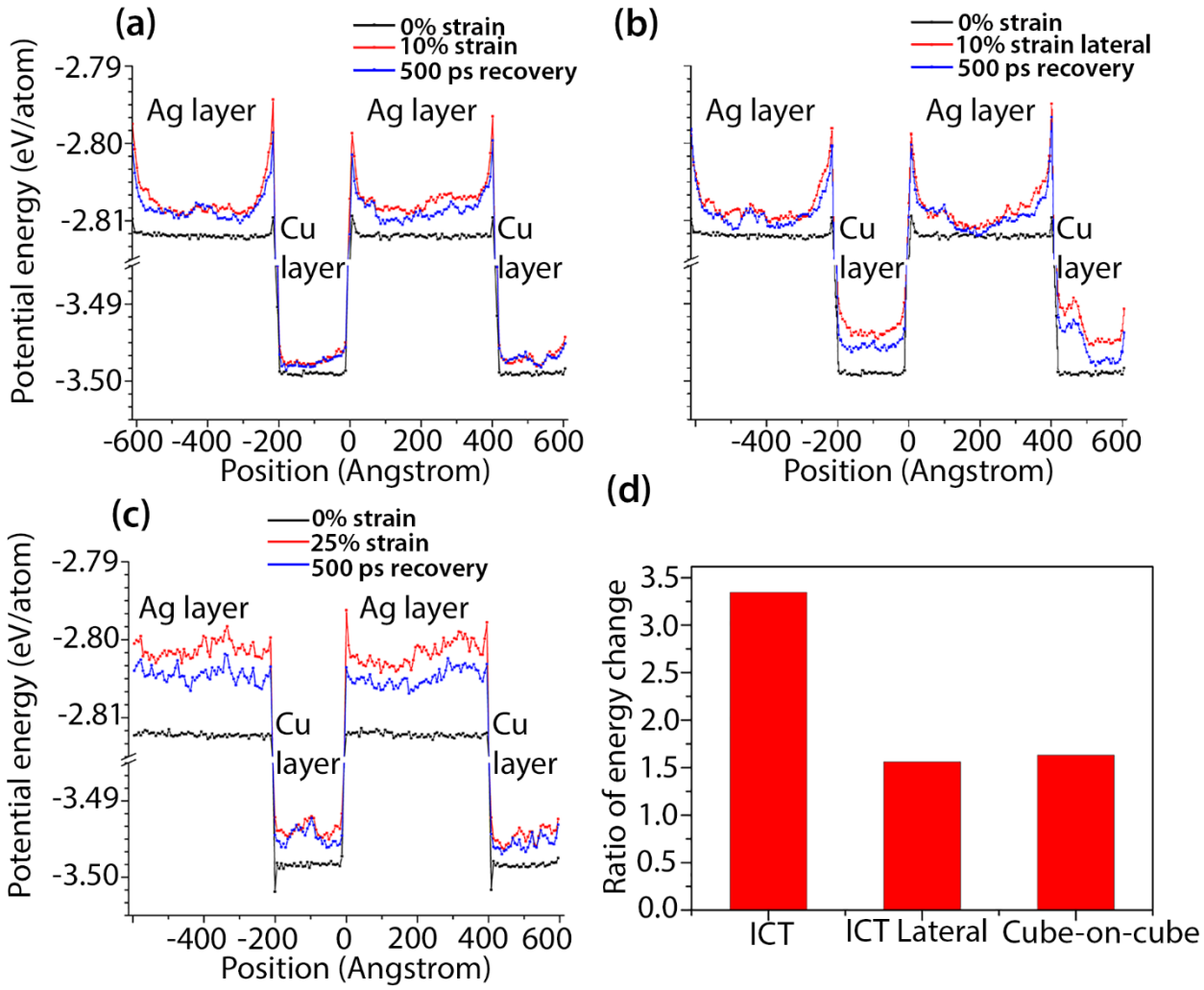

Figure 5.7: (a) Potential energy in different positions normal to incoherent twin interfaces before, at the peak of loading at 10% strain along $[101]_{Ag}$ and $[110]_{Cu}$, and 500 ps after unloading. (b) Potential energy in different positions normal to incoherent twin interfaces before, at the peak of loading at 10% strain 90° to $[101]_{Ag}$ and $[110]_{Cu}$, and 500 ps after unloading. (c) Potential energy in different positions normal to cube-on-cube interfaces along $[101]_{Ag,Cu}$ before, at the peak of loading at 10% strain along $[101]_{Ag}$ and $[110]_{Cu}$, and 500 ps after unloading. (d) The ratio of energy change between the interface and layer interior regions [134].

CHAPTER 6

CONCLUSION

The dislocation/interface interactions in a AgCu eutectic were investigated in this study. To compare to previously proposed models for both single phase and multiphase materials, both *in situ* and *ex situ* TEM straining experiments were performed. Key questions were

1. Is twinning in Cu driven by twinning in Ag and what conditions does Cu twin in the Ag/Cu composite system?
2. Are the dislocation/interface interactions for the different interface types in the Ag/Cu composite comparable to the slip transfer criteria proposed for single phase dislocation/grain boundary interactions?
3. Can interface type and interface orientation with respect to the load direction be related to mechanical strength?

Deformation twinning in Cu was found at length-scales between 50 nm and several microns, and strains as low as 4% for bulk samples strained in compression at 10^3 s^{-1}. The determining factor was a source of twinning partial dislocations provided by Ag that were able to transmit across the Ag/Cu interfaces. This requires i) twinning partials in Ag and ii) cube-on-cube Ag/Cu interfaces. Transmission of twinning partial dislocations across the Ag/Cu interfaces proposed by Wang *et al.* was confirmed including the rotation of the interface by the event [28].

For dislocations interacting with the different interface types, the residual dislocation left at the interface had to be small for communication across the interface. This criterion was found to be determining to the point where deformation twinning could be driven in Cu under conditions it otherwise would not. With larger $|b_{res}|$, dislocation slip was effectively blocked by the interface. For example partial dislocations in Ag on the shared plane are blocked by the incoherent twin

interfaces which would require a $|b_{res}|$ = 1.30 Å to communicate across, while perfect dislocations in Ag on the shared plane communicate across with a $|b_{res}|$ = 0.34 Å. Even though both the partial and the perfect dislocations are on the slip plane that is continuous across the interface.

In addition to layer thickness, interface type and interface orientation with respect to the load were found to impact the mechanical strength of the bulk material. There was a significant increase in yield strength associated with the incoherent twin interfaces. Decreasing the layer thickness from 2200 nm to 1100 nm resulted in a yield strength increase of 27% compared to an increase of 58% from 1100 nm to 500 nm despite the difference in length-scale of both being approximately a factor of 2. The difference is the interface type is predominantly, greater than 66%, incoherent twin in the 500 nm material while the 1100 nm and 2200 nm bi-layer thickness material have mostly cube-on-cube interfaces, 0% and 15% incoherent twin respectively. The relative barrier strengths of the cube-on-cube and incoherent twin interfaces is related to the $|b_{res}|$ for the different slip systems to communicate across the interfaces, indicating that the incoherent twin interfaces are stronger barriers to dislocations which matches the increase in yield strength associated with them. Loading the directionally solidified material at different orientations with respect to the interfaces was associated with differences in yield strength which was attributed to the relative mean free paths of dislocations to encountering interfaces. Activated slip systems were predicted by Schmid factor analysis indicating load orientations with slip systems with relatively short mean free paths to interfaces had a higher yield strength.

REFERENCES

[1] A. Balyanov, J. Kutnyakova, N.A. Amirkhanova, V.V. Stolyarov, R.Z. Valiev, X.Z. Liao, Y.H. Zhao, Y.B. Jiang, H.F. Xu, T.C. Lowe, Y.T. Zhu. Corrosion resistance of ultra fine-grained Ti, Scripta Materialia 51 (2004) 225-229.

[2] P.Q. La, J.Q. Ma, Y.T. Zhu, J. Yang, W.M. Lu, Q.J. Xue, R.Z. Valiev. Dry-sliding tribological properties of ultrafine-grained Ti prepared by severe plastic deformation, Acta Materialia 53 (2005) 5167-5173.

[3] J.T. Wood, J.D. Embury, M.F. Ashby. An approach to materials processing and selection for high-field magnet design, Acta Materialia 45 (1997) 1099-1104.

[4] T. Hochbauer, A. Misra, K. Hattar, R.G. Hoagland. Influence of interfaces on the storage of ion-implanted He in multilayered metallic composites, Journal of Applied Physics 98 (2005) 1-7.

[5] K. Hattar, M.J. Demkowicz, A. Misra, I.M. Robertson, R.G. Hoagland. Arrest of He bubble growth in Cu-Nb multilayer nanocomposites, Scripta Materialia 58 (2008) 541-544.

[6] M.A. Meyers, A. Mishra, D.J. Benson. Mechanical properties of nanocrystalline materials, Prog. Mater. Sci. 51 (2006) 427-556.

[7] J.P. Hirth. Influence of grain-boundaries on mechanical properties, Metallurgical Transactions 3 (1972) 3047-3067.

[8] Y. Liu, D. Bufford, H. Wang, C. Sun, X. Zhang. Mechanical properties of highly textured Cu/Ni multilayers, Acta Materialia 59 (2011) 1924-1933.

[9] T.D. Shen, R.B. Schwarz, X. Zhang. Bulk nanostructured alloys prepared by flux melting and melt solidification, Applied Physics Letters 87 (2005).

[10] Y.Z. Tian, Z.F. Zhang. Bulk eutectic Cu-Ag alloys with abundant twin boundaries, Scripta Materialia 66 (2012) 65-68.

[11] C.J. Davidson, I.O. Smith. Interphase orientation relationships in directionally solidified silver copper eutectic alloy, Materials Science Letters 3 (1984) 759-762.

[12] R.G. Hoagland, R.J. Kurtz, C.H. Henager. Slip resistance of interfaces and the strength of metallic multilayer composites, Scripta Materialia 50 (2004) 775-779.

[13] T.C. Lee, I.M. Robertson, H.K. Birnbaum. TEM in situ deformation study of the interaction of lattice dislocations with grain boundaries in metals, Philosophical Magazine A 62 (1990) 131-153.

[14] H.B. Huang, F. Spaepen. Tensile testing of free-standing Cu, Ag and Al thin films and Ag/Cu multilayers, Acta Materialia 48 (2000) 3261-3269.

[15] M. Verdier, H. Huang, F. Spaepen, J.D. Embury, H. Kung. Microstructure, indentation and work hardening of Cu/Ag multilayers, Philosophical Magazine 86 (2006) 5009-5016.

[16] J. McKeown, A. Misra, H. Kung, R.G. Hoagland, M. Nastasi. Microstructures and strength of nanoscale Cu-Ag multilayers, Scripta Materialia 46 (2002) 593-598.

[17] T.D. Shen, X. Zhang, K. Han, C.A. Davy, D. Aujla, P.N. Kalu, R.B. Schwarz. Structure and properties of bulk nanostructured alloys synthesized by flux-melting, Journal of Materials Science 42 (2007) 1638-1648.

[18] H.E. Cline, D.F. Stein. Strengthening by Interfaces in Ag-Cu Directionally Solidified Eutectic, Transactions of the Metallurgical Society of AIME 245 (1969) 841-&.

[19] S. Brittman, A.J. Smith, S. Milenkovic, A.W. Hassel. Copper nanowires and silver micropit arrays from the electrochemical treatment of a directionally solidified silver-copper eutectic, Electrochim. Acta 53 (2007) 324-329.

[20] L. Ghalandari, M.M. Moshksar. High-strength and high-conductive Cu/Ag multilayer produced by ARB, Journal of Alloys and Compounds 506 (2010) 172-178.
[21] G. Frommeyer, G. Wassermann. Microstructure and anomalous mechanical properties of in situ-produced silver-copper composite wires, Acta Metallurgica 23 (1975) 1353-1360.
[22] Y. Sakai, K. Inoue, T. Asano, H. Maeda. Development of a high strength, high conductivity copper-silver alloy for pulsed magnets, IEEE Transactions on Magnetics 28 (1992) 888-891.
[23] K. Han, J.D. Embury, J.R. Sims, L.J. Campbell, H.J. Schneider-Muntau, V.I. Pantsyrnyi, A. Shikov, A. Nikulin, A. Vorobieva. The fabrication, properties and microstructure of Cu-Ag and Cu-Nb composite conductors, Materials Science and Engineering A 267 (1999) 99-114.
[24] K. Han, J.D. Embury, J.J. Petrovic, G.C. Weatherly. Microstructural aspects of Cu-Ag produced by the Taylor wire method, Acta Materialia 46 (1998) 4691-4699.
[25] K. Han, J.P. Hirth, J.D. Embury. Modeling the formation of twins and stacking faults in the Ag-Cu system, Acta Materialia 49 (2001) 1537-1540.
[26] S. Zghal, M.J. Hÿtch, J.P. Chevalier, R. Twesten, F. Wu, P. Bellon. Electron microscopy nanoscale characterization of ball-milled Cu–Ag powders. Part I: Solid solution synthesized by cryo-milling, Acta Materialia 50 (2002) 4695-4709.
[27] F. Wu, D. Isheim, P. Bellon, D.N. Seidman. Nanocomposites stabilized by elevated-temperature ball milling of Ag 50 Cu 50 powders: An atom probe tomographic study, Acta Mater. 54 (2006) 2605-2613.
[28] J. Wang, I.J. Beyerlein, N.A. Mara, D. Bhattacharyya. Interface-facilitated deformation twinning in copper within submicron Ag-Cu multilayered composites, Scripta Materialia 64 (2011) 1083-1086.
[29] B.P. Eftink, N.A. Mara, O.T. Kingstedt, D.J. Safarik, J. Lambros, I.M. Robertson. Anomalous deformation twinning in coarse-grained Cu in Ag60Cu40 composites under high strain-rate compressive loading, Materials Science and Engineering: A 618 (2014) 254-261.
[30] I.J. Beyerlein, N.A. Mara, D. Bhattacharyya, D.J. Alexander, C.T. Necker. Texture evolution via combined slip and deformation twinning in rolled silver-copper cast eutectic nanocomposite, International Journal of Plasticity 27 (2011) 121-146.
[31] A. Howie, P.R. Swann. Direct measurements of stacking-fault energies from observations of dislocation nodes, Philosophical Magazine 6 (1961) 1215-1226.
[32] W. Li, S. Lu, Q.M. Hu, S.K. Kwon, B. Johansson, L. Vitos. Generalized stacking fault energies of alloys, J. Phys.-Condes. Matter 26 (2014).
[33] T.D. Shen, R.B. Schwarz, X. Zhang. Bulk nanostructured alloys prepared by flux melting and melt solidification, Appl. Phys. Lett. 87 (2005) 1-3.
[34] J.D. Hunt, K.A. Jackson. Binary eutectic solidification, Transactions of the Metallurgical Society of Aime 236 (1966) 843-&.
[35] G. Frommeyer, G. Wassermann. Microstructure and anomalous mechanical-properties of insitu-produced silver-copper composite wires, Acta Metallurgica 23 (1975) 1353-1360.
[36] H.E. Cline, D. Lee. Strengthening of Lamellar vs Equiaxed Ag-Cu Eutectic, Acta Metallurgica 18 (1970) 315-&.
[37] D. Kuhlmann-Wilsdorf. The theory of dislocation-based crystal plasticity, Philos. Mag. A-Phys. Condens. Matter Struct. Defect Mech. Prop. 79 (1999) 955-1008.
[38] B. Bay, N. Hansen, D.A. Hughes, D. Kuhlmannwilsdorf. Evolution of FCC deformation structures in polyslip, Acta metallurgica et materialia 40 (1992) 205-219.

[39] D.A. Hughes, N. Hansen, D.J. Bammann. Geometrically necessary boundaries, incidental dislocation boundaries and geometrically necessary dislocations, Scripta Materialia 48 (2003) 147-153.
[40] S. Asgari, E. ElDanaf, S.R. Kalidindi, R.D. Doherty. Strain hardening regimes and microstructural evolution during large strain compression of low stacking fault energy fcc alloys that form deformation twins, Metall. Mater. Trans. A-Phys. Metall. Mater. Sci. 28 (1997) 1781-1795.
[41] L. Remy. Kinetics of f.c.c. deformation twinning and its relationship to stress-strain behaviour, Acta Metallurgica 26 (1978) 443-451.
[42] H. Suzuki, C.S. Barrett. Deformation twinning in silver-gold alloys, Acta Metallurgica 6 (1958) 156-165.
[43] E.B. Tadmor, N. Bernstein. A first-principles measure for the twinnability of FCC metals, Journal of the Mechanics and Physics of Solids 52 (2004) 2507-2519.
[44] E. El-Danaf, S.R. Kalidindi, R.D. Doherty. Influence of grain size and stacking-fault energy on deformation twinning in fcc metals, Metall. Mater. Trans. A-Phys. Metall. Mater. Sci. 30 (1999) 1223-1233.
[45] M.A. Meyers, U.R. Andrade, A.H. Chokshi. The Effect of Grain-Size on the High-Strain, High-Strain-Rate Behavior of Copper, Metall. Mater. Trans. A-Phys. Metall. Mater. Sci. 26 (1995) 2881-2893.
[46] M.A. Meyers, O. Vohringer, V.A. Lubarda. The onset of twinning in metals: A constitutive description, Acta Materialia 49 (2001) 4025-4039.
[47] M. Niewczas, G. Saada. Twinning nucleation in Cu-8 at.% Al single crystals, Philos. Mag. A-Phys. Condens. Matter Struct. Defect Mech. Prop. 82 (2002) 167-191.
[48] F. Cao, I.J. Beyerlein, F.L. Addessio, B.H. Sencer, C.P. Trujillo, E.K. Cerreta, G.T. Gray. Orientation dependence of shock-induced twinning and substructures in a copper bicrystal, Acta Materialia 58 (2010) 549-559.
[49] J.W. Christian, S. Mahajan. Deformation twinning, Prog. Mater. Sci. 39 (1995) 1-157.
[50] B. Cao, N.P. Daphalapurkar, K.T. Ramesh. Ultra-high-strain-rate shearing and deformation twinning in nanocrystalline aluminum, Meccanica 50 (2015) 561-574.
[51] G.T. Gray, P.S. Follansbee, C.E. Frantz. Effect of residual strain on the substructure developement and mechanical response of shock-loaded copper, Mater. Sci. Eng. A-Struct. Mater. Prop. Microstruct. Process. 111 (1989) 9-16.
[52] J.C. Sanchez, L.E. Murr, K.P. Staudhammer. Effect of grain size and pressure on twinning and microbanding in oblique shock loading of copper rods, Acta Materialia 45 (1997) 3223-3235.
[53] A. Kauffmann, J. Freudenberger, D. Geissler, S. Yin, W. Schillinger, V.S. Sarma, H. Bahmanpour, R. Scattergood, M.S. Khoshkhoo, H. Wendrock, C.C. Koch, J. Eckert, L. Schultz. Severe deformation twinning in pure copper by cryogenic wire drawing, Acta Materialia 59 (2011) 7816-7823.
[54] J.Y. Zhang, G. Liu, R.H. Wang, J. Li, J. Sun, E. Ma. Double-inverse grain size dependence of deformation twinning in nanocrystalline Cu, Phys. Rev. B 81 (2010).
[55] P. Haasen. Plastic deformation of nickel single crystals at low temperatures, Philosophical Magazine 3 (1958) 384-418.
[56] L.S. Palatnik, A.I. Ii'inskii. Stabilization of High-Strength Vacuum-Deposited Films, Soviet Physics-Doklady 9 (1964) 2.
[57] L.S. Palatnik, A.I. Ii'inskii, N.P. Sapelkin. Strength of Multilayered Vacuum Condensates, Soviet Physics-Solid State 8 (1967) 2.

[58] A. Misra, M. Verdier, Y.C. Lu, H. Kung, T.E. Mitchell, N. Nastasi, J.D. Embury. Structure and mechanical properties of Cu-X (X = Nb,Cr,Ni) nanolayered composites, Scripta Materialia 39 (1998) 555-560.
[59] W. D. Nix. Elastic and plastic properties of thin films on substrates: nanoindentation techniques, Materials Science & Engineering A 234 (1997) 37-44.
[60] T.E. Mitchell, Y.C. Lu, A.J. Griffin, M. Nastasi, H. Kung. Structure and mechanical properties of copper/niobium multilayers, Journal of the American Ceramic Society 80 (1997) 1673-1676.
[61] S.L. Lehoczky. Retardation of dislocation generation and motion in thin-layered metal laminates, Physical Review Letters 41 (1978) 1814-1818.
[62] G.S. Was, T. Foecke. Deformation and fracture in microlaminates, Thin Solid Films 286 (1996) 1-31.
[63] A.H. Chokshi, A. Rosen, J. Karch, H. Gleiter. On the validity of the Hall-Petch relationship in nanocrystalline materials, Scripta Metallurgica 23 (1989) 1679-1683.
[64] A. Misra, J.P. Hirth, H. Kung. Single-dislocation-based strengthening mechanisms in nanoscale metallic multilayers, Philosophical Magazine A: Physics of Condensed Matter, Structure, Defects and Mechanical Properties 82 (2002) 2935-2951.
[65] J.D. Embury, J.P. Hirth. On dislocation storage and the mechanical response of fine-scale microstructures, Acta metallurgica et materialia 42 (1994) 2051-2056.
[66] P.M. Anderson, T. Foecke, P.M. Hazzledine. Dislocation-based deformation mechanisms in metallic nanolaminates, Mrs Bulletin 24 (1999) 27-33.
[67] A. Misra, R.G. Hoagland. Plastic flow stability of metallic nanolaminate composites, Journal of Materials Science 42 (2007) 1765-1771.
[68] R.O. Scattergood, C.C. Koch. A modified-model for Hall-Petch behavior in nanocrystalline materials, Scr. Metall. Materialia 27 (1992) 1195-1200.
[69] C.H. Henager, R.J. Kurtz, R.G. Hoagland. Interactions of dislocations with disconnections in fcc metallic nanolayered materials, Philosophical Magazine 84 (2004) 2277-2303.
[70] A. Misra, J.P. Hirth, H. Kung. Single-dislocation-based strengthening mechanisms in nanoscale metallic multilayers, Philos. Mag. A-Phys. Condens. Matter Struct. Defect Mech. Prop. 82 (2002) 2935-2951.
[71] R.G. Hoagland, T.E. Mitchell, J.P. Hirth, H. Kung. On the strengthening effects of interfaces in multilayer fcc metallic composites, Philos. Mag. A-Phys. Condens. Matter Struct. Defect Mech. Prop. 82 (2002) 643-664.
[72] J. Wang, A. Misra, R.G. Hoagland, J.P. Hirth. Slip transmission across fcc/bcc interfaces with varying interface shear strengths, Acta Materialia 60 (2012) 1503-1513.
[73] Y.Z. Tian, Z.F. Zhang. Stability of interfaces in a multilayered Ag-Cu composite during cold rolling, Scripta Materialia 68 (2013) 542-545.
[74] O.T. Kingstedt, B. Eftink, J. Lambros, I.M. Robertson. Quasi-static and dynamic compressive deformation of a bulk nanolayered Ag-Cu eutectic alloy: Macroscopic response and dominant deformation mechanisms, Mater. Sci. Eng. A-Struct. Mater. Prop. Microstruct. Process. 595 (2014) 54-63.
[75] W.Z. Han, J.S. Carpenter, J. Wang, I.J. Beyerlein, N.A. Mara. Atomic-level study of twin nucleation from face-centered-cubic/body-centered-cubic interfaces in nanolamellar composites, Applied Physics Letters 100 (2012).

[76] X.H. An, S.M. Zhu, Y. Cao, M. Kawasaki, X.Z. Liao, S.P. Ringer, J.F. Nie, T.G. Langdon, Y.T. Zhu. Atomic-scale investigation of interface-facilitated deformation twinning in severely deformed Ag-Cu nanolamellar composites, Applied Physics Letters 107 (2015).
[77] J.S. Carpenter, X. Liu, A. Darbal, N.T. Nuhfer, R.J. McCabe, S.C. Vogel, J.E. LeDonne, A.D. Rollett, K. Barmak, I.J. Beyerlein, N.A. Mara. A comparison of texture results obtained using precession electron diffraction and neutron diffraction methods at diminishing length scales in ordered bimetallic nanolamellar composites, Scr. Mater. 67 (2012) 336-339.
[78] J. Kacher, B.P. Eftink, B. Cui, I.M. Robertson. Dislocation interactions with grain boundaries, Curr. Opin. Solid State Mat. Sci. 18 (2014) 227-243.
[79] J.D. Livingston, B. Chalmers. Multiple slip in bicrystal deformation, Acta Metallurgica 5 (1957) 322-327.
[80] Z. Shen, R.H. Wagoner, W.A.T. Clark. Dislocation and Grain-Boundary Interactions in Metals, Acta Metallurgica 36 (1988) 3231-3242.
[81] Z. Shen, R.H. Wagoner, W.A.T. Clark. Dislocation pile up and grain-boundary interactions in 304 stainless-steel, Scripta Metallurgica 20 (1986) 921-926.
[82] T.C. Lee, I.M. Robertson, H.K. Birnbaum. Prediction of slip transfer mechanisms across grain-boundaries, Scripta Metallurgica 23 (1989) 799-803.
[83] M.A. Morris, J. Luster. Effect of rotation relationship between gamma grains on compatability of deformation in Ti-Al alloys. in: Horton J, Baker I, Hanada S, Noebe RD, Schwartz DS, (Eds.). High-Temperature Ordered Intermetallic Alloys Vi, Pts 1 and 2, vol. 364. Materials Research Soc, Pittsburgh, 1995. pp. 593-598.
[84] J. Luster, M.A. Morris. Compatibility of deformation in two-phase Ti-Al alloys: Dependence on microstructure and orientation relationships, Metallurgical and Materials Transactions A 26 (1995) 1745-1756.
[85] I.J. Beyerlein, J. Wang, K. Kang, S.J. Zheng, N.A. Mara. Twinnability of bimetal interfaces in nanostructured composites, Materials Research Letters 1 (2013) 89-95.
[86] J. Kacher, I.M. Robertson. Quasi-four-dimensional analysis of dislocation interactions with grain boundaries in 304 stainless steel, Acta Materialia 60 (2012) 6657-6672.
[87] T.C. Lee, I.M. Robertson, H.K. Birnbaum. An In Situ transmission electron microscope deformation study of the slip transfer mechanisms in metals, Metallurgical Transactions A 21 (1990) 2437-2447.
[88] A. Misra, R. Gibala. Slip transfer and dislocation nucleation processes in multiphase ordered Ni-Fe-Al alloys, Metall. Mater. Trans. A-Phys. Metall. Mater. Sci. 30 (1999) 991-1001.
[89] J. Kacher, I.M. Robertson. In situ and tomographic analysis of dislocation/grain boundary interactions in alpha-titanium, Philosophical Magazine 94 (2014) 814-829.
[90] T. Kehagias, P. Komninou, G.P. Dimitrakopulos, J.G. Antonopoulos, T. Karakostas. Slip transfer across low-angle grain-boundaries of deformed titanium, Scr. Metall. Materialia 33 (1995) 1883-1888.
[91] A. Gemperle, J. Gemperlova, N. Zarubova. Interaction of slip dislocations with grain boundaries in body-centered cubic bicrystals, Mater. Sci. Eng. A-Struct. Mater. Prop. Microstruct. Process. 387 (2004) 46-50.
[92] J. Gemperlova, A. Jacques, A. Gemperle, T. Vystavel, N. Zarubova, M. Janecek. In-situ transmission electron microscopy observation of slip propagation in Sigma 3 bicrystals, Mater. Sci. Eng. A-Struct. Mater. Prop. Microstruct. Process. 324 (2002) 183-189.

[93] M. Dewald, W.A. Curtin. Multiscale modeling of dislocation/grain-boundary interactions: III. 60 degrees dislocations impinging on Sigma 3, Sigma 9 and Sigma 11 tilt boundaries in Al, Model. Simul. Mater. Sci. Eng. 19 (2011).
[94] D.V. Bachurin, D. Weygand, P. Gumbsch. Dislocation-grain boundary interaction in < 1 1 1 > textured thin metal films, Acta Materialia 58 (2010) 5232-5241.
[95] M.D. Sangid, T. Ezaz, H. Sehitoglu, I.M. Robertson. Energy of slip transmission and nucleation at grain boundaries, Acta Materialia 59 (2011) 283-296.
[96] G.J. Tucker, D.L. McDowell. Non-equilibrium grain boundary structure and inelastic deformation using atomistic simulations, International Journal of Plasticity 27 (2011) 841-857.
[97] Z.H. Jin, P. Gumbsch, E. Ma, K. Albe, K. Lu, H. Hahn, H. Gleiter. The interaction mechanism of screw dislocations with coherent twin boundaries in different face-centred cubic metals, Scripta Materialia 54 (2006) 1163-1168.
[98] N. Li, J. Wang, A. Misra, X. Zhang, J.Y. Huang, J.P. Hirth. Twinning dislocation multiplication at a coherent twin boundary, Acta Materialia 59 (2011) 5989-5996.
[99] J.P. Couzinie, B. Decamps, L. Priester. Interaction of dissociated lattice dislocations with a Sigma=3 grain boundary in copper, International Journal of Plasticity 21 (2005) 759-775.
[100] M.P. Dewald, W.A. Curtin. Multiscale modelling of dislocation/grain boundary interactions. II. Screw dislocations impinging on tilt boundaries in Al, Philosophical Magazine 87 (2007) 4615-4641.
[101] Z.X. Wu, Y.W. Zhang, D.J. Srolovitz. Dislocation-twin interaction mechanisms for ultrahigh strength and ductility in nanotwinned metals, Acta Materialia 57 (2009) 4508-4518.
[102] Z.H. Jin, P. Gumbsch, K. Albe, E. Ma, K. Lu, H. Gleiter, H. Hahn. Interactions between non-screw lattice dislocations and coherent twin boundaries in face-centered cubic metals, Acta Materialia 56 (2008) 1126-1135.
[103] L.L. Li, P. Zhang, Z.J. Zhang, Z.F. Zhang. Intrinsically higher fatigue cracking resistance of the penetrable and movable incoherent twin boundary, Sci Rep 4 (2014).
[104] J.M.K. Wiezorek, X.D. Zhang, W.A.T. Clark, H.L. Fraser. Activation of slip in lamellae of alpha(2)-Ti3Al in TiAl alloys, Philos. Mag. A-Phys. Condens. Matter Struct. Defect Mech. Prop. 78 (1998) 217-238.
[105] A. Godfrey, D. Hu, M.H. Loretto. The role of the a2 phase in the transmission of slip in lamellar TiAl-based alloys, Phil. Mag. A 77 (1998) 287-287.
[106] J.B. Singh, G. Molenat, M. Sundararaman, S. Banerjee, G. Saada, P. Veyssiere, A. Couret. In situ straining investigation of slip transfer across 2 lamellae at room temperature in a lamellar TiAl alloy, Phil. Mag. Lett. 86 (2006) 47-60.
[107] R.Z. Li, H.B. Chew. Deformation twinning and plastic recovery in Cu/Ag nanolayers under uniaxial tensile straining, Philos. Mag. Lett. 94 (2014) 260-268.
[108] J. Rajagopalan, J.H. Han, M.T.A. Saif. Plastic deformation recovery in freestanding nanocrystalline aluminum and gold thin films, Science 315 (2007) 1831-1834.
[109] X.Y. Li, Y.J. Wei, W. Yang, H.J. Gao. Competing grain-boundary- and dislocation-mediated mechanisms in plastic strain recovery in nanocrystalline aluminum, Proc. Natl. Acad. Sci. U. S. A. 106 (2009) 16108-16113.
[110] Q.Q. Qin, S. Yin, G.M. Cheng, X.Y. Li, T.H. Chang, G. Richter, Y. Zhu, H.J. Gao. Recoverable plasticity in penta-twinned metallic nanowires governed by dislocation nucleation and retraction, Nat. Commun. 6 (2015) 1-8.
[111] O.T. Kingstedt, B.P. Eftink, I.M. Robertson, J. Lambros. Inelastic strain recovery of a dynamically deformed unidirectional Ag-Cu eutectic alloy, In Preparation (2016).

[112] X.C. He, H. Wang, H.S. Liu, Z.P. Jin. Thermodynamic description of the Cu–Ag–Zr system, CALPHAD 30 (2006) 367-374.
[113] O.T. Kingstedt, B. Eftink, J. Lambros, I.M. Robertson. Quasi-static and dynamic compressive deformation of a bulk nanolayered Ag–Cu eutectic alloy: Macroscopic response and dominant deformation mechanisms, Materials Science and Engineering: A 595 (2014) 54-63.
[114] O.T. Kingstedt, B.P. Eftink, D.J. Safarik, I.M. Robertson, J. Lambros. Anisotropic Dynamic Compression Response of a Directionally-Cast Silver-Copper Eutectic Alloy, Acta Materialia (2016).
[115] O.T. Kingstedt. Effects of micro- and nano- structure on the deformation response of a Ag60Cu40 lamellar and rod-in-matrix eutectic alloy. Aerospace Engineering, vol. PhD: University of Illinois Urbana-Champaign, 2014.
[116] B.A. Gama. Hopkinson bar experimental technique: A critical review, Applied mechanics reviews 57 (2004) 223-250.
[117] R.D. Field, P.A. Papin. Location specific in situ TEM straining specimens made using FIB, Ultramicroscopy 102 (2004) 23-26.
[118] P.R. Munroe. The application of focused ion beam microscopy in the material sciences, Materials Characterization 60 (2009) 2-13.
[119] J.B. Liu, Y.W. Zeng, L. Meng. Interface structure and energy in Cu-71.8 wt.% Ag, J. Alloy. Compd. 464 (2008) 168-173.
[120] S. Wang. Energy of AgCu interfaces. 2015.
[121] J.B. Singh, G. Molénat, M. Sundararaman, S. Banerjee, G. Saada, P. Veyssière, A. Couret. In situ straining investigation of slip transfer across α 2 lamellae at room temperature in a lamellar TiAl alloy, Philos. Mag. Lett. 86 (2006) 47-60.
[122] K.A. Jackson, J.D. Hunt. Lamellar and rod eutectic growth, Transactions of the Metallurgical Society of Aime 236 (1966) 1129-&.
[123] B.P. Eftink, N.A. Mara, O.T. Kingstedt, D.J. Safarik, J. Lambros, I.M. Robertson. Deformation response of cube-on-cube and incoherent twin interfaces in AgCu eutectic after dynamic loading, In Preparation (2016).
[124] E. Cadirli, D.M. Herlach, T. Volkmann. Characterization of rapidly solidified Ni-Si and Co-Al eutectic alloys in drop tube, J. Non-Cryst. Solids 356 (2010) 461-466.
[125] R. Goetzinger, M. Barth, D.M. Herlach. Mechanism of formation of the anomalous eutectic structure in rapidly solidified Ni-Si, Co-Sb and Ni-Al-Ti alloys, Acta Mater. 46 (1998) 1647-1655.
[126] C.R. Clopet, R.F. Cochrane, A.M. Mullis. Spasmodic growth during the rapid solidification of undercooled Ag-Cu eutectic melts, Appl. Phys. Lett. 102 (2013).
[127] D.A. Porter, K.E. Easterling. Phase Transformations in Metals and Alloys. 2 ed., Chapman & Hall, London, UK, 1997.
[128] R. Elliott. Eutectic Solidification, Elsevier Ltd.
[129] S. Shao. Unpublished results (2014).
[130] A. Li. Unpublished results (2016).
[131] J. Kacher, B. Eftink, B. Cui, I.M. Robertson. Dislocation interactions with grain boundary interactions, Current Opin. Solid State and Mater. Sci. 18 (2014) 227-243.
[132] T.C. Lee, I.M. Robertson, H.K. Birnbaum. In situ transmission electron microscope deformation study of the slip transfer mechanisms in metals, Metallurgical Transactions. A, Physical Metallurgy and Materials Science 21 A (1990) 2437-2447.
[133] L.C. Lim, R. Raj. Interaction between Lattice and Grain-Boundary Dislocations and Their Role in Mechanical-Properties of Interfaces, J. De Phys. 46 (1985) 581-595.

[134] B.P. Eftink, A. Li, I. Szlufarska, I.M. Robertson. Interface Mediated Mechanisms of Plastic Strain Recovery in a AgCu Alloy, In Preparation (2016).

APPENDIX A: PYTHON RESIDUAL DISLOCATION PROGRAM

Python program will calculate the residual Burgers vector, and angle between slip plane normals for all possible dislocation interactions across an interface in FCC crystals. Orientation between the incoming and outgoing crystals must be defined by a rotation of one crystal about an axis, which is prompted in the program.

The output is a text file with columns of data separated by comas. Columns 1-3 define the slip plane of the incoming system, columns 4-6 are Burgers vector of the incoming system (does not show a/2 or a/6 but the calculations do account for this). Columns 7-9 define the outgoing slip plane and columns 10-12 define the outgoing Burgers vector both in the original coordinate system. Column 13 is the angle between the incoming and outgoing slip planes. Columns 14-16 is the Burgers vector (correct in magnitude) by subtracting the incoming dislocation by the outgoing dislocation. Column 17 is the magnitude of that Burgers vector (lattice parameter is considered in the calculation and needs to be changed in lines 74, 75, and 76 if using an interface other than Ag and Cu). Columns 18-20 are the outgoing slip plane in the transformed coordinate system. Columns 21-23 are the outgoing Burgers vector in the transformed coordinate system.

http://www.planetb.ca/syntax-highlight-word was used to place the code in the document.

```
1.  import math
2.  y = [1]
3.  end = y
4.  while True:
5.
6.      opperation = int(input("Type 1 for dislocation reactions across an interface" '\n'
    "?"))
7.
8.
9.      if opperation == 1: # Slip transfer criteria
10.
11.         perfect = [[1,1,1,-1,1,0,-1/2,1/2,0],[1,1,1,1,-1,0,1/2,-1/2,0],[1,1,1,1,0,-
    1,1/2,0,-1/2],[1,1,1,-1,0,1,-1/2,0,1/2],[1,1,1,0,-1,1,0,-1/2,1/2],[1,1,1,0,1,-1,0,1/2,-
    1/2],[-1,-1,1,-1,1,0,-1/2,1/2,0],[-1,-1,1,1,-1,0,1/2,-1/2,0],[-1,-
    1,1,0,1,1,0,1/2,1/2],[-1,-1,1,0,-1,-1,0,-1/2,-1/2],[-1,-1,1,1,0,1,1/2,0,1/2],[-1,-1,1,-
    1,0,-1,-1/2,0,-1/2],[-1,1,-1,1,0,-1,1/2,0,-1/2],[-1,1,-1,-1,0,1,-1/2,0,1/2],[-1,1,-
    1,1,1,0,1/2,1/2,0],[-1,1,-1,-1,-1,0,-1/2,-1/2,0],[-1,1,-1,0,1,1,0,1/2,1/2],[-1,1,-1,0,-
```

```
    1,-1,0,-1/2,-1/2],[1,-1,-1,0,-1,1,0,-1/2,1/2],[1,-1,-1,0,1,-1,0,1/2,-1/2],[1,-1,-
    1,1,0,1,1/2,0,1/2],[1,-1,-1,-1,0,-1,-1/2,0,-1/2],[1,-1,-1,1,1,0,1/2,1/2,0],[1,-1,-1,-
    1,-1,0,-1/2,-1/2,0]]
12.         partial = [[1,1,1,-2,1,1,-2/6,1/6,1/6],[1,1,1,1,1,-2,1/6,1/6,-2/6],[1,1,1,1,-
    2,1,1/6,-2/6,1/6],[-1,-1,1,-1,2,1,-1/6,2/6,1/6],[-1,-1,1,-1,-1,-2,-1/6,-1/6,-2/6],[-1,-
    1,1,2,-1,1,2/6,-1/6,1/6],[-1,1,-1,2,1,-1,2/6,1/6,-1/6],[-1,1,-1,-1,-2,-1,-1/6,-2/6,-
    1/6],[-1,1,-1,-1,1,2,-1/6,1/6,2/6],[1,-1,-1,1,-1,2,1/6,-1/6,2/6],[1,-1,-1,-2,-1,-1,-
    2/6,-1/6,-1/6],[1,-1,-1,1,2,-1,1/6,2/6,-1/6]]
13.
14.         ############################## Rotation of the first crystal to get the second
15.         print("Rotation of the first crystal to get to the second crystal")
16.         rh = int(input("What is the rotation axis h?"))
17.         rk = int(input("What is the rotation axis k?"))
18.         rl = int(input("What is the rotation axis l?"))
19.         theta = int(input("What is the rotation angle in degrees?"))
20.         angle = (theta*2*3.1415926)/360
21.         mag = (rh**2+rk**2+rl**2)**0.5
22.         l = rh/mag
23.         m = rk/mag
24.         n = rl/mag
25.
26.         c = math.cos(angle)
27.         s = math.sin(angle)
28.
29.         a11 = l*l*(1-c) + c
30.         a12 = m*l*(1-c) - n*s
31.         a13 = n*l*(1-c)+m*s
32.         a21 = l*m*(1-c)+n*s
33.         a22 = m*m*(1-c)+c
34.         a23 = n*m*(1-c)-l*s
35.         a31 = l*n*(1-c)-m*s
36.         a32 = m*n*(1-c)+l*s
37.         a33 = n*n*(1-c)+c
38.
39.         twinperfect = [[0,0,0,0,0,0,0,0,0,0,0,0]]
40.         twinpartial = [[0,0,0,0,0,0,0,0,0,0,0,0]]
41.
42.         for j in range(0,len(perfect)):
43.             twinperfect.append([a11*perfect[j][0]+a12*perfect[j][1]+a13*perfect[j][2],a
    21*perfect[j][0]+a22*perfect[j][1]+a23*perfect[j][2],a31*perfect[j][0]+a32*perfect[j][1
    ]+a33*perfect[j][2],a11*perfect[j][3]+a12*perfect[j][4]+a13*perfect[j][5],a21*perfect[j
    ][3]+a22*perfect[j][4]+a23*perfect[j][5],a31*perfect[j][3]+a32*perfect[j][4]+a33*perfec
    t[j][5], a11*perfect[j][6]+a12*perfect[j][7]+a13*perfect[j][8],a21*perfect[j][6]+a22*pe
    rfect[j][7]+a23*perfect[j][8],a31*perfect[j][6]+a32*perfect[j][7]+a33*perfect[j][8], pe
    rfect[j][0], perfect[j][1], perfect[j][2], perfect[j][3], perfect[j][4], perfect[j][5]]
    )
44.         for j in range(0,len(partial)):
45.             twinpartial.append([a11*partial[j][0]+a12*partial[j][1]+a13*partial[j][2],a
    21*partial[j][0]+a22*partial[j][1]+a23*partial[j][2],a31*partial[j][0]+a32*partial[j][1
    ]+a33*partial[j][2],a11*partial[j][3]+a12*partial[j][4]+a13*partial[j][5],a21*partial[j
    ][3]+a22*partial[j][4]+a23*partial[j][5],a31*partial[j][3]+a32*partial[j][4]+a33*partia
    l[j][5], a11*partial[j][6]+a12*partial[j][7]+a13*partial[j][8],a21*partial[j][6]+a22*pa
    rtial[j][7]+a23*partial[j][8],a31*partial[j][6]+a32*partial[j][7]+a33*partial[j][8], pa
    rtial[j][0], partial[j][1], partial[j][2], partial[j][3], partial[j][4], partial[j][5]]
    )
46.
47.         matrix1 = perfect + partial
48.         matrix2 = [[0,0,0,0,0,0,0,0,0,0,0,0,0,0,0]]
49.         for j in range(1, len(twinperfect)):
50.             matrix2.append([twinperfect[j][0], twinperfect[j][1], twinperfect[j][2], tw
    inperfect[j][3], twinperfect[j][4], twinperfect[j][5], twinperfect[j][6], twinperfect[j
```

```
    ][7], twinperfect[j][8], twinperfect[j][9], twinperfect[j][10], twinperfect[j][11], twi
    nperfect[j][12], twinperfect[j][13], twinperfect[j][14]])
51.         for j in range(1, len(twinpartial)):
52.             matrix2.append([twinpartial[j][0], twinpartial[j][1], twinpartial[j][2], tw
    inpartial[j][3], twinpartial[j][4], twinpartial[j][5], twinpartial[j][6], twinpartial[j
    ][7], twinpartial[j][8], twinpartial[j][9], twinpartial[j][10], twinpartial[j][11], twi
    npartial[j][12], twinpartial[j][13], twinpartial[j][14]])
53.
54.         ################ Combine to make all the possibilities
55.         combo = [[0,0,0,0,0,0,0,0,0,0,0,0,0,0,0,0,0,0,0,0,0,0,0,0,0,0,0,0,0,0,0]]
56.         for j in range(0,len(matrix1)):
57.             for i in range(1,len(matrix2)):
58.                 combo.append([matrix1[j][0],matrix1[j][1],matrix1[j][2],matrix1[j][3],m
    atrix1[j][4],matrix1[j][5],matrix1[j][6],matrix1[j][7],matrix1[j][8],matrix2[i][0],matr
    ix2[i][1],matrix2[i][2],matrix2[i][3],matrix2[i][4],matrix2[i][5],matrix2[i][6],matrix2
    [i][7],matrix2[i][8], matrix2[i][9], matrix2[i][10], matrix2[i][11], matrix2[i][12], ma
    trix2[i][13], matrix2[i][14]])
59.
60.         ################ Angle between slip plane normals
61.         planesangle = [0]
62.         for j in range(0,len(combo)):
63.             dot = combo[j][0]*combo[j][9] + combo[j][1]*combo[j][10] + combo[j][2]*comb
    o[j][11]
64.             mag1 = (combo[j][0]**2 + combo[j][1]**2 + combo[j][2]**2)**0.5+.00000000000
    0000000000000000000000000001
65.             mag2 = (combo[j][9]**2 + combo[j][10]**2 + combo[j][11]**2)**0.5+.000000000
    0000000000000000000000000001
66.             x = dot / (mag1*mag2)
67.             thetaplanes = math.acos(round(dot/(mag1*mag2),14))
68.             angleplanes = round(thetaplanes*360 / (2*3.14159265359), 5)
69.             planesangle.append([angleplanes])
70.
71.         ################ Residual left at the interface
72.         residual = [[0,0,0,0]]  ### residual left in h k and l in the first three, then
     the magnitude in the last column
73.         for j in range(0,len(combo)):
74.             resh = combo[j][6]*4.09-combo[j][15]*3.61 # in minus out
75.             resk = combo[j][7]*4.09-combo[j][16]*3.61
76.             resl = combo[j][8]*4.09-combo[j][17]*3.61
77.             magres = (resh**2+resk**2+resl**2)**0.5
78.             residual.append([resh,resk,resl,magres])
79.
80.
81.         fo = open("STCraw.txt", "w")
82.         for j in range(0,len(combo)):
83.             col1 = str(combo[j][0])
84.             col2 = str(combo[j][1])
85.             col3 = str(combo[j][2])
86.             col4 = str(combo[j][3])
87.             col5 = str(combo[j][4])
88.             col6 = str(combo[j][5])
89.             col7 = str(combo[j][9])
90.             col8 = str(combo[j][10])
91.             col9 = str(combo[j][11])
92.             col10 = str(combo[j][12])
93.             col11 = str(combo[j][13])
94.             col12 = str(combo[j][14])
95.             col13 = str(planesangle[j+1][0])
96.             col14 = str(residual[j+1][0])
97.             col15 = str(residual[j+1][1])
98.             col16 = str(residual[j+1][2])
```

```
            col17 = str(residual[j+1][3])
                    col18 = str(combo[j][18])
                    col19 = str(combo[j][19])
                    col20 = str(combo[j][20])
                    col21 = str(combo[j][21])
                    col22 = str(combo[j][22])
                    col23 = str(combo[j][23])

                    fo.write( col1 );
                    fo.write( "," );
                    fo.write( col2 );
                    fo.write( "," );
                    fo.write( col3 );
                    fo.write( ",");
                    fo.write( col4 );
                    fo.write( ",");
                    fo.write( col5);
                    fo.write( ",");
                    fo.write( col6 );
                    fo.write( ",");
                    fo.write( col7);
                    fo.write(",");
                    fo.write(col8);
                    fo.write(",");
                    fo.write(col9);
                    fo.write(",");
                    fo.write(col10);
                    fo.write(",");
                    fo.write(col11);
                    fo.write(",");
                    fo.write(col12);
                    fo.write(",");
                    fo.write(col13);
                    fo.write(",");
                    fo.write(col14);
                    fo.write(",");
                    fo.write(col15);
                    fo.write(",");
                    fo.write(col16);
                    fo.write(",");
                    fo.write(col17);
                    fo.write(", ");
                    fo.write(col18);
                    fo.write(", ");
                    fo.write(col19);
                    fo.write(", ");
                    fo.write(col20);
                    fo.write(", ");
                    fo.write(col21);
                    fo.write(", ");
                    fo.write(col22);
                    fo.write(", ");
                    fo.write(col23);
                    fo.write("\n");

                fo.close()


            end = input("End program? y/n:")
```

```
160.
161.           if end.strip() == 'y':
162.               break
```